Nonlinear Silicon Waveguides for Integrated Fiber Laser Systems

WONG, Chi Yan

A Thesis Submitted in Partial Fulfillment
of the Requirements for the Degree of
Doctor of Philosophy
in
Electronic Engineering

The Chinese University of Hong Kong
August 2013

Abstract of thesis entitled:

Nonlinear Silicon Waveguides for Integrated Fiber Laser Systems

Submitted by WONG, Chi Yan

for the degree of Doctor of Philosophy in Electronic Engineering

at The Chinese University of Hong Kong in August 2013

Silicon-on-insulator (SOI) based photonic devices have attracted great interest from photonics community because of its compatibility with state-of-the-art CMOS fabrication processes and its potential of making energy efficient and low cost photonic integrated circuits (PICs) for high bandwidth optical interconnects and integrated optical sensors. Wavelength division multiplexing (WDM) is already widely used in optical communications and is also of interest for optical sensors, providing advantages of low cost, and high speed compared with single wavelength approach. However, the cost and the bulkiness of WDM systems increase proportionally with the number of wavelengths if conventional external laser source is used. Therefore, low cost and compact laser source with stable and high line quality is of great interest for integrated sensors.

In this thesis, we investigate the incorporation of silicon photonic devices as intracavity elements in fiber lasers for various applications. Therefore, the high flexibly and rich functionalities of fiber lasers can be directly used in the PIC. Also, high-speed feedback control of the cavity becomes possible. The possibility of applying nonlinear SOI waveguides to fiber lasers is investigated. We propose and

demonstrate a multiwavelength erbium-doped fiber laser stabilized by four-wave mixing (FWM) in a nonlinear SOI waveguide. Such multiwavelength lasers are potentially suitable for WDM sensing. The wavelength selectivity was achieved by an intracavity Fabry-Pérot comb filter. Making use of the nonlinearity of the SOI waveguide, a multiwavelength laser with six output wavelengths at 0.8 nm spacing was achieved.

We study a passive mode-locked erbium-doped fiber ring laser based on a nonlinear SOI microring resonator (MRR). By using the MRR as the comb filter and the nonlinear medium, a stable mode-locked pulse train at 100 GHz was produced by filter-driven four-wave mixing. Such lasers can act as high repetition rate optical clocks for high speed applications and coherent optical comb source for high spectral efficiency modulation schemes such as orthogonal frequency division multiplexing (OFDM).

Besides the parametric processes, we study a graphene based saturable absorber which can be used to achieve ultrafast passive mode-locked laser for SOI sensing platform. Graphene based photonic devices have attracted considerable interest because of their unique zero bandgap and linear electronic dispersion. The graphene on silicon waveguide structure offers the advantage of greatly increasing the interaction length compared to the geometry with light incident normal to the graphene plane. We describe a mode-locked fiber laser using graphene on silicon saturable absorber.

Finally, we study the possibility of expanding the working wavelengths to mid-infrared (mid-IR) for chemical sensing or free-space communications. MRRs

were fabricated on silicon-on-sapphire (SOS) wafer and characterized at 2.75 μm. We developed a characterization technique to measure the Q of MRRs using a fixed wavelength source by only varying the temperature of the device. The proposed method provides an alternative method of Q measurement for MRRs in mid-IR where tunable lasers may not be easily available.

摘要

絕緣層上覆硅（SOI）為基礎的光子器件引起了光電子界濃厚的興趣。因為它兼容先進的 CMOS 製造工藝，並且可製成高能源效益及低成本的光子集成電路（PIC）應用在高帶寬光互連和集成光學傳感器波分複用（WDM）技術已廣泛用於在光通信中，而且也開始應用於光學傳感器。它比單波長方案提供更低成本和高速的方案。然而如果使用傳統的外部激光源，WDM 系統的成本和體積與波長數目成正比。因此光學傳感器應用渴求低成本和小巧並且提供穩定和高線寬質量的激光源。

在這篇論文中，我們探討硅光子器件成為光纖激光器的腔中部件所衍生的各種應用。光纖激光器的高靈活和豐富的功能，可以直接使用在 PIC 上。此外腔內高速反饋控制亦變成可能。我們也探討應用非線性 SOI 波導在光纖激光器的可行性。我們提出並實現了在非線性 SOI 波導中以四波混頻（FWM）穩定多波長摻鉺光纖激光器。這種多波長激光器可能適合於 WDM 感知應用。腔內使用法布里－珀羅梳狀濾波器來選擇波長。使用 SOI 波導的非線性，實現具有 6 個輸出波長，波長間距為 0.8 納米的多波長激光器。

我們研究基於非線性 SOI 微環諧振腔（MRR）的被動鎖模摻鉺光纖環形激光器。通過使用 MRR 作為梳狀濾波器和在非線性介質，過濾器驅動四波混頻產生穩定的 100 GHz 鎖模脈衝。這種激光器可以充當高重複率的光學時鐘和應用於高頻譜效率的調制方案的相干光梳光源，例如正交頻分複用（OFDM）。

除了參量過程，我們研究了基於石墨烯的可飽和吸收器。它可以用來實現超高速的被動鎖模激光器應用在 SOI 傳感平台。基於石墨烯的光子器件已經吸引了相當大的注視，因為其獨特的零能隙和線性電子色散。在硅波導上覆石墨烯這種結構提供相比垂直入射擁有更長的相互作用長度。我們實現了一個基於硅上覆石墨烯的飽和吸收器的鎖模光纖激光器。

最後，我們研究將工作波長擴展至中紅外波長（mid-IR）為化學傳感或自由空間通信應用的可能性。 MRR 製造在藍寶石上覆硅（SOS）晶圓之上並且使用 2.75 微米波長測量。我們開發了一種測量技術僅通過改變器件的溫度測量和固定波長源來測量 MRR 的 *Q* 值。因為可調諧激光器在中紅外不容易獲得，該方法提供了一種測量 MRR 的 *Q* 值的替代方法。

Dedicated to Kathy and my family, with love.

Acknowledgement

First at all, I would like to thank my advisor, Professor Hon Ki Tsang, for his patient guidance and seemingly endless support. His limitless creativity taught me how to think free of constraint in my research. He taught me how to be an engineer. I have also learnt a lot from his broad and deep knowledge, especially in optoelectronics, which span the gap in my knowledge. He trusts in my abilities and gives me the freedom to pursue my own research agenda that I have a room for growth with responsibility. I am very grateful for the opportunity to work with him.

I wish to thank all the technicians and administrative staff in the Department of Electronic Engineering, especially to Ms. L.C.Ho. Without her technical assistance, I could not fabricate the samples and finish my experiments. I also want to thank the technicians in the Micro and Nano Fabrication Laboratory (MNF): Mr. M. T. Yeung, Mr. Albert Wong, and Mr. Angus Lam. They help to solve countless technical problems in the cleanroom.

I would like to thank Mr. Man Wai Lee from the Nanoelectronics Fabrication Facility (NFF) of The Hong Kong University of Science and Technology (HKUST). He gave a number of advices for developing the fabrication processes in clean rooms at early stage. Also, I also thank for the helps of Mr. Siu Fai Luk from the Electronic and Computer Engineering (ECE) Department of HKUST and Mr. Joe Chan from The Hong Kong Applied Science and Technology Research Institute (ASTRI). They taught me about the processes of sapphire wafers which are the key component of my mid-infrared (mid-IR) research. I thank ePIXfab (www.epixfab.eu) and Institute

of Microelectronics, Singapore for the device fabrication. I also thank Bookham (now Oclaro Inc) for the high power 975 nm pump laser for mid-IR research.

I would like to thank the colleagues in our group: Dr. Yang Liu, Dr. Chao Li, Dr. C.M. Sun, Dr. Xia Chen, Dr. Lin Xu, Ms. Joyce P. K. Ho, Ms Christy K. Y. Fung, Mr. Stanley M. G. Lo, Mr. Zhengzhou Cheng, Mr. Ke Xu, Mr. Yi Min Chen, Mr. Fu Wa Tong, and Ms Zerui Shi who have made countless contributions in our laboratory. A special thanks goes to Dr. Li Chao. He set up the basis of silicon photonics devices design and fabrication processes in our group. He also gives me many productive advices in my research and my career. Xia Chen set up the basis of mid-IR research and grating coupler design for our group. Lin Xu has given me a lot of fun time in the laboratory even we do have much overlap in the research. Joyce is an optimistic girl who creates a fun and positive atmosphere in the group. Christy and Stanley have the great contribution to the development of fabrication in MNF. I would like to express my special thanks to Zhengzhou. He and I worked side-by-side for countless hours on the mid-IR project. We also have a lot of interesting and constructive discussions inside and outside the school. He is the kindest and most dedicated colleague for anyone could hope for. His hard work and focus attitudes in research influence me continuously. Ke Xu and Yi Min have done a lot of interesting and enjoyable experiments with me. I have learnt a lot the knowledge of optical communication from them. I also thank Fu Wa who introduces the field of fiber lasers. We work together for the early stage of silicon embedded fiber laser research for many nights. I would also like to express my appreciation to the other group members: Dr. Mable Fok, Dr. K.J. Chen, Dr. C.M. Sun, Dr. Y.H. Dai, Dr. J.B. Du, Dr. H. He, Dr. K.P. Lei, and Dr. Z.X. Zhang. Another special thanks goes to Mr. Da

Peng Zhang from the Department of Mechanical and Automation Engineering. I have learnt a lot of mode-locked lasers from him. I must additionally thank Zhengzhou, Ke Xu, Yi Min and Lang Wang again. They helped me to pass through the difficult days. During this period, they encouraged me and help me to gain the self-confident again. I could not image how I can pass through the bad time without them. Besides the colleagues of our group, I also wish to thank Dr. Hui Chen from ECE of HKUST. We have spent a lot overnight time together at the laboratory. He had shared a lot of experience on the nonlinear silicon photonics.

I would like to thank Dr. Vic Kam Tuen Law, Dr. Kin Hung Fung, Professor Zikang Tang, and Professor Zhiyu Yang from the Department of Physics HKUST. Vic and Hung did not only teach me a lot of the beautiful and elegant theoretical physics but let me do not constrain myself to study as a under graduate student. Professor Zikang Tang and Professor Zhiyu Yang introduced me the fascinating experimental physics and let me involve to their research of carbon nanotubes and photonic crystals. I also have to thank my former advisor, Dr. Xiaodong Cui from the Department of Physics of The University of Hong Kong during my master degree study. He taught me how to be an experimentalist. He almost knows everything in experimental physics. I always treat him as my role model of experimental physicist. He also taught me do not constrain the study in fundamental physics.

I also have to thank a lot of nice and smart people I have met who have benefited my life in academia. Sorry for that I cannot list them in details because of the limited space of the paragraph.

Finally, I could not imagine how to express my deepest gratitude to my family and my girlfriend Kathy. They give countless encouragement, support and love to me for chasing my dream.

Table of Contents

List of figures

1 Introduction

1.1 Integrated photonics

Integrated photonics is inspired by the great success of integrated electronics. Photonics means the manipulation of photons (optical signal) rather than electrons (electrical signal). The idea of integrated photonics (or integrated optics) was first proposed by S. E. Miller in 1969 [1]. By using the similar idea of integrated electronic circuits, a number of different small footprint optical devices are fabricated on the same substrate simultaneously. They are connected through optical waveguides and forming a complex optical systems for various potential applications, especially for optical communications. However, this idea was far beyond the fabrication technology and the market demand in this era, especially the optical communications have not realized yet.

This situation was changed by the first low loss optical fiber produced by Corning Glass in 1970. This idea of optical fiber communication was first proposed by C. K. Kao and G. Hockham in 1966 [2]. By using the advantages of ultrahigh bandwidth (>5 THz for communication band (C-band)) and low power attenuation (<0.2 dB/km), optical fiber commutation networks dominates the local and long-haul data transmission after only 4 decades of development. As the demand of commutation bandwidth continues to grow, a number of networking scheme have been used, including wavelength division multiplexing (WDM) networks. One of the major issues of optical communication is the limitation due to optoelectronic conversions. Since the optical signal is not easy to be manipulated as the electrical one, the routing

and regeneration of the optical networks are still done by electronic systems. Due to the limited processing speed and the high power consumption of electronic systems, a number of optoelectronic conversions limit the performance and the growth of the optical communication networks.

Integrated photonic devices provide a new solution to replace the electronic systems of the networks without optoelectronic conversions. If the optical signals can be processed without the needs of regenerating the signal at the end, it greatly reduces the power consumption and the transmission speed of the networks. In fact, a number of individual integrated photonic devices are already used in the practical networks. For example, optical intensity/phase modulators and arrayed waveguide gratings (AWGs), as optical (de)multiplexer, are used as the key components for constructing the modern optical networks. Some of the add-drop optical (de)multiplexers (Cisco Co.) are already integrating the optical and electronic components on same printed circuit board [3]. The problem becomes how to further low down the production and operation costs, e.g. scaling down the footprints or integrating the optical and electronic components on a single chip.

On the other hand, modern electronic computing is facing the problems of heat dissipation and limited speed of on-chip electronic interconnects. As the number of transistors almost doubles every 18 months, by Moore's law, the heat generation is also increased exponentially. Although the power consumption (as the heat generation) can be compensated by employing shorter transistor gate lengths, the clock rate of the processor is still limited by heat dissipation of the chip. One approach is using parallel computation, which has been already implemented in multi-core CPU/GPU for latest desktop computers. However, as the number of core

increases, the required bandwidth of communications between cores also increases exponentially. The limited electrical bandwidth of electronic interconnects sets the upper bound of the parallel computation. Moreover, a large portion of power consumption and heat generation of microprocessors is due to the electronic interconnects. Photonic integrated circuit (PIC) provides a promising solution to break this bandwidth limit. Also, the potentially low power consumption of optical interconnects also helps the heat dissipation of the chip.

1.2 Silicon photonics

Silicon, a well known semiconductor has been driving the information technology revolution for over a half-century. In fact, silicon is a very good optical material since it is transparent in optical communication band (C-band) (1530-1565 nm). By making use of the high refractive index of 3.46 at C-band, much smaller footprint photonic devices, compared with other materials such as polymers and fused silica, can be made. Therefore, silicon provides an integrated photonic platform with much higher device density. However, as the footprint is smaller, the major challenge is the precise fabrication technology. By the success of silicon based integrated electronic circuits, mature and high precise complementary metal-oxide-semiconductor (CMOS) technologies had been developed. It opens the possibility of making silicon based PIC in silicon-on-insulator (SOI) wafer, so-called “silicon photonics”. As using the same fabrication technologies, silicon photonic circuit becomes the most promising choice for achieving monolithic integration with electronic circuit in order to provide ultrahigh bandwidth optical interconnects for future microprocessors.

A number of high quality passive components have been demonstrated, such as Mach–Zehnder interferometers (MZIs), microresonators, photonic crystal waveguide and AWGs [4]. Recently, surface plasmon waveguides (SPWs) were demonstrated in SOI platform which have over one order of magnitude smaller footprint than the dielectric waveguides [5]. Figure 1.1 shows image of the fabricated passive PIC on SOI wafer. However, because of the centrosymmetry of silicon crystal lattice structure, it is not possible to make the active devices, e.g. optical modulators by Pockels effect in other materials such as lithium niobate and gallium arsenide. Fortunately, since the observation of free-carrier plasma dispersion effects in silicon by R. A. Soref in 1987 [6], it becomes possible to make optical modulators in silicon. During over two decades of development, a number of optical modulators and add/drop multiplexer based on MZIs and microresonators have been demonstrated

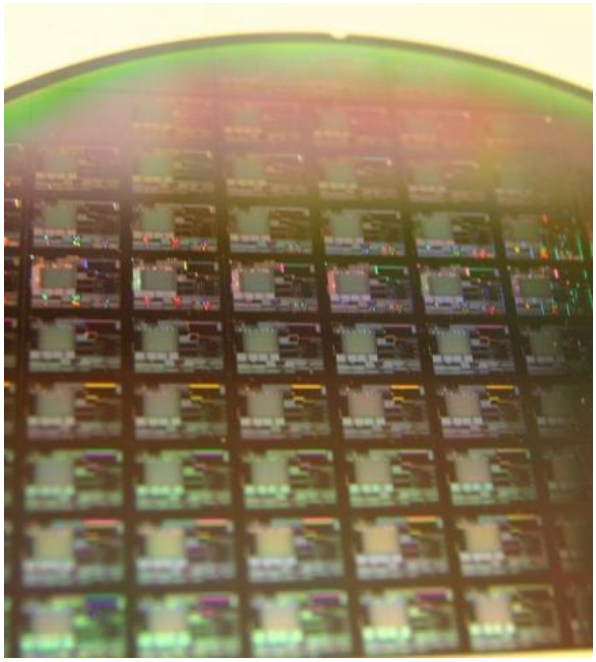

Figure 1.1 SOI wafer with integrated photonic circuits.

[7], [8], [9], [10]. The highest modulation speed is up to 50 Gb/s via carrier depletion in MZI structure [10].

On the other hand, the on-chip photodetectors for silicon photonics are also a hot research topic of silicon photonics. As mention above, the silicon has bandgap energy of 1.12 *e*V which makes silicon transparent to C-band. Fortunately, it has been solved by deposition of a layer germanium on top of silicon waveguides [11] or introducing defect states by ion-implantation [12]. By integrating the components of demodulators and detectors, a number of different integrated optical receivers for advance optical communication format have been demonstrated, e.g. DPSK receivers [13].

As the on-chip modulation and detection have been done, the last holy grail of silicon photonics is the optical gain/laser source. Due to the indirect bandgap nature of silicon, it is hard to achieve efficient light emission. Even it does, the wavelength is still not suitable for optical communication. The first step is achieving the optical gain in silicon. One approach is using optical nonlinearity of silicon, the first successfully demonstrated optical gain in silicon waveguide was stimulated Raman scattering (SRS) [14], [15]. Several years later, the first silicon Raman laser was achieved [16]. Finally, monolithic silicon Raman lasers were demonstrated in fully CMOS compatible SOI platform [17], [18]. Another approach is using parametric processes, the first efficient parametric gain in SOI waveguides was demonstrated in 2006 [19]. However, parametric gain is not strong enough to compensate the loss of two-photon absorption (TPA) and the resulting free-carrier absorption (FCA) inside the cavity. Silicon optical parametric oscillator (OPO) has not been demonstrated yet. Those optical amplifiers and lasers using optical nonlinearity, however, require

external high power pump lasers which set the lower bound of total power consumption of the systems. Those solutions may not be suitable for low-power requirement applications, e.g. microprocessor on-chip interconnects.

Besides those optical nonlinear approaches, some linear (lower power consumption) approaches are proposed and demonstrated: deposition of a layer of III-V on top of waveguide and erbium doping in silicon/silicon dioxide. Especially the methods of III-V deposition, a different type of integrated lasers are achieved, such as continuous-wave (CW) lasers, active mode-locked lasers, passive mode-lasers and even hybrid mode-lock lasers [20], [21]. However, III-V deposition is not a CMOS compatible process. This problem can be solved by using germanium on top of silicon. By adding tensile strain and n-type doping to the germanium layer, efficient direct bandgap emission can be achieved [22], [23], [24]. The major challenge remains: if the WDM scheme is used in on-chip interconnects, a number of lasers with different lasing wavelengths are needed to be integrated on the same chip. The heat generation of each laser may alter the lasing wavelengths among the others since the lasing wavelengths depend on the refractive index of the cavities which are very thermal sensitive in silicon [25]. Moreover, the short cavity length also limits the laser line quality which limits the performance in high precision requirement applications such as time and frequency metrology. It may need an alternative solution to provide stable WDM laser sources or good line quality as the conventional lasers for silicon photonics.

1.3 Integrated optical sensing

Integrated optical sensors have been shown great potential of chemical detection and analysis, with the advantages of high sensitivity, compact and immune to environmental electromagnetic interference. There is a considerable attention focused on biochemical sensors because they have a number of applications in fundamental biomedical research, healthcare and environmental monitoring. Analogy to optical communication, WDM sensing scheme can be used and provides multiplexed detection inside a single device.

In optical biochemical sensing, the most attractive method is label-free optical sensing which is measuring the refractive index change, optical absorption induced by the interactions of molecules which is not related by the total sample mass but the surface density or concentration. Also, the target molecules are not needed to be labeled (chemically modified). Therefore, the detection is performed in the natural forms of the molecules. Compared with other sensing schemes, e.g. fluorescence-based detection, this kind of detection is relatively easy and low cost, and can be done in real time and on site.

There are a number of optical structures for label-free biosensors: surface plasmon resonance, interferometers (e.g. MZI), special waveguide structures (e.g. metal-clad waveguides), resonators and photonic crystals [26], [27], [28], [29]. Interferometers and resonators are relatively easier to be implemented in integrated platform. For example, MZI structures can be used to compare the refractive index change in two paths, as shown in Figure 1.2 [28]. Also, by using optimized waveguide design, the refractive index change (propagation constant change) in waveguide is much higher

than directly passing through the sample in free space [30]. MZIs are easy in design and high fabrication tolerance. However, they are limited in sensitivity and large footprint.

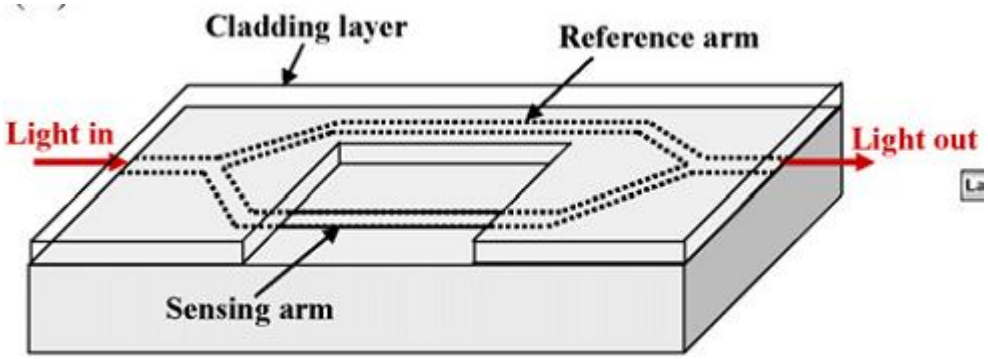

Figure 1.2 MZI based biosensor, adapted from [28].

Compared with interferometer structure, resonator structures have much higher sensitive and smaller footprint. The tiny refractive index change in cavity leads an enlarged change in resonant wavelength. By using high quality factor (*Q*) microresonators, single-molecule detection can be achieved [26]. Also, the optical field enhancement inside the cavity as the light is effectively trapped inside for a period. Therefore, the effective interaction length between light and molecules is much longer than the round-trip length of the cavity. The absorption change can also be enlarged. If it is used with microfluidic system, the sample can be efficiently sensed by directly transferring to the sensors [31]. The total sample mass can be further reduced.

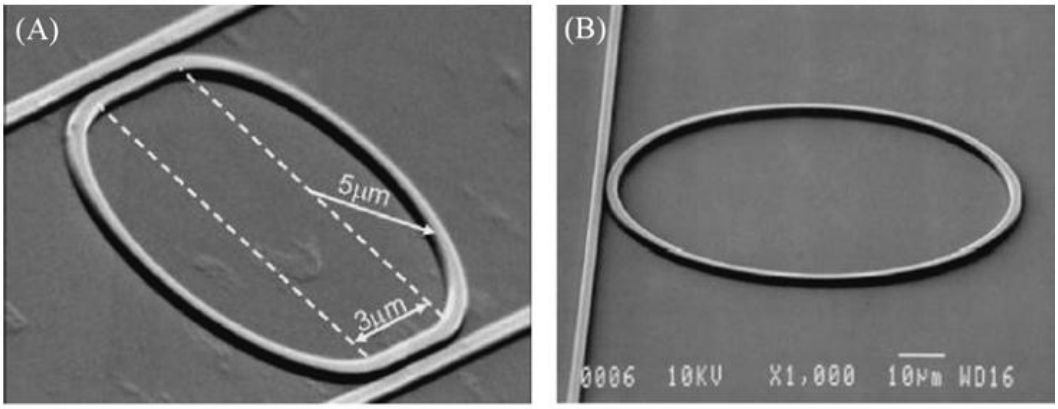

Figure 1.3 (a) SOI microresonator and (b) polymer microresonator based biosensors, adapted from [27], [29].

Although the integrated sensors are compact, the detection and analysis have to perform in external systems for silica and polymer platform. Making use of the optoelectronic integration of silicon photonics, it provides a promising sensing platform including sensing and processing functionalities in the same chip which is a truly lab-on-a-chip solution. A number of silicon optical sensors have been demonstrated: (bio)chemical detection using microresonators/MZIs [27], [32], [33], photonic crystal based biosensor for protein detection [34], (bio)chemical on-chip absorption spectroscopy using microring resonators (MRRs) [35], [36], and WDM-addressed microring sensor array [37].

Similar to optical interconnects, the on-chip laser sources is still the major challenge to integrated optical sensor. As mention above, the III-V/germanium on-

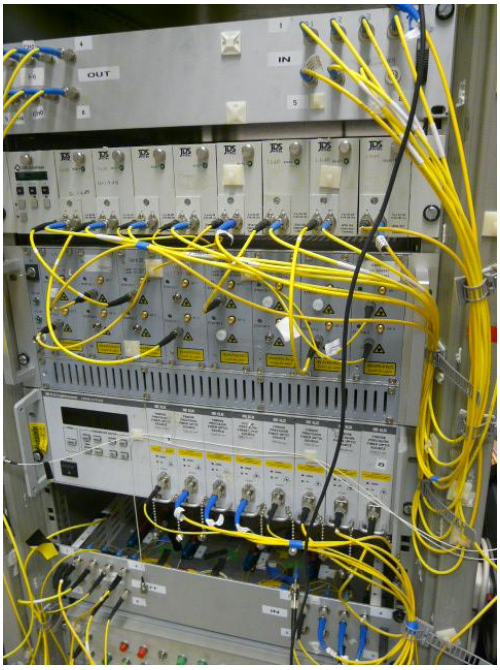

Figure 1.4 24 channel WDM Source, adapted from [38].

chip laser still have a number of practical issues in WDM applications. Also, if external WDM source is used, the bulkiness of the source increases with the number of wavelengths [38]. Multiwavelength erbium-doped fiber lasers (EDFLs) provide compact and low cost multiwavelength sources [39]. However, it needs to suppress the gain competition due to homogeneous gain broadening of erbium-doped fibers. One option is using optical nonlinearity. SOI waveguides already have different optical nonlinearities as mentioned above. If the SOI chip is embedded as part of the fiber laser cavity, it provides the similar advantages of on-chip laser sources without their disadvantages: the WDM laser output can be directly used in the integrated sensor components in order to achieve a compact sensor system. Also, a number of different types of fiber lasers can be used in SOI platform for different applications.

On the other hand, as the original purpose of integrated optics, it is possible to integrate the optical components of the laser to the chip in order to simplify the fiber laser system and enhance its stability. Furthermore, SOI embedded fiber laser opens the possibility to intracavity optical sensing, which provides a much higher sensitivity compared with normal sensing schemes. Making use of integrated electronics, it is also able to achieve high speed data processing and fast feedback control to the cavity while the other fiber laser systems cannot provide (even using other integrated platforms).

1.4 Overview of thesis

In this thesis, we will describe how to develop SOI photonic device embedded fiber laser systems for various applications. In Chapter 2, we propose and demonstrate a multiwavelength erbium-doped fiber laser stabilized by four-wave mixing (FWM) in a nonlinear silicon-on-insulator (SOI) waveguide for WDM sensing. The optical gain was provided by an erbium-doped fiber amplifier, and the wavelength selectivity was achieved by a comb filter in the ring cavity. The FWM in the SOI waveguide was enhanced by applying a reverse-biased p-i-n diode structure to reduce free-carriers absorption (FCA). The coupling between the single-mode fiber (SMF) and the SOI waveguide was using grating coupler which also works as the bandpass filter and polarizer. Making use of the nonlinearity of the SOI waveguide, multiwavelength laser with six output wavelengths at 0.8 nm spacing was achieved. The power difference among modes was equalized within a range of 1.8 dB. The power fluctuation of each mode was stabilized to less than 0.65 dB during 20 minutes observation at room temperature.

In Chapter 3, we further combine the comb filter and the nonlinear waveguides as a nonlinear MRR. From the pulsation result of the laser in Chapter 2, we found that multiwavelength laser using FWM with comb filter can be treated as a mode-locked laser using dissipative FWM (DFWM). It is able to be the potential comb source for orthogonal frequency division multiplexing (OFDM) and ultrahigh speed on-chip optical clocks. We propose a passive mode-locked EDFL based on a nonlinear silicon MRR by using filter driven FWM (FD-FWM). The *Q* and free-spectral range (FSR) of the MRR are ~50000 and 0.78 nm, respectively. By using the nonlinearity of the silicon MRR, it achieves stable mode-locking pulse train with 100 GHz repetition rate.

In Chapter 4, in order to explore other possible laser source for integrated sensor, a new hybrid structure: graphene on silicon suspend membrane waveguide (SMW) was investigated. We studied the saturable absorption in this hybrid structure and observed a large saturable absorption, as high as 50% change in transmission. Furthermore, we propose and demonstrate a mode-locking of an erbium fiber laser using a graphene on silicon SMW. By using the saturable absorption of graphene in the evanescent field of the waveguide mode, a stable mode-locked fiber laser is achieved. The structure is compatible with silicon optical waveguides and may be easily integrated with other passive waveguide devices such as tunable filters or silicon modulators for making tunable mode-locked lasers.

In Chapter 5, we explore how to transfer the current results to mid-infrared (mid-IR) range. We fabricated mid-IR MRRs and characterized them by thermal tuning using a fixed wavelength Er/Pr-codoped ZBLAN fiber laser at 2.75 μm [40]. A method of *Q* estimation by temperature scanning transmission curve is proposed

which does not need any curve fitting. Similar results are obtained if we assume the ratio of resonant period (in temperature) to the FWHM of resonant dip/peak, $\Delta T/\delta T$, is equal to the cavity finesse [41]. Finally, the thermo-optic coefficient of the epitaxial silicon layer of SOS is also estimated by perturbation method [42], [43]. The measurement techniques were verified with conventional SOI microring resonators in near-IR.

In the last chapter, we summarize our works in this thesis. Based on the current results, including the results from other groups, potential future work is proposed.

2 Nonlinear silicon waveguide & multiwavelength laser

2.1 Introduction

Silicon photonic integrated devices have attracted a considerably interest in bio-sensing, gas detection, and spectroscopy because of their potential of lab-on-a-chip applications with a number of advantages, such as low cost, high sensitivity, small size, and high scale integration [34], [35], [37], [44], [45], [46]. Recently, wavelength division multiplexing (WDM) sensing schemes have been investigated, which provide a simpler, lower cost and higher speed solution compared with single wavelength approach [39], [46]. However, the bulkiness and cost of conventional WDM light sources are proportional to the number of wavelengths.

Multiwavelength erbium-doped fiber lasers (EDFLs) provide compact and low cost multiwavelength sources [39]. However, the homogeneous gain broadening of erbium-doped fibers (EDFs) leads to the laser instability because of gain competition [47], [48] since the energy transitions share the same energy levels of erbium ion, as shown in Figure 2.1 [49].

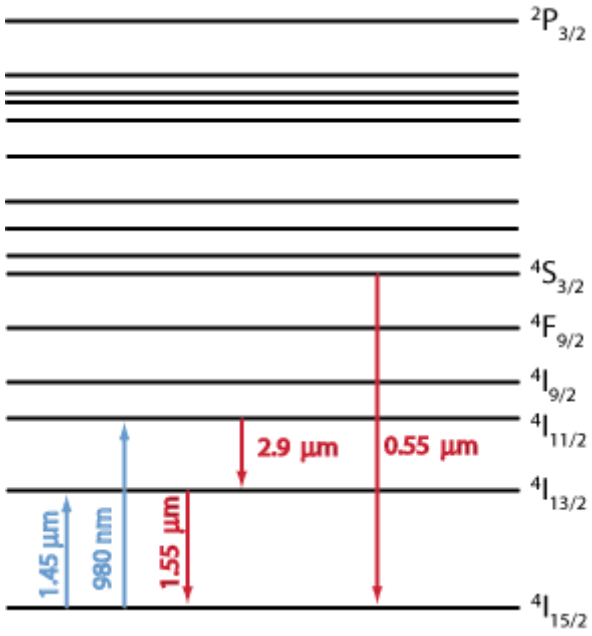

Figure 2.1 Energy level transitions of erbium ion, adapted from [49].

There are several different approaches that have been previously proposed to suppress these instabilities [39], [50], [51], [52], [53], [54], [55]. Among those techniques, FWM provides a simple and flexible method for laser cavity design. It has been successfully demonstrated in dispersion shifted fibers (DSFs), highly nonlinear fibers (HNLFs), photonic crystal fibers (PCFs) and graphene [51], [52], [53], [54], [55].

Moreover, for silicon optical sensor platform, the nonlinear media can be directly replaced by nonlinear silicon-on-insulator (SOI) waveguides which have been used in high speed nonlinear all-optical signal processing [56]. It is due to the high Kerr nonlinearity, n_2, of bulk silicon which is over 2 orders of magnitude larger than that of silica. Together with smaller effective area in SOI waveguides, the resulting nonlinear optical coefficient (γ) is typically of the order of 100 $W^{-1}m^{-1}$ [56], [57],

which is about four orders of magnitude larger than commercial HNLF and PCF which have γ of about 0.01 $W^{-1}m^{-1}$. Thus a centimeter length of SOI waveguide may replace an HNLF or PCF with hundreds of meters length. It is also possible to simplify the laser cavity by integrating a number of optical components onto a single chip, which decreases the cost and complexity of the system. Furthermore, employing SOI waveguide in the multiwavelength EDFL greatly reduces the fiber laser cavity length and potentially improves the laser stability. By embedding part of the laser cavity into the silicon chip, the laser output can be directly used in the integrated sensor components and high speed feedback control of the cavity becomes possible. In this chapter, we propose and demonstrate the stabilization of a multiwavelength EDFL which uses FWM in a SOI waveguide to stabilize simultaneous lasing at different wavelengths.

2.2 Nonlinear silicon photonics

2.2.1 Silicon nonlinearity

The optical nonlinear effects of silicon are related to the interaction between the optical field with the electrons and phonons of silicon crystal. The optical field excites the vibration of the outer shells' electron orbitals of silicon atoms. The induced displacement between electron orbitals and the nucleus produces polarizations. Figure 2.2a shows the schematic diagram of the optical field, at frequency ω, induces the polarization of a silicon atom. The nonlinear effects are due to the nonlinear response of the polarization to the optical field. In classical electrodynamics, the macroscopic polarization of the isotropic material, *P*, can be

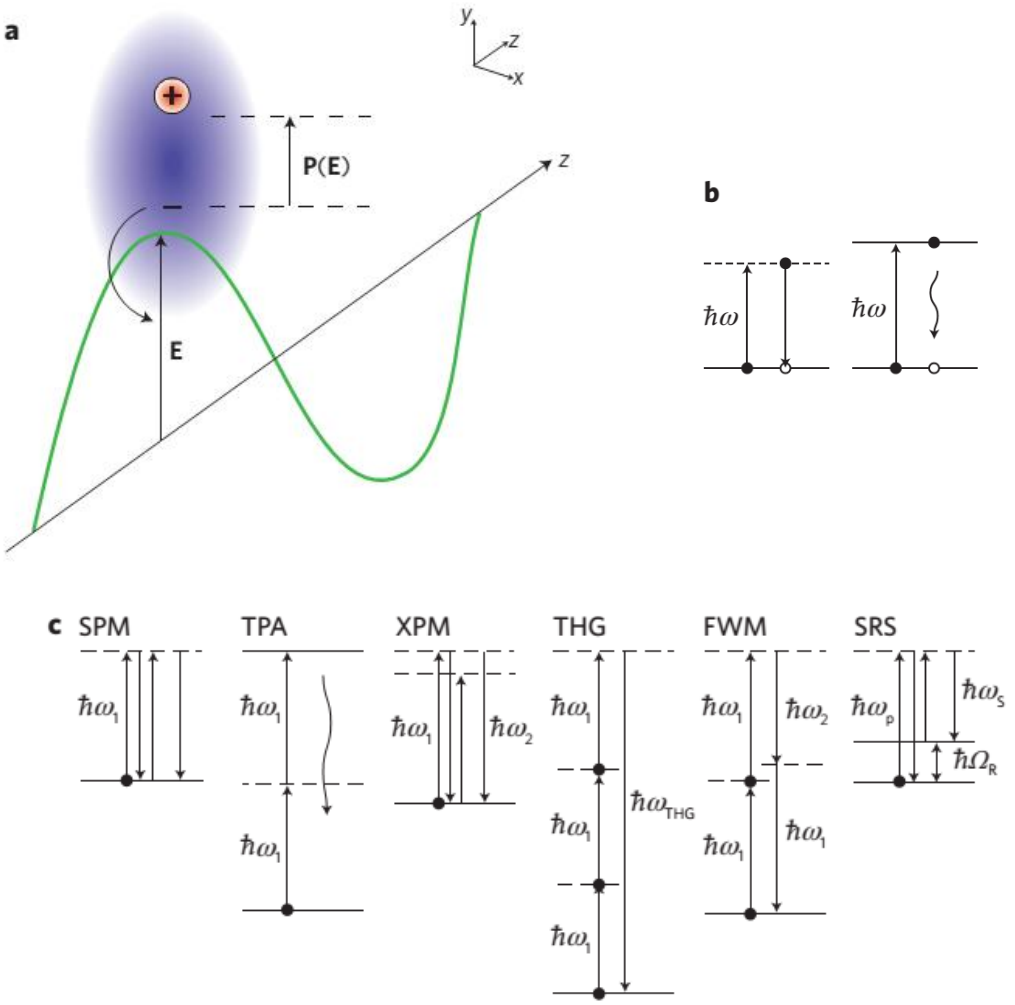

Figure 2.2 (a) The schematic diagram of the optical field, at frequency ω, induces the polarization of a silicon atom. Energy diagrams of optical transitions: (b) refractive index changes (left) and FCA (right); (c) SPM, TPA, XPM, THG, FWM, and SRS. Figures are adapted from [56].

expressed in a power series of the driving electric field, E by assuming the instantaneous dielectric response [58], [59]:

$$P = \varepsilon_0(\chi^{(1)}E + \chi^{(2)}E^2 + \chi^{(3)}E^3 + \ldots), \tag{2.1}$$

where ε_0 and $\chi^{(i)}$ are the vacuum permittivity and the complex *i*-order susceptibility, respectively, with *P* and *E* are scalars for simplification. $\chi^{(i)}$ contain all the information of the linear and nonlinear effects of the materials such as phase shift, amplification, absorption of the incident field, or even new frequency generations. In general, $\chi^{(i)}$ are tensors in rank (i + 1). For simplification, those susceptibility terms are scalars in following discussion.

The linear processes are related to the complex first-order susceptibility term $\chi^{(1)}$. The real part of the $\chi^{(1)}$ mainly contributes to the real part of the refractive index while the imaginary part of $\chi^{(1)}$ induces the gain and loss. $\chi^{(1)}$ of silicon comes from the bounded electrons and free-carriers which can be classically described by the Lorentz model and Drude model, respectively [59]. In quantum mechanical picture, the bounded electron contribution can be described by single-dipole oscillation of the electron between the bounded state and the virtual state, as shown in the energy diagram of Figure 2.2b. On the other hand, the FCA contribution can be described by an absorption process followed by a non-radiative recombination, as shown in Figure 2.2b. The resulting total refractive index change due to free-carriers can be expressed by an empirical function:

$$n(\lambda, N_e, N_h) = n_0(\lambda) + \Delta n_f(N_e, N_h) - i\frac{\lambda}{4\pi}\Delta\alpha_f(N_e, N_h), \qquad (2.2)$$

where $n_0(\lambda)$ is the refractive index in wavelength λ without free-carriers, Δn_f is the free-carrier index (FCI), $\Delta\alpha_f$ is the FCA, N_e and N_h are the concentrations of free electrons and holes, respectively. In wavelength of 1550 nm in silicon, the empirical function of FCI and FCA is [6], [60]:

$$\Delta n_f = -\left[8.8\times10^{-4}\,\frac{N_e}{\mathrm{cm}^{-3}} + 8.5\left(\frac{N_h}{\mathrm{cm}^{-3}}\right)^{0.8}\right]\times10^{-18}$$
$$\frac{\Delta\alpha_f}{\mathrm{cm}^{-1}} = -\left[8.5\,\frac{N_e}{\mathrm{cm}^{-3}} + 6.0\,\frac{N_h}{\mathrm{cm}^{-3}}\right]\times10^{-18} \quad (2.3)$$

where N_e and N_h are in unit of cm^{-3}, and $\Delta\alpha_f$ is in unit of cm^{-1}. This FCI and FCA have been widely used in silicon photonics for optical modulator and variable optical absorbers [5].

The second-order susceptibility term $\chi^{(2)}$ describes the nonlinear processes such as second harmonic generation, sum-/difference-frequency generation and optical rectification. However, it is zero in silicon due to its centrosymmetric crystal structure [56], [59]. Fortunately, $\chi^{(2)}$ in silicon can be induced by breaking the centrosymmetric, e.g. adding stress on the silicon [61].

The major optical nonlinear effects of silicon come from the third-order susceptibility term $\chi^{(3)}$. The related effects are much more complicate than second-order one. By setting the third-order polarization $P^{(3)}$ as:

$$P^{(3)} = \varepsilon_0 \chi^{(3)} E^3, \quad (2.4)$$

and setting the driving electric field, E, as the superposition of three frequencies ω_k for k = 1, 2, 3:

$$E = \sum_{k=1}^{3} E_k = \frac{1}{2}\sum_{k=1}^{3}\left(E_{\omega_k k}(r,\omega_k)e^{i\omega_k t} + c.c.\right), \quad (2.5)$$

where *c.c.* indicates the complex conjugate, the resulting terms can be sort by their frequency components:

$$
\begin{aligned}
P^{(3)} = & \frac{3}{4}\varepsilon_0\chi^{(3)}\left[\left|E_{\omega_1}\right|^2 E_1 + \therefore\right] && \text{SPM}\\
& + \frac{6}{4}\varepsilon_0\chi^{(3)}\left[\left(\left|E_{\omega_2}\right|^2 + \left|E_{\omega_3}\right|^2\right)E_1 + \therefore\right] && \text{XPM}\\
& + \frac{1}{4}\varepsilon_0\chi^{(3)}\left[\left(E_{\omega_1}^3 e^{i3\omega_1 t} + c.c.\right) + \therefore\right] && \text{THG}\\
& + \frac{3}{4}\varepsilon_0\chi^{(3)}\left[\frac{1}{2}\left(E_{\omega_1}^2 E_{\omega_2} e^{i(2\omega_1+\omega_2)t} + c.c.\right) + \therefore\right] && \text{FWM}\\
& + \frac{3}{4}\varepsilon_0\chi^{(3)}\left[\frac{1}{2}\left(E_{\omega_1}^2 E_{\omega_2}^* e^{i(2\omega_1-\omega_2)t} + c.c.\right) + \therefore\right] && \text{FWM}\\
& + \frac{6}{4}\varepsilon_0\chi^{(3)}\left[\frac{1}{2}\left(E_{\omega_1}^2 E_{\omega_2} E_{\omega_3}^* e^{i(\omega_1+\omega_2-\omega_3)t} + c.c.\right) + \therefore\right] && \text{FWM}\\
& + \frac{6}{4}\varepsilon_0\chi^{(3)}\left[\frac{1}{2}\left(E_{\omega_1}^2 E_{\omega_2} E_{\omega_3} e^{i(\omega_1+\omega_2+\omega_3)t} + c.c.\right) + \therefore\right] && \text{FWM}
\end{aligned}
\quad , \qquad (2.6)
$$

where ∴ indicates the all permutations of frequencies. In quantum mechanical picture, these third-order nonlinear processes can be described by an electron excited to a virtual state via three photon induced dipole transitions and then relax back to the original state by releasing the fourth photon, as shown in Figure 2.2c. Because of the transitions involved virtual states, the photon energies are conserved, therefore, they called optical parametric processes. Moreover, the relaxation processes are ultrafast. It makes these parametric processes as a promising solution for ultrafast optical communications.

The first term in Eqs. (2.6) is called self-phase modulation (SPM) which involved three dipole transitions with same the frequency, shown in Figure 2.2c. The resulting effect is an intensity dependent refractive index, n_2, so-called the Kerr coefficient. SPM leads to the pulse compression and spectral broadening of ultrashort optical

pulse, as the major process of achieving optical soliton in $\chi^{(3)}$ materials. It also plays the major role in supercontinuum generation [62]. If the first two transitions lead to a real eigenstate of the electron, e.g. conduction band of silicon, a pair of electron and hole is generated as free carriers. This effect is called two-photon absorption (TPA). It induces intensity dependent loss in the material. The resulting free carriers also lead to FCA. Together with SPM, the refractive index can be expressed as:

$$n = n_0 + n_2 I - i\frac{\lambda}{4\pi}(\alpha_0 + \alpha_2 I), \tag{2.7}$$

where α_0 and α_2 are the linear loss and the TPA coefficients, respectively.

The second term in Eqs. (2.6) is called cross-phase modulation (XPM) which means the refractive index change was due to another frequency. The effect is twice of SPM, as shown in their coefficients.

The third term is accounted for the third harmonic generation (THG). It means there is a new frequency at three times of the original frequency. It has been demonstrated in green light generation from silicon photonic crystal waveguides at 1550 nm [63].

The remaining terms is FWM which also generates new frequency but involving three dipole transitions with different frequencies. If two photons of these transitions are in same frequency, it is called degenerated FWM, otherwise non-degenerated FWM. FWM has a number of photonic applications such as wavelength conversion and parametric amplification.

Besides these parametric processes, silicon also has strong simulated Raman scattering (SRS). In Figure 2.2c, a pump photon is annihilated and then a photon and an optical phonon are created. The new photon is called Stoke wave with frequency of the difference of the pump photon and phonon (15.6 THz). As the crystal structure of silicon is better defined than that of silica, the SRS in silicon is much stronger than silica but full-width-half-maximum (FWHM) bandwidth (105 GHz) is much narrower than silica [64].

2.2.2 FWM in SOI waveguides

To achieve efficient nonlinear effect in silicon, SOI waveguide is made. If we consider 4 different frequencies CW waves propagates along the waveguide with same polarization $\hat{x}$:

$$E = \frac{1}{2}\hat{x}\sum_{k=1}^{4}(E_k e^{i(\beta_k z-\omega_k t)} + c.c.), \tag{2.8}$$

where β_k is the propagation constant of the wave with frequency ω_k ($\omega_1 + \omega_2 = \omega_3 + \omega_4$), the waves interact in the waveguide through well-known wave equations [65]:

$$\nabla^2 E - \frac{1}{c^2}\frac{\partial^2 E}{\partial t^2} = \mu_0 \frac{\partial^2 P^{(1)}}{\partial t^2} + \mu_0 \frac{\partial^2 P^{(3)}}{\partial t^2}, \tag{2.9}$$

where $P^{(3)} = \varepsilon_0 \chi^{(1)} E$ is the linear polarization. By assuming the waveguide modes can be expressed in following form:

$$E_k = F_k(x, y)A_k(z), \tag{2.10}$$

where $F_k(x,y)$ and $A_k(z)$ is the spatial mode profile and the amplitude of k-th mode, we substitute Eq. (2.1) into Eq. (2.9) and then integrate over spatial mode profile. We obtain a set of coupled equations [65]:

$$\begin{aligned}
\frac{dA_1}{dz} &= \frac{in_2\omega_1}{cA_{eff}}\left[\left(\left|A_1\right|^2 + 2\sum_{k\neq 1}\left|A_k\right|^2\right)A_1 + 2A_2^* A_3 A_4 e^{i\Delta kz}\right] \\
\frac{dA_2}{dz} &= \frac{in_2\omega_2}{cA_{eff}}\left[\left(\left|A_2\right|^2 + 2\sum_{k\neq 2}\left|A_k\right|^2\right)A_2 + 2A_1^* A_3 A_4 e^{i\Delta kz}\right] \\
\frac{dA_3}{dz} &= \frac{in_2\omega_3}{cA_{eff}}\left[\left(\left|A_3\right|^2 + 2\sum_{k\neq 3}\left|A_k\right|^2\right)A_3 + 2A_1 A_2 A_4^* e^{-i\Delta kz}\right], \\
\frac{dA_4}{dz} &= \frac{in_2\omega_4}{cA_{eff}}\left[\left(\left|A_4\right|^2 + 2\sum_{k\neq 4}\left|A_k\right|^2\right)A_4 + 2A_1 A_2 A_3^* e^{-i\Delta kz}\right]
\end{aligned} \tag{2.11}$$

where $\Delta k = \beta_3 + \beta_4 - \beta_1 - \beta_2$ is the phase mismatch, and

$$A_{eff} \approx \frac{\left[\left\langle\left|F_i\right|^2\right\rangle\left\langle\left|F_j\right|^2\right\rangle\left\langle\left|F_k\right|^2\right\rangle\left\langle\left|F_l\right|^2\right\rangle\right]^{\frac{1}{2}}}{\left[\left\langle F_i^* F_j^* F_k F_l\right\rangle\right]} \approx \frac{\left\langle\left|F_i\right|^2\right\rangle\left\langle\left|F_j\right|^2\right\rangle}{\left[\left\langle\left|F_i\right|^2\left|F_j\right|^2\right\rangle\right]} \tag{2.12}$$

is the effective modal area. The approximation is valid for single-mode waveguides [65]. The angle brackets denote the integration of the mode over the transverse spatial coordinates. Also, we can define a useful and simple parameter, so-called the nonlinear coefficient γ:

$$\gamma_k = \frac{n_2\omega_k}{cA_{eff}} \approx \gamma\,. \tag{2.13}$$

We can see that higher γ leads to stronger nonlinear coupling among those waves. As mentioned above, the high nonlinearity of silicon waveguides are due to their higher

n_2 and smaller A_{eff} compared with silica optical fiber. In high index contrast waveguide, this quantity can be modified to [57]:

$$\gamma = k_0 \left(\frac{\varepsilon_0}{\mu_0} \right) \frac{\left\langle n^2 n_2 \left(2|E|^4 + |E^2|^2 \right) \right\rangle}{3 \left| \left\langle E \times H^* \cdot \hat{z} \right\rangle \right|^2}. \tag{2.14}$$

Eqs. (2.11) do not have general analytical solution and must be solved numerically. Fortunately, we still can have some valuable physical insights by taking reasonable approximations. If we assume A_1 and A_2 are the pump waves which are much intense than A_3 and A_4 and remain undepleted during FWM, they can be easily solved:

$$\begin{aligned} A_1 &= \sqrt{P_1} \exp\left[i\gamma (P_1 + 2P_2) z \right] \\ A_2 &= \sqrt{P_2} \exp\left[i\gamma (P_2 + 2P_1) z \right] \end{aligned}, \tag{2.15}$$

where $P_k = |A_k(0)|^2$ is the incident pump power at $z = 0$. And we introduce:

$$B_k = A_k \exp\left[-2i\gamma (P_1 + P_2) z \right], \tag{2.16}$$

for $k = 3,4$. The B_3 and B_4 can be solved to have general solutions:

$$\begin{aligned} B_3 &= (a_3 e^{gz} + b_3 e^{-gz}) \exp\left[-i\kappa z / 2 \right] \\ B_4 &= (a_4 e^{gz} + b_4 e^{-gz}) \exp\left[i\kappa z / 2 \right] \end{aligned}, \tag{2.17}$$

where a_k and b_k are determined by boundary conditions; κ is the effective phase mismatch:

$$\kappa = \Delta k + \gamma (P_1 + P_2); \tag{2.18}$$

g is the parametric gain which depends on pump powers and phase matching:

$$g = \sqrt{(\gamma P_0 r)^2 - (\kappa / 2)^2}. \tag{2.19}$$

In Eq. (2.19), we introduced parameters r and P_0:

$$r = 2\sqrt{P_1 P_2}/P_0,\ P_0 = P_1 + P_2 . \tag{2.20}$$

Eqs. (2.17) show the parametric gain is proportional to γ when it is effectively phase matched ($\kappa = 0$). We can also observe the phase mismatch suppresses the gain. The phase mismatch is mainly due to the dispersion of waveguide propagation constant $\beta(\omega)$. By using Taylor expansion, the propagation constant can be expressed by:

$$\beta(\omega) = \beta(\omega_0) + (\omega - \omega_0)\beta'(\omega_0) + \frac{1}{2}(\omega - \omega_0)^2 \beta''(\omega_0) + \ldots, \tag{2.21}$$

where ω_0 is the reference (central) frequency. For single pump configuration, degenerated FWM ($\omega_1 = \omega_2$, $P_1 = P_2 = P_0/2$, $r = 1$), in short waveguide, the bandwidth of the parametric gain is approximated up to second-order dispersion:

$$\Delta\Omega \approx \sqrt{\frac{\gamma P_0}{2|\beta''(\omega_1)|}} . \tag{2.22}$$

It shows that smaller second-order dispersion of the waveguide leads to wider gain bandwidth. In the small-gain limit, $2\gamma P_0 L << \pi$, the bandwidth is independent to the pump power and only depends on second-order dispersion [66]:

$$\Delta\Omega \approx \sqrt{\frac{4\pi}{\beta''(\omega_1)L}} . \tag{2.23}$$

The SOI waveguides were fabricated on the SOI wafer with 220 nm top silicon layer and 2 μm buried oxide (BOX). The typical waveguide structure is in rib geometry. Waveguide width is 500 nm in order to satisfy the single mode condition of quasi-transverse electric (TE) mode at 1550 nm [67]. The slab height is 60 nm. The theoretical mode field profile is calculated by finite-element method (FEM), as shown in Figure 2.3. By Eqs. (2.12), (2.14) and (2.21), it has A_{eff} and theoretical γ and β'' of 0.17 μm^2, 59 $W^{-1}m^{-1}$, and 1.14 ps^2m^{-1} [57], respectively.

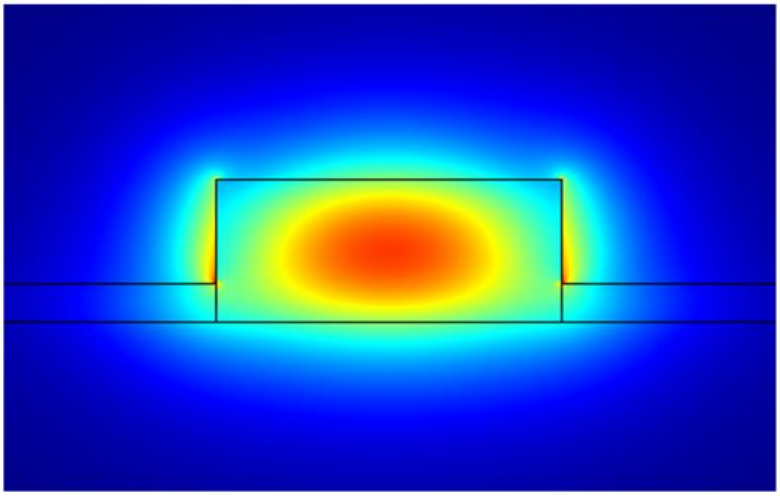

Figure 2.3 The electric field mode profile of corresponding quasi-TE mode, calculated by FEM.

2.2.3 Grating couplers

As FWM is an intensity dependent process, the efficient coupling between SOI waveguides and SMFs is essential. However, as shown in Figure 2.4, the cross-section area of the SOI waveguide core is much smaller than standard single mode fiber (SMF). Moreover, the propagation constants (wave vectors) of their modes are also different.

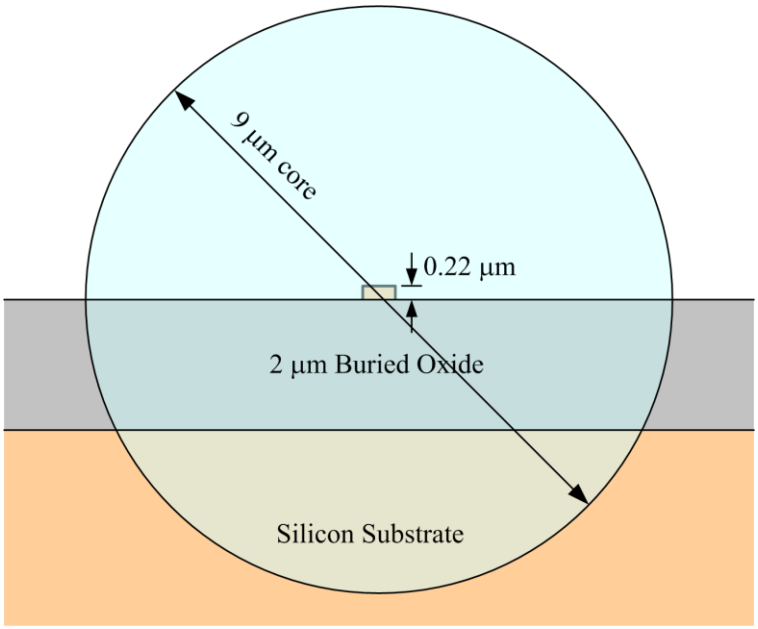

Figure 2.4 The comparison of cross-section area between SOI waveguide and standard SMF.

In order to match the mode field profile and the wave vector between two modes, grating couplers were implemented, which are widely used in silicon optical sensor systems [34], [37], [45], [46], [68]. The grating couplers were designed for coupling quasi-TE light between the SOI waveguide and standard SMF with 9 μm core diameter at 10° off-vertical orientation, as shown in Figure 2.5. The wave vector matching, also called phase-matching, is using modified diffraction grating equation [68]:

$$k_0 n_{eff} = k_0 n_c \sin\theta + q\frac{2\pi}{\Lambda}, \tag{2.24}$$

where $k_0=2\pi/\lambda$, n_c is the refractive index of the top cladding material (silica), θ is the angle between the input/output light and the normal axis of the SOI wafer, n_{eff} is average effective index of the grating, q is the diffraction order (equals to 1 in our

case), and Λ is the grating period. To match the model field profile, the width of grating couplers region is expanded from 500 nm of single mode region to 10 um through an adiabatic taper.

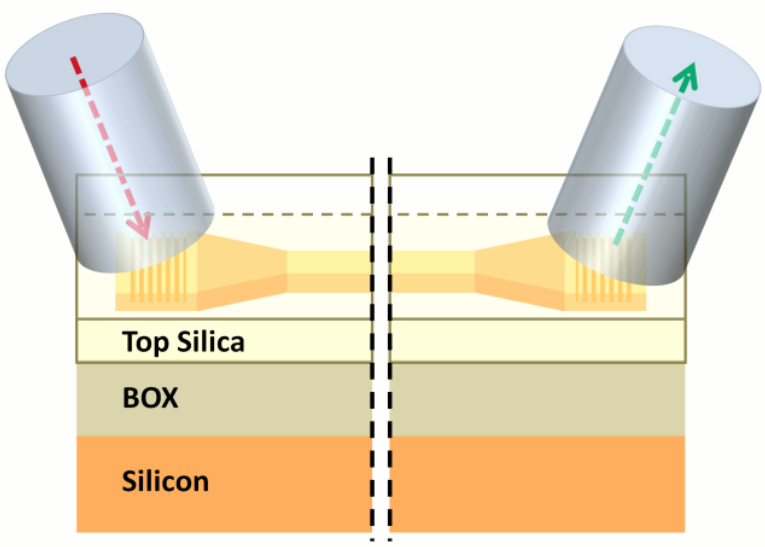

Figure 2.5 The schematic diagram of the experimental setup: light coupled in from input SMF to the silicon strip waveguide and then coupled to output SMF through grating couplers.

To optimize the design of grating parameters, a numerical simulation based on Finite-difference time-domain (FDTD) was used. Due to the limitation of computational power, the model is simplified to two-dimensional (2D), assuming the grating coupler on a 2D slab waveguide with infinite width. We first launched a CW optical fiber mode (effectively a Gaussian mode) at the top cladding with angle of 10° off-vertical. The coupling efficiency was obtained by measuring the optical power of slab waveguide when the system has come to steady state. The preset 70 nm shallow-etched for grating groove was defined by the fabrication process which was optimized to prevent the unwanted reflections at interface by reducing the lateral

index contrast. Under those restrictions, the optimized grating structure has a period of 630 nm and 0.5 filling factor. The typical optical field in steady state is shown in Figure 2.6.

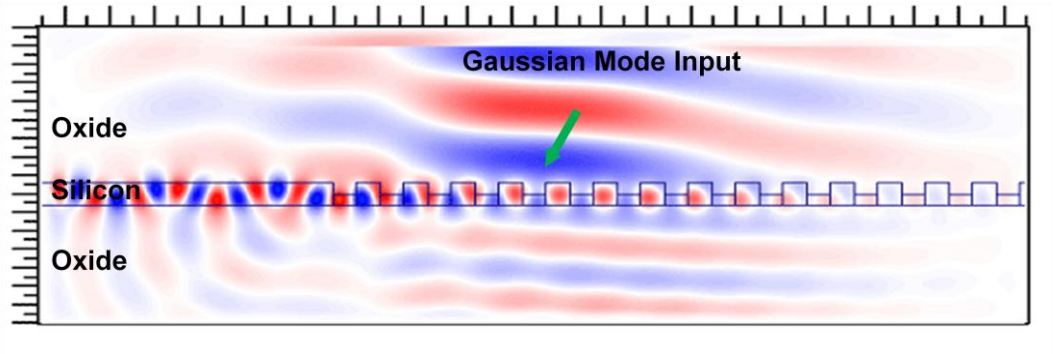

Figure 2.6 The 2D FDTD simulation result of grating couplers in steady state.

In practice, the input and output fibers are mounted on a V-groove fiber holder with three axis positioners at 10° off-vertical orientation while the silicon chip is mounted on a stage horizontal below the fibers, as shown in Figure 2.7a. Figure 2.7b shows the magnified optical image of the fiber and waveguide orientation in efficient coupling.

The fabrication processes of waveguides and grating couplers are based on deep-UV lithography technology from Interuniversity Microelectronics Centre (IMEC), ePIXfab (http://www.epixfab.eu) [69].

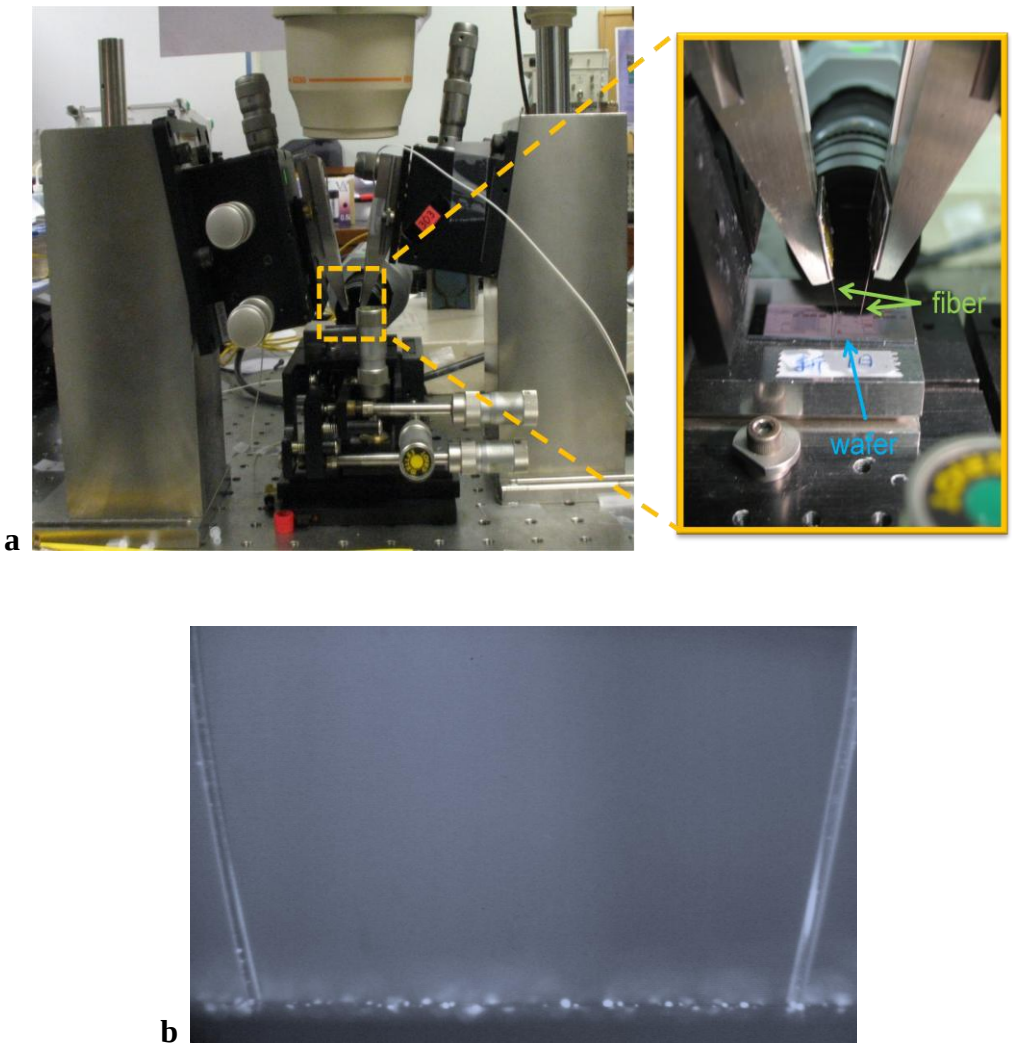

Figure 2.7 (a) The setup of optical coupling using grating couplers in practice. (b) The magnified image of fiber and waveguide in efficient coupling.

2.2.4 SOI waveguide nonlinearity

To clarify the nonlinearity of SOI waveguide, we have performed a FWM experiment in a SOI waveguide in cross section 460 nm × 220 nm and 17 mm long with effective length of 8.14 mm. The 2nd-order dispersion, also called group velocity dispersion (GVD), is calculated by applying numerical differentiation to the

effective index of the waveguide mode. The calculated GVD of quasi-TE mode is shown in Figure 2.8. By Eq. (2.23), the conversion bandwidth is about 47 nm.

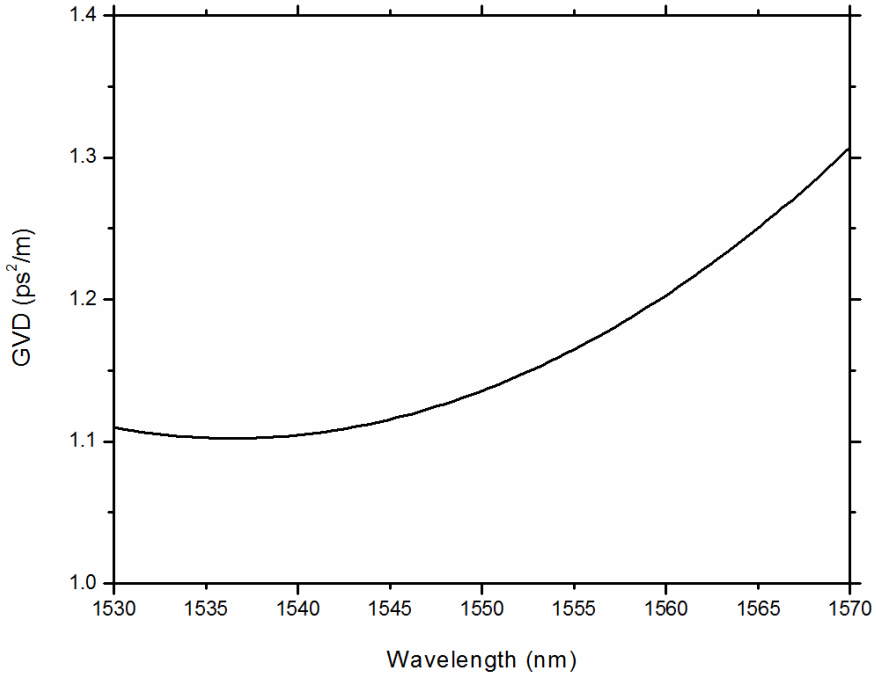

Figure 2.8 Calculated GVD of SOI waveguide.

The experimental setup is shown in Figure 2.9. A CW signal wave at wavelength 1535.5 nm and a CW tunable pump wave are first amplified by erbium-doped fiber amplifiers (EDFAs) individually. Since the grating couplers only couple quasi-TE mode, polarization controllers are inserted before EDFA. The signal and the pump

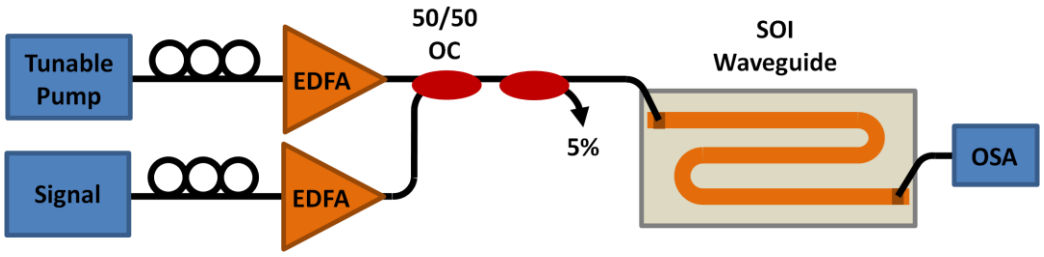

Figure 2.9 Experimental setup of degenerated FWM in SOI waveguide.

waves are combined by a 3-dB optical coupler and then 5% taped out for monitoring before coupled to SOI waveguide.

The pump wave is first set to 1549.5 nm. The optical spectrum of the 5% tapped light is shown in Figure 2.10a. There are two wavelengths with amplified spontaneous emission (ASE) from the EDFA. It ensures that this is no observable FWM before the SOI waveguide. After passing through the SOI waveguide, the optical spectrum of the output is shown in Figure 2.10b. There is clearly a new wavelength, so-called idler generated at 1563.8 nm. The conversion efficiency is about -29 dB which is ratio of idler wave to signal wave at output.

In order to measure the bandwidth of conversion efficiency, we vary the pump wavelength from 1537.5 nm to 1569.5 nm. The conversion efficiency is plotted as a function of pump-signal detuning, as shown in Figure 2.10c. We can see that the conversion efficiency drops down with the wavelength detuning. The half-width-half-maximum (HWHM) is about 20 nm which is well matched to the theoretical prediction. Compared to the results of SMF with length in order of km, these experiments show that the SOI waveguide in length of only 17 mm has better performance in FWM [70].

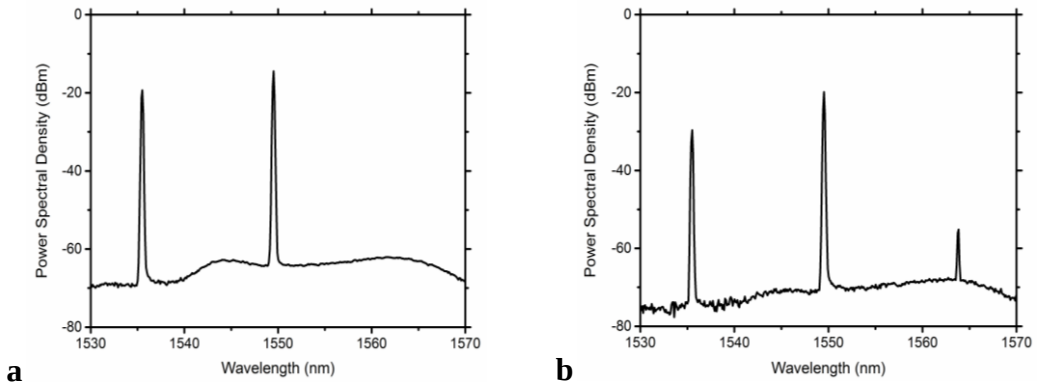

a b

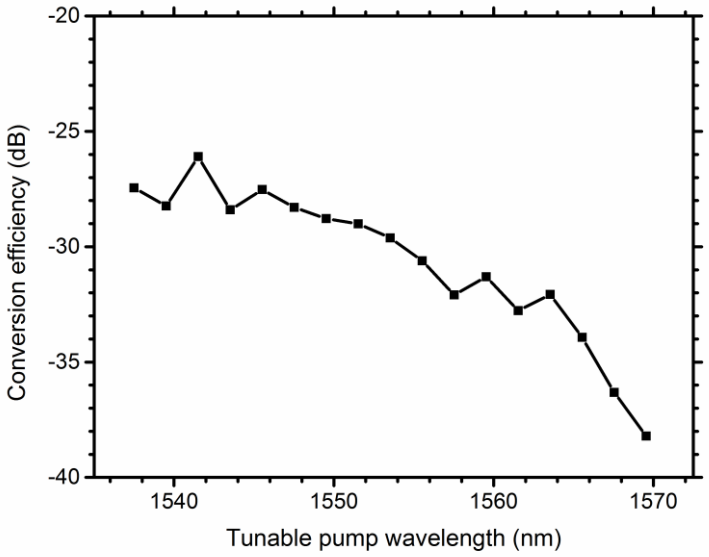

c

Figure 2.10 Optical spectra of (a) 5% input and (b) output. (c) The conversion efficiency of different pump wavelengths.

2.3 Multiwavelength laser using SOI strip waveguides and PMF Sagnac loop-based comb filter

The experimental setup is shown in Figure 2.11. An erbium-doped fiber amplifier (EDFA) having a maximum saturated power of 28 dBm was operated as the gain medium. An optical isolator ensured unidirectional operation of the ring cavity. A

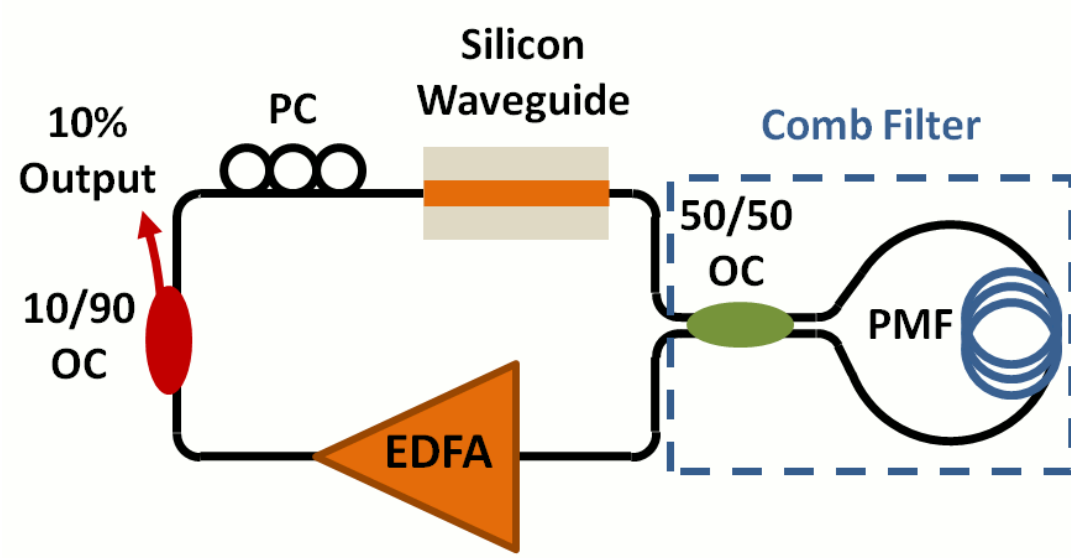

Figure 2.11 Experimental Setup of multiwavelength EDFL using SOI strip waveguides with PMF Sagnac loop-based comb filter.

SOI strip waveguide (no remaining slab) of 19 mm length was inserted after the output 10/90 optical coupler (OC) and the polarization controller (PC) following the EDFA in order to ensure reasonable optical power in the silicon for triggering FWM which stabilizes and equalizes optical power between each wavelength. The lasing wavelengths were selected by a comb filter with 0.38 nm wavelength spacing which is a polarizing-maintaining fiber (PMF) Sagnac loop consists of 13.1 meter PMF, with birefringence $\Delta n_{x\text{-}y}=0.42\times10^{-3}$, and 50/50 optical coupler (OC). It provides a sinusoidal transmission spectrum, shown in Figure 2.12. The peak insertion loss and the extinction ratio are 0.6 dB and 17.7 dB, respectively. The FWHM bandwidth is ~0.195 nm (24 GHz), about half of its FSR (48 GHz). Only the cavity modes coinciding with the comb filter resonances will be able to lase and the other cavity modes are suppressed.

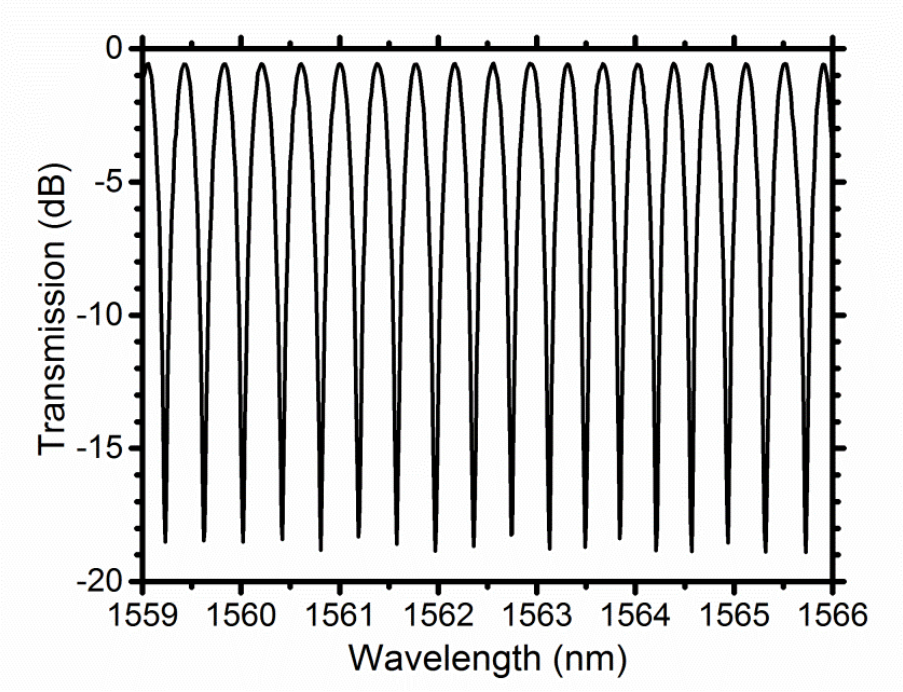

Figure 2.12 Transmission spectrum of PMF Sagnac loop-based comb filter transmission.

The total transmission spectrum of input/output grating couplers and the 19 mm SOI strip waveguide is shown in Figure 2.13. A total insertion loss of ~21 dB at 1565 nm is observed for two grating couplers and 19 mm length of SOI waveguide. Thus, the total cavity loss is ~22 dB, including the OC and the comb filter. As the grating couplers only couple the quasi-TE mode, they serve as linear polarizers inside the laser cavity. Such polarizer property introduces a wavelength dependence loss into the laser cavity due to the fiber birefringence which can be adjusted by PC.

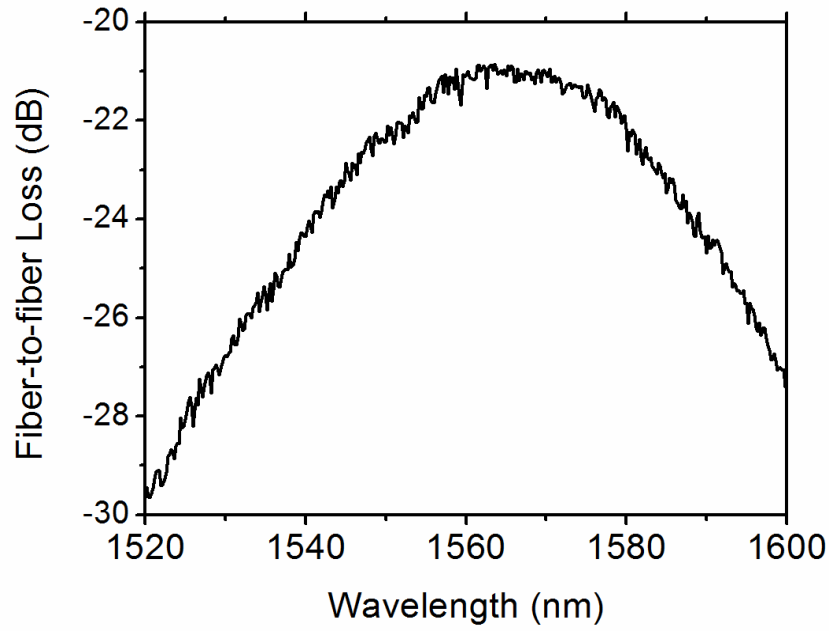

Figure 2.13 Fiber-to-fiber transmission spectra of the SOI strip waveguide with length of 19 mm.

2.3.1 Results and discussions

When the EDFA output power was increased to 27 dBm, the laser was operated in multiwavelength mode. The output spectrum of the MEDFL at room temperature is shown in Figure 2.14a. There are 5 lasing wavelengths center at 1562.26 nm with 0.38 nm spacing and within 3.2 dB channel power difference. The extinction ratio is about 20 dB. As the above discussion, a pair of grating couplers suppressed the gain maximum around 1530 nm of the EDFA as a window leading the lasing wavelength near the maximum coupling efficiency of the couplers at around 1560 nm.

In order to investigate the stability of the laser, we measured the power fluctuations of the selected wavelengths, λ_1: 1561.88 nm and λ_2: 1562.26 nm, with a

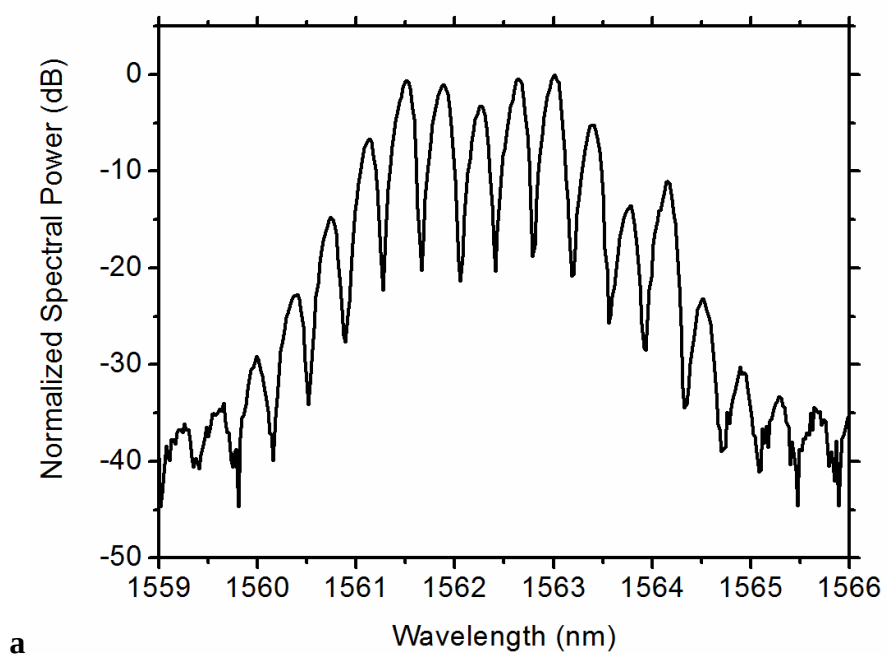

a

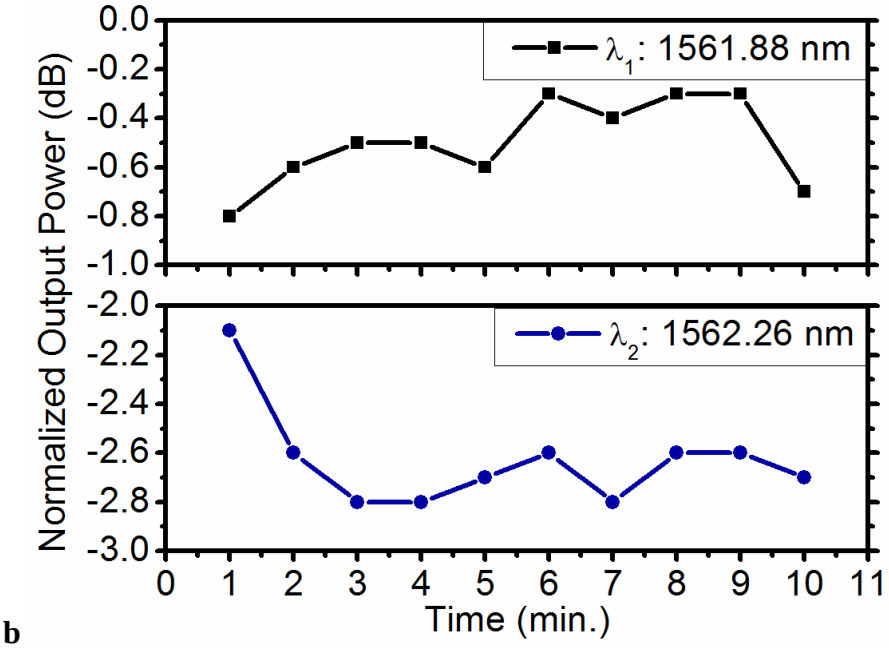

b

Figure 2.14 (a) Normalized output spectrum of the MEDFL at room temperature. (b) Power fluctuations of selected channels for 10 min.

tunable band pass filter. The output powers of those wavelengths were stable during 10 min scanning with fluctuation less than 0.8 dB, as shown in Figure 2.14b. However, the linewidths of the lasing modes are >0.15 nm. Also, the side-mode

suppression ratio is only ~3 dB. The linewidth may be due to the poor FSR/bandwidth ratio of the comber filter.

Another major concern in sensing applications is the wavelength stability which is mainly related to the stability of the comb filter. It affects the accuracy in the applications of absorption spectroscopy.

2.4 Multiwavelength laser using SOI rib waveguides and F-P comb filter

To improve the linewidth and wavelength stability of the lasers, an athermal F-P filter is used. The transmission spectrum is shown in Figure 2.15. Comparing with

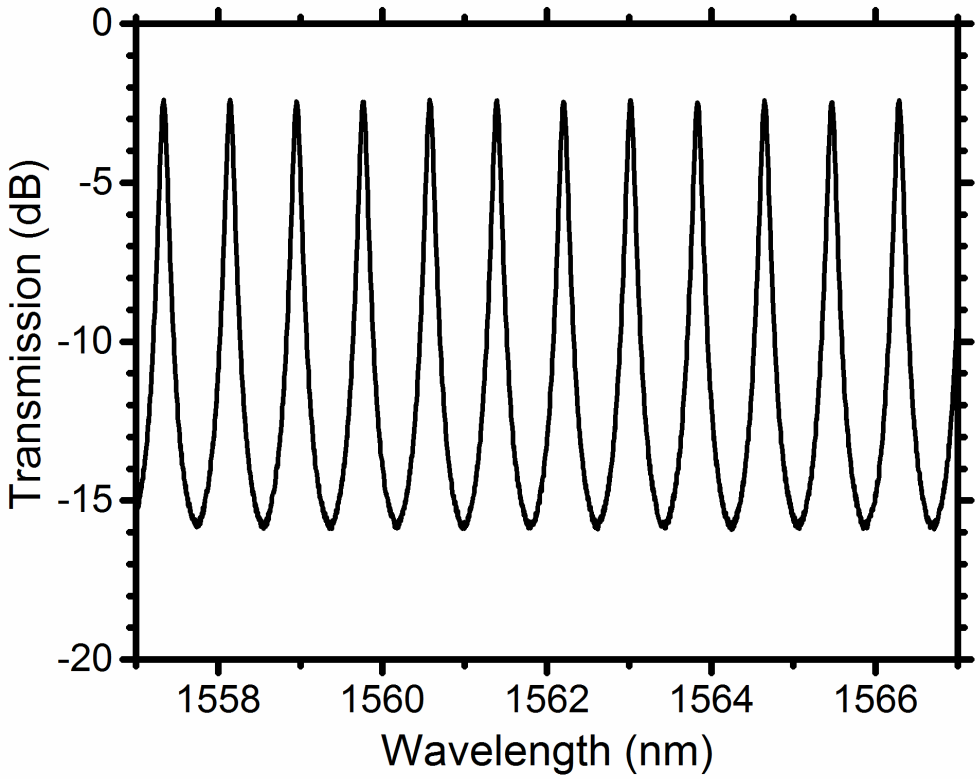

Figure 2.15 Transmission spectrum of F-P comb filter length of 19 mm.

the PMF based Sagnac loop, it provides a better free spectral range/bandwidth ratio, finesse, and average wavelength thermal stability of (100 GHz/13.1 GHz = 7.63) and ±0.08 GHz (-5–70 °C), respectively.

As FWM is proportional to the effective interaction length of the waveguides, we replace the SOI strip waveguide by a longer SOI rib waveguide (21 mm) but lower propagation loss (using newer fabrication technology). The waveguide dimension is same as the Figure 2.3 (width of 500 nm and slab height of 60 nm) which has a mode effective area and theoretical γ of 0.17 μm^2 and 59 $W^{-1}m^{-1}$ [57], respectively.

The wavelength of the maximum coupling efficiency can be changed by detuning the incident angle of the fiber. We discover that it can be easily achieved by fine adjustment of the position of the fiber relative to the grating coupler. The total transmission spectra of input/output grating couplers and the 15 mm silicon waveguide with different fiber positions are shown in Figure 2.16b. Defining the fiber position with maximum coupling efficiency of 1560 nm as position A, the center wavelength can be red-shifted by detuning the fiber position forward to the tapper along x'-axis, as shown in Figure 2.16a, reaching position B and position C. Therefore, the grating couplers serve additional role: as tunable broad bandpass filters.

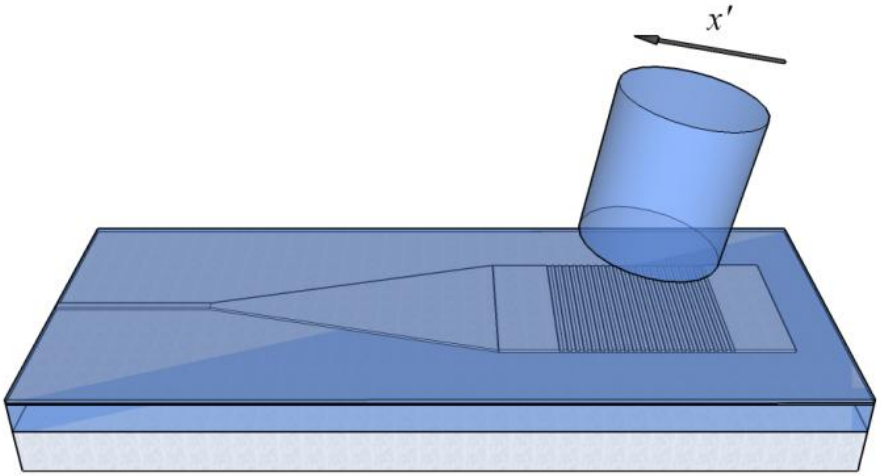

a

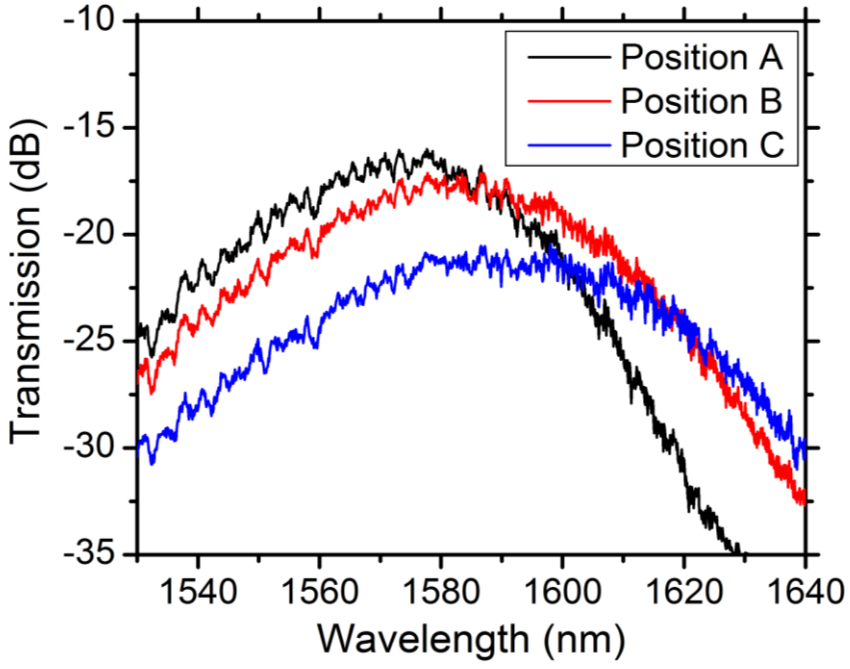

b

Figure 2.16 (a) Schematic diagram of coupling between SMF and SOI waveguide through grating coupler with fiber position moving along *x*′-axis. (b) Fiber-to-fiber transmission spectra with different fiber positions.

The new laser configuration is shown in Figure 2.17. A total insertion loss of ~17.5 dB at 1560 nm is observed for two grating couplers and 21 mm length of SOI length

waveguide. Thus, the total cavity loss is cavity loss is ~20.5 dB, including the OC and the comb filter.

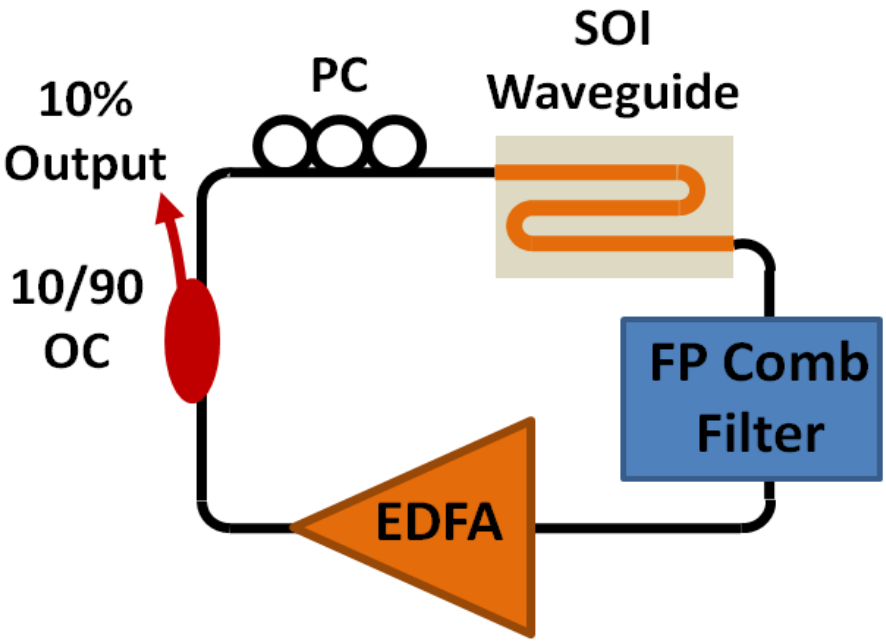

Figure 2.17 Experimental Setup of multiwavelength EDFL using SOI rib waveguides with F-P comb filter.

2.4.1 Results and discussions

To verify the contribution of FWM to the laser stabilization, the laser output characteristics with different pump power was investigated. When the output power of EDFA was set to 2.5 dBm, one channel started lasing stably at 1562.54 nm. As the power reached 10.5 dBm, the output spectrum became unstable. Another channel at 1563.34 nm started lasing and competed with the former one (see Figure 2.18 (center), which shows snapshots of the spectra over a 3 minute time interval). The output spectrum at any given time only has one channel dominant or two channels coexisted. The individual channel peak power fluctuations are larger than 25 dB in a short 3 minute observation interval. At the low output powers, there is insufficient

FWM to exchange power among the channels to overcome the gain competition and stabilize the output [52]. The number of lasing channels was increased gradually with the EDFA output power, as shown in Figure 2.18 (right). The channel peak powers also became more stable as the EDFA output power was increased.

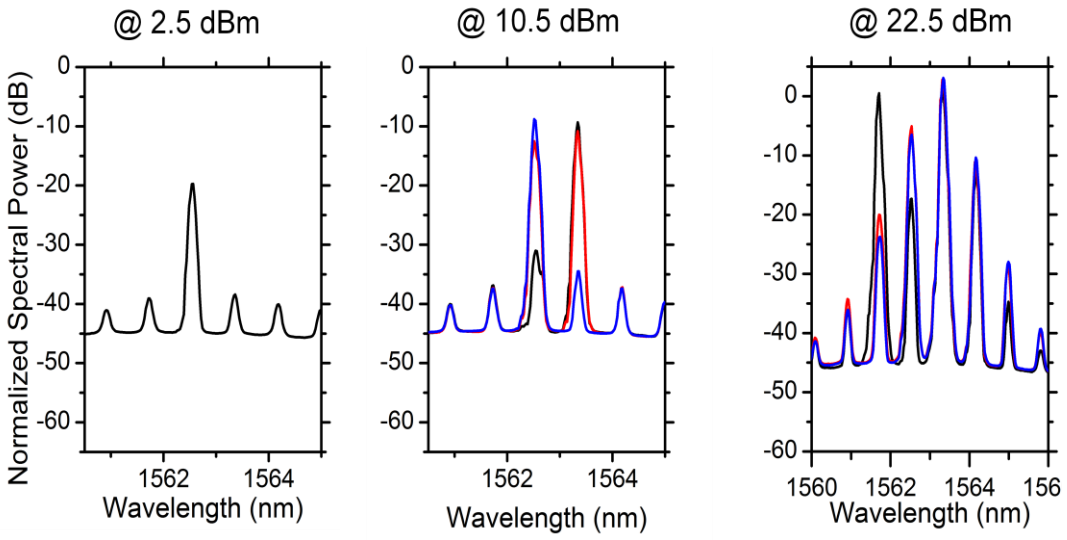

Figure 2.18 The typical output spectra of 3 min scanning at different EDFA output powers: 2.5 dBm (left), 10.5 dBm (center), and 22.5 dBm (right).

When the EDFA output power was increased to 27 dBm, the laser was operated in multiwavelength mode. The output spectrum of the MEDFL at room temperature is shown in Figure 2.19a. There are 5 lasing wavelengths center at 1562.53 nm with ~0.8 nm spacing and within 2.8 dB channel power difference. By using the F-P comb filter, the extinction ratio is increased to over 40 dB. The side-mode suppression ratio is increased to ~15 dB. The line width is less than 0.01 dB which is limited by the resolution of the optical spectrum analyzer. Similar to the previous results, the lasing wavelength is near the maximum coupling efficiency of the couplers.

In order to investigate the stability of the laser, we measured the power fluctuations of the selected wavelengths, λ_1: 1561.71 nm and λ_2: 1563.34 nm, with tunable band pass filters. The output powers of those wavelengths were stable during

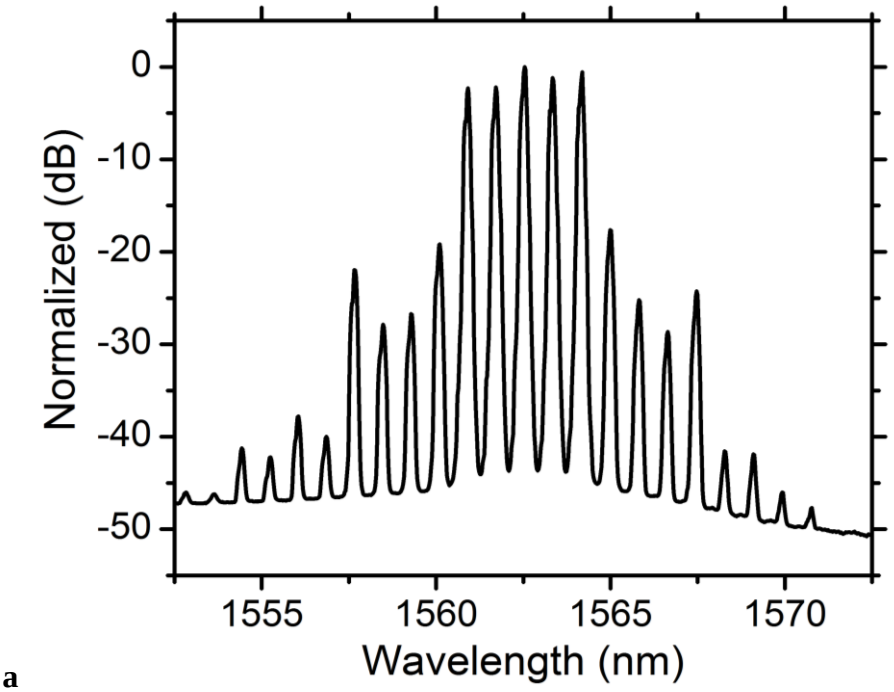

a

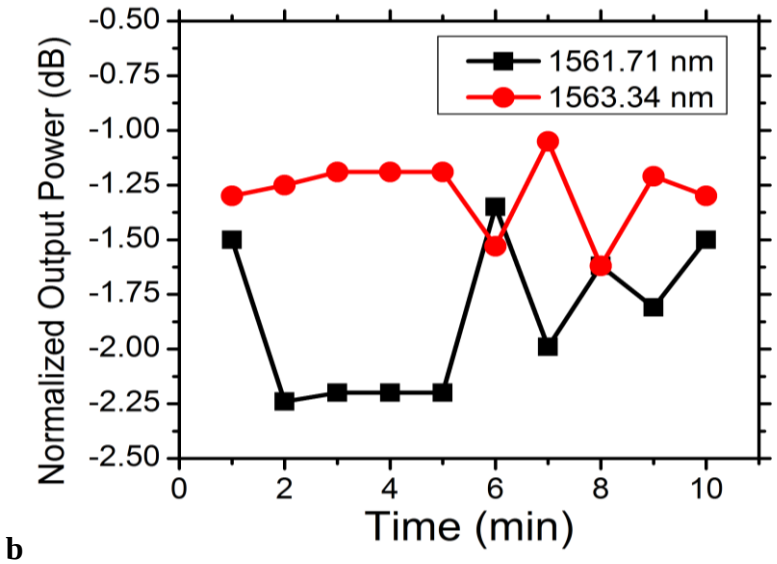

b

Figure 2.19 (a) Normalized output spectrum of the MEDFL at room temperature. (b) Power fluctuations of selected channels for 10 min.

10 min scanning with fluctuation less than 1 dB, as shown in Figure 2.19b. The laser has better performance than the last one in even wider wavelength difference. It suggests the FWM is more efficient in the lower loss SOI waveguide.

2.5 Reverse biased p-i-n SOI waveguides

To further improve the laser, we try to further decrease the propagation loss of the waveguide. We focus on the nonlinear loss at that moment. To reduce FCA generated by TPA in high power regime, a rib waveguide structure with a reverse-biased p-i-n diode was applied [71]. The fabrication process is the deep-UV lithography technology from the Institute of Microelectronics (IME), Agency for Science, Technology and Research (A∗STAR), Singapore, the details are refer to [72].

The new laser configuration is shown in Figure 2.20a. From the transmission spectra of the new waveguides, the total insertion loss of ~15 dB at 1560 nm is observed for two grating couplers and 15 mm length of SOI waveguide, as shown in Figure 2.20b. As the last waveguide, the coupling efficiency can be detuned by the fiber positions. The total cavity loss is ~18 dB, including the OC and the comb filter.

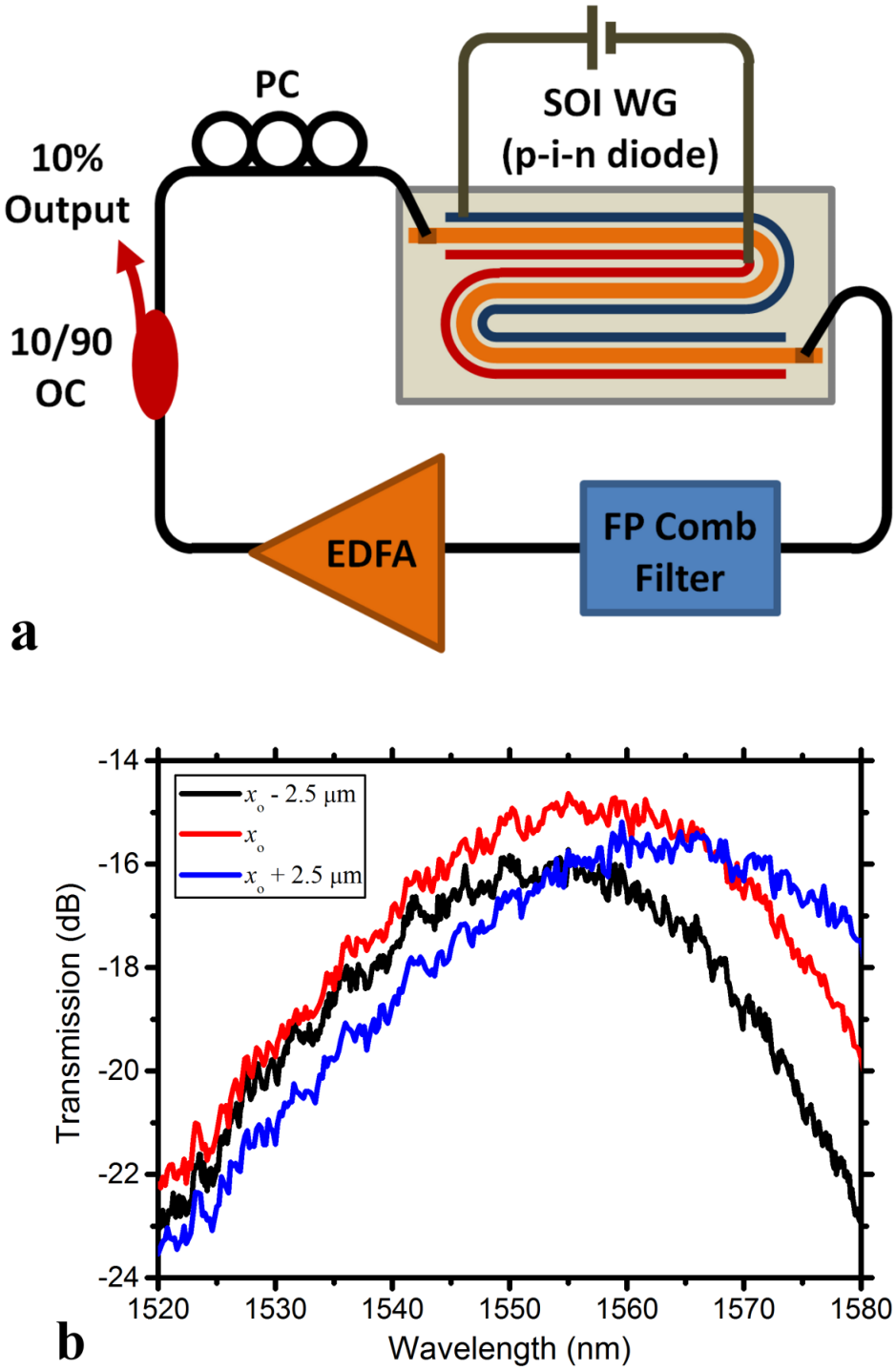

Figure 2.20 (a) Schematic diagram of experimental Setup of MEDFL using SOI rib waveguides (p-i-n diode) with F-P comb filter. (b) Fiber-to-fiber transmission spectra of SOI waveguide with different fiber positions.

2.5.1 Results and discussions

When the output power of EDFA was set to 8 dBm and without any reverse-bias applied to the SOI waveguide, one channel started lasing stably at 1564.1 nm. As the power reached 22 dBm, the output spectrum became unstable. Another channel at 1563.3 nm started lasing and competed with the former one, as shown in Figure 2.21a. The individual channel peak power fluctuations are larger than 40 dB in a short 3 minute observation interval. Similar to the previous version, the number of lasing channels and the channel power stability were increased gradually with the EDFA output power. However, the uniformity of channel peak powers was not good and had up to 10 dB power difference.

Without the reverse-bias, the nonlinearity of the SOI waveguide was insufficient to equalize the lasing channels since the waveguide is not long enough as the previous waveguide. Moreover, the effective interaction length of FWM in the waveguide was limited by FCA.

To equalize the laser channel powers, the EDFA output power was increased to 28 dBm. A reverse-bias of 4.0 V was applied to the diode to increase the effective length of the waveguide by removing the free-carriers, which generated a photocurrent of 10.1 mA. By adjusting the optical fiber position and PC to optimize the wavelength dependent loss, a stable output spectrum of the multiwavelength EDFL at room temperature was achieved, as shown in Fig. 3b. There are six lasing wavelengths between 1560.9-1564.9 nm with 0.8 nm spacing. The power difference among wavelengths is within 1.8 dB. The extinction ratios and the side-mode-suppression are over 49 dB and over 10 dB, respectively. There is some periodic

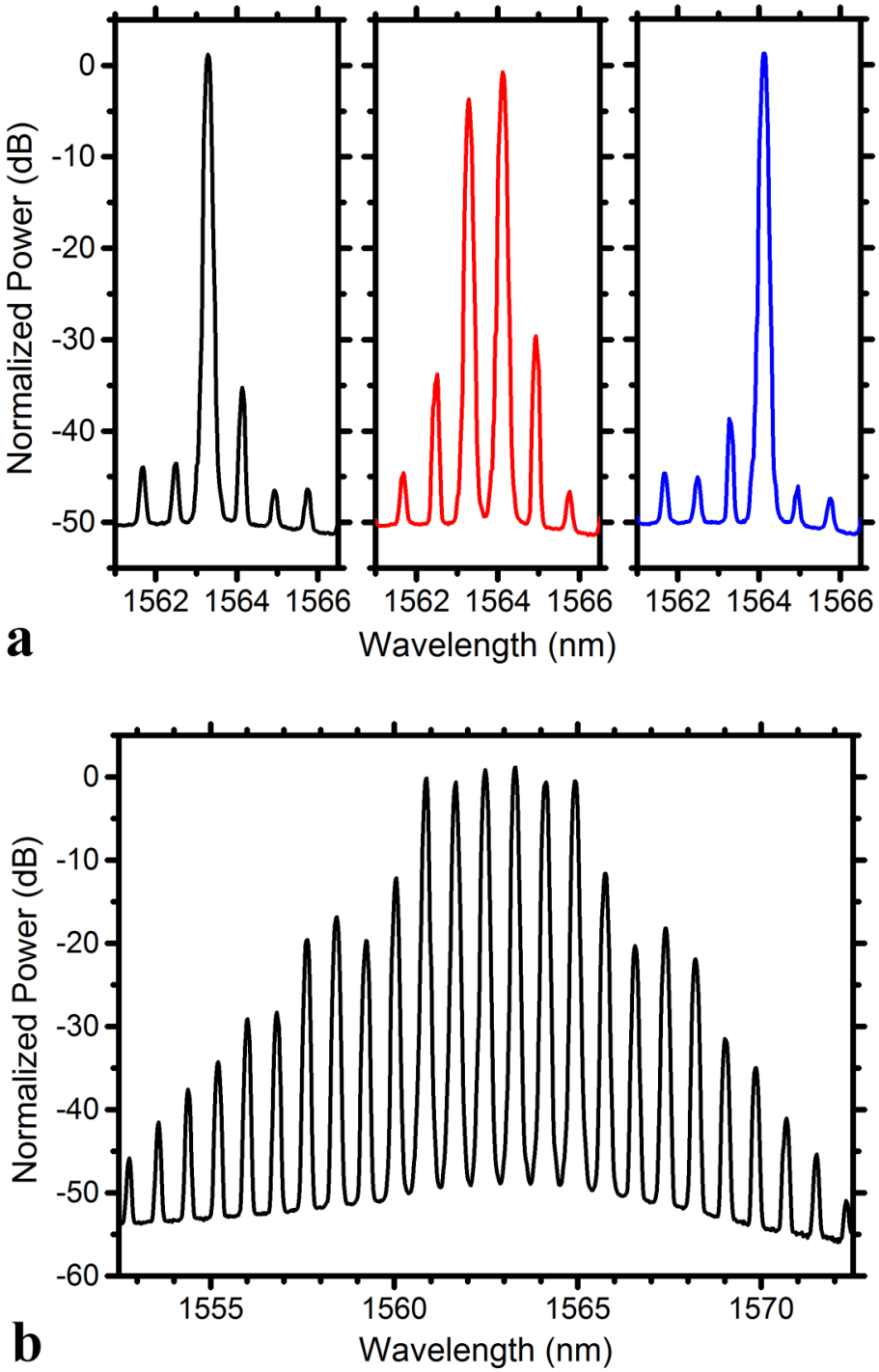

Figure 2.21 (a) The typical output spectra of 3 minutes scanning at 22 dBm EDFA output power without reverse-bias. (b) Multiwavelength output spectrum of the laser at 28 dBm EDFA output power with reverse-bias of 4.0 V.

variation to the peak power of the different modes. It may be due to F-P interference inside the SOI waveguide produced by the weak back reflections between the pair of grating couplers and seen as small, repeatably measured, fluctuations in the spectral transmission characteristic of the grating couplers in Fig. 2b. Fig. 2b also shows that the grating coupler has higher loss at the wavelength of erbium gain peak, around 1530 nm, and thus the laser operated in a wavelength window around 1560 nm.

The laser stability was verified by repeating the spectral measurements over 20 minutes, as shown in Figure 2.22a. Figure 2.22b shows the channel power evolution of the laser respect to time over a 2 minutes interval. The power fluctuation per channel over a 20 minute period is less than 0.65 dB. The laser was obviously more stable than Fig. 3a in terms of power stability. Mechanical/thermal drift in the fiber-waveguide alignment may also contribute to some of the power fluctuation. The power stability may be sufficient for some sensor applications, e.g. gas sensing. Moreover, the stability requirement of sensing applications can be relaxed by using differential detection method, which is similar to the design used in balanced detectors [73]. In order to further improve the power stability, this may be done in future by fixing the fiber position by (index matching) epoxy [74].

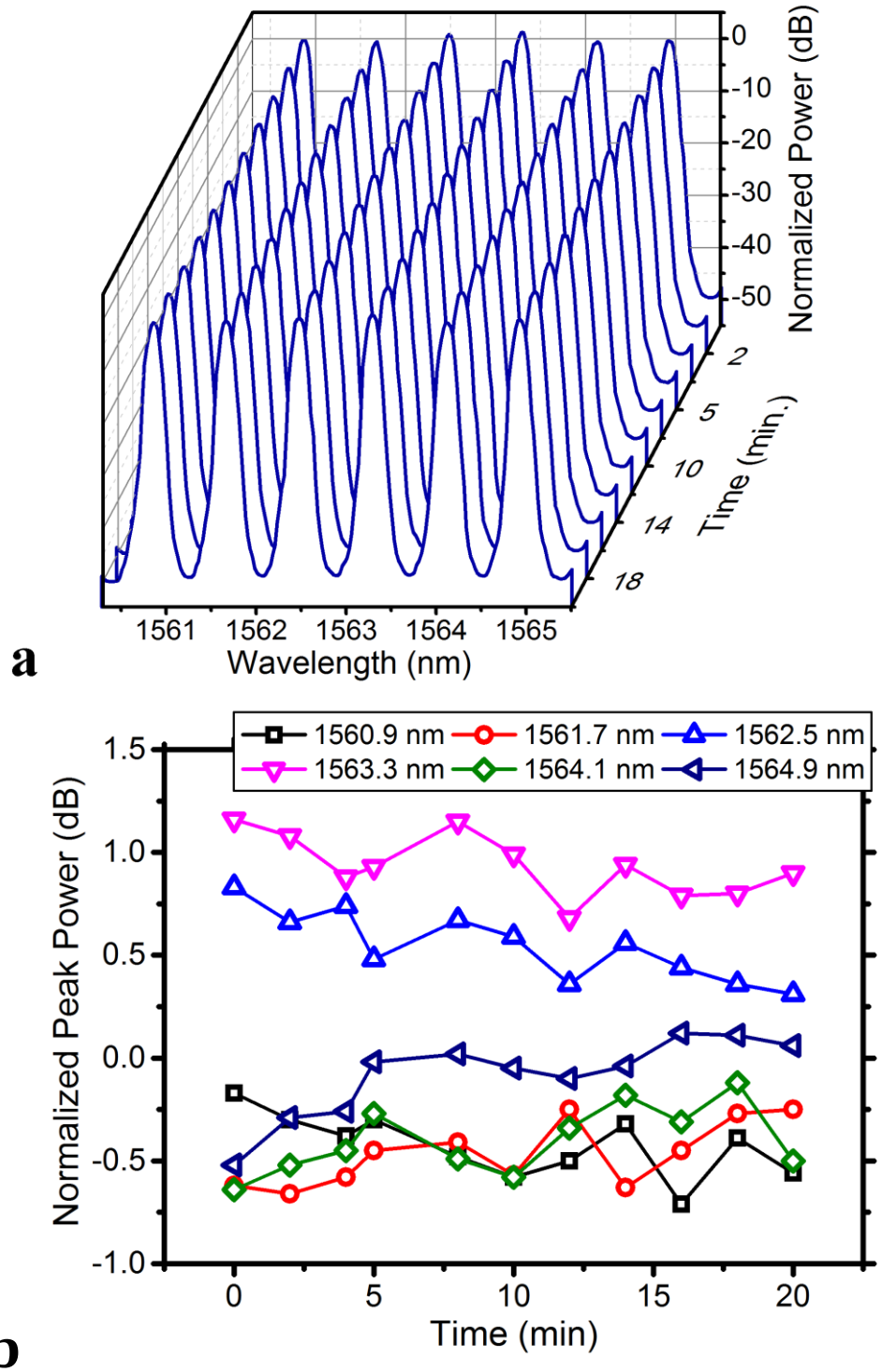

Figure 2.22 (a) Repeated scanning spectra for every 2 minutes. (b) Channel peak power evolution of the laser respect to time over 20 minutes.

As FWM maintains a definite phase relationship among the lasing modes [52], the combined wavelengths output will have 100 GHz beating due to the comb filter and also exhibit some evidence of mode-locking because of the well defined phase relationship among the modes. We measured autocorrelation of the combined wavelengths output, to examine their coherence and temporal characteristics, as shown in Figure 2.23. The experiment results clearly show a ~100 GHz beating, confirming the coherent relationship among the 100 GHz spaced wavelength outputs. It is clear evidence that these modes have interaction through FWM. Furthermore, the other possible nonlinearities in the cavity, such as simulated Raman scattering (SRS) and stimulated Brillouin scattering (SBS), are negligible. It is because the Stokes shift of SRS in silicon operates only over a narrow bandwidth (<100 MHz) at

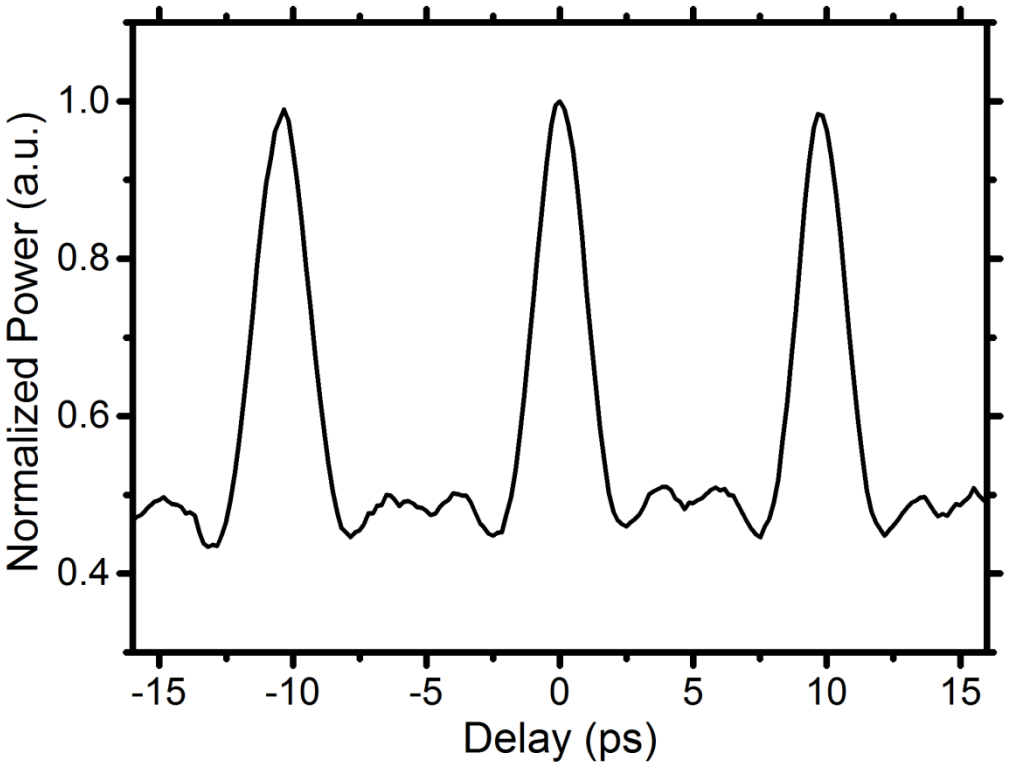

Figure 2.23 The autocorrelation trace of the multiwavelength output.

15.6 THz detuning from the pump which is blocked by grating couplers [56], while the magnitude of SRS or SBS in only ~3 m SMF at this optical power level is much weaker than FWM in SOI waveguide.

To further investigate the effect of FCA and reverse-bias in power equalization, the output spectra measured for different reverse-biases across the diode are shown in Figure 2.24. The power level difference among modes is increased from 1.8 dB to 3.1 dB when the reverse-bias is reduced from 4 to 0 V (short circuit). If no external circuit is connected to the diode (open circuit), the power level difference increases further to 5.9 dB. The reverse-bias and external circuit increase the effective length of the waveguide by reducing the optical loss from FCA, and thus increase the FWM and power exchange rate between the laser channels: the results clearly show that the

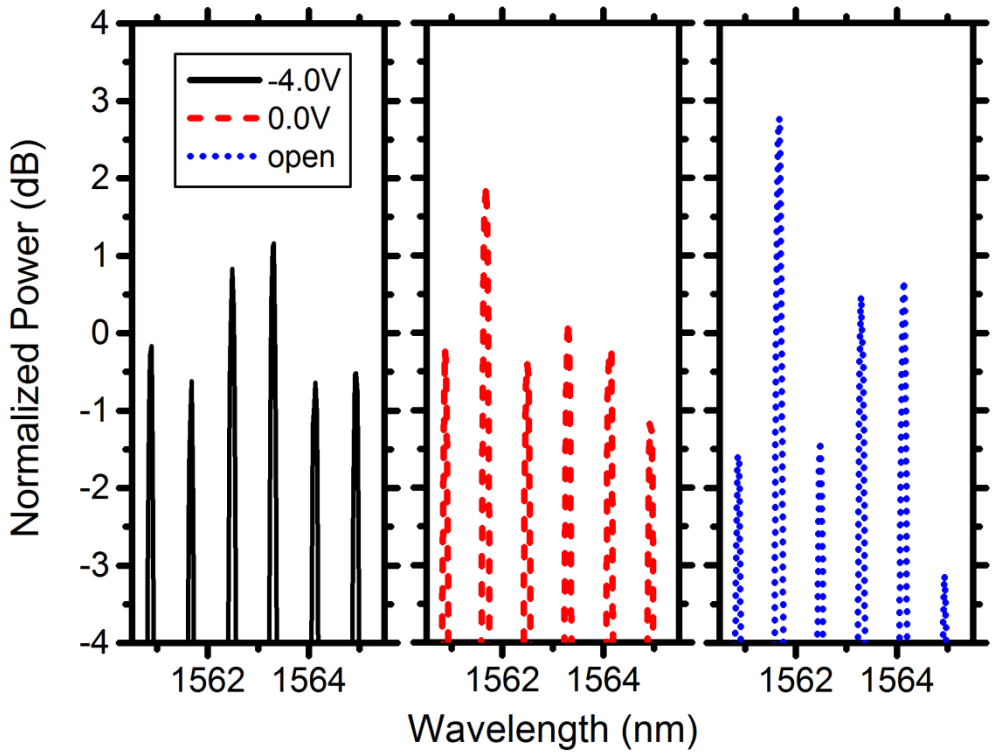

Figure 2.24 The output spectra of different reverse-bias voltages.

power equalization from FWM is enhanced by reverse-bias. Compared with our earlier work without a reverse-biased diode, the removal of the free carriers allows the fiber laser to support more lasing channels and more channel power stability with a shorter waveguide.

The number of equalized channels and power level requirement for the multiwavelength operation mainly depend on the FWM effect in SOI waveguide and the gain bandwidth of the laser cavity. The FWM process is limited by the insertion loss of the input grating coupler and the interaction length due to waveguide linear propagation loss, besides FCA suppressed by reverse-biased p-i-n diode. The insertion loss of the SOI chip can be potentially reduced to ~4.7 dB using the apodized grating couplers with 1.2 dB loss and waveguides with losses of about 1.5 dB/cm [75], [76], therefore, relaxing the power level requirement. The cavity gain bandwidth is limited by the bandwidth of the grating couplers which can be increased by the use of wideband grating couplers [77]. Moreover, by designing the center wavelength of the grating coupler towards longer wavelengths with the use of L-band EDF, it is possible to produce L-band multiwavelength operation for gas sensors, e.g., carbon dioxide around 1572 and 1578.6 nm [39].

As shown in Figure 2.23, the output wavelengths of the laser superpose coherently to generate 100 GHz pulses. However, the major challenge is achieving single longitudinal mode lasing for each wavelength, otherwise, the cavity mode coupling, with frequency spacing in the order of MHz, will affect the temporal stability. In our proposed laser, the average FWHM of the F-P filter is 0.107 nm (13.1 GHz) which is much wider than cavity mode-spacing. It is not sufficient to suppress the cavity mode coupling. A possible approach towards single longitudinal mode lasing in each line

of the frequency comb is to cascade comb filters to reduce the number of cavity modes via Vernier effect [78].

2.5.2 Conclusion

In conclusion, we first demonstrated a MEDFL based on FWM in SOI strip waveguide with PMF-based Sagnac loop comb filter. Five lasing wavelengths centered at 1562.26 nm with 0.38 nm spacing were achieved. The output powers of those wavelengths were stable during 10 min. scanning with fluctuation less than 0.8 dB at room temperature.

In order to improve the line width and the thermal stability, athermal F-P comb filter and longer (and lower loss) SOI rib waveguide were used. Five lasing wavelengths with 0.8 nm spacing were achieved. The extinction ratio and the side-mode suppression ratio are increased to over 40 dB and ~15 dB, respectively. The power fluctuations of selected channels were less than 1 dB during 10 min scanning.

By employing a reverse-bias to remove the free carriers generated by TPA in the SOI waveguide, we have demonstrated a multiwavelength EDFL with six lasing wavelengths between 1560.9-1564.9 nm. The power fluctuation per channel (all six channels) is less than 0.65 dB.

The proposed silicon/erbium-doped fiber hybrid ring laser provides a potentially compact and low cost solution for possible applications in integrated WDM gas sensors.

3 Nonlinear microresonators & dissipative four-wave mixing mode-locking

3.1 Introduction

In previous chapter, we have demonstrated the FWM multiwavelength EDFL for optical sensing using a nonlinear SOI waveguide and a F-P comb filter. In system integration, it is natural to integrate these two components into a single chip. In silicon photonic platform, the F-P comb filter can be replaced by a MRR. MRR has almost the same spectral behavior as the F-P filter except the wave propagation direction. In fact, we can even further integrate the SOI waveguide and the MRR into a single device: nonlinear silicon MRR. This device can take advantage of the resonation enhancement to reduce the footprint of the whole system. It will be discussed in the following section in details.

Moreover, the autocorrelation trace of the combined multiwavelength output shows that such kind of FWM multiwavelength laser with comb filter has an pulsation output with ultrahigh repetition rate, up to hundreds GHz. This results link the multiwavelength lasers to another type of lasers: passive mode-locked fiber lasers based on DFWM [79], [80]. By adding an intracavity comb filter, only the cavity modes coinciding with the comb filter will be able to lase and the other cavity modes are suppressed. The lasing modes are phase-locked by FWM through the Kerr nonlinear medium. The resulting output would be a pulse train in high repetition rate. Recently, in order to suppress the instability due to the long cavity length, a new

scheme employing a high-*Q* silica MRR as both the Kerr medium and the comb filter, named FD-FWM, was demonstrated stable operation at 200 GHz [81].

This kind of lasers can be the potential solution for the demands of the recent advances in optical communication for the high speed applications such as optical clocks. Also, they can also act as the coherent optical comb source for high spectral efficiency modulation schemes such as OFDM. Recently, optical OFDM employing silicon photonic devices have been reported [82], [83]. High repetition rate mode-locked pulse source directly generated in silicon waveguide using FD-FWM with nonlinear silicon MRR provides an attractive solution for making integrated OFDM systems and on-chip optical clocks.

In fact, optical comb source in integrated platform can be provided by OPO. It has been demonstrated in high *Q* silica and silicon nitride microresonators recently [84]. For silicon MRR, although the *Q* of silicon MRRs are typically lower than the silica and silicon nitride by 1-2 orders of magnitude, their higher nonlinearity can compensate for the lower *Q*. However, the TPA and resultant FCA in SOI [56], [71] will limit the parametric gain inside the waveguide and is the major impediment for efficient silicon based OPO [84]. FD-FWM provides an alternative solution for comb generation, by moving the gain mechanism to EDF.

In this chapter, we employed a nonlinear silicon MRR with reverse-biased p-i-n to demonstrate a FD-FWM mode-locked laser. A stable mode-locked laser with 100 GHz mode spacing is achieved at high pump powers.

3.2 Dissipative four-wave mixing

Passive mode-locked fiber lasers have been used in many applications such as optical spectroscopy, medical sensing and optical communication. However, the repetition rate is typically limited by the cavity roundtrip time, resulting in repetition rates below 200 MHz which limit the usage in high speed optical communication. In order to increase the fiber laser repetition, many different approaches have been proposed [85], [86]. The most straightforward approach is simply making a very short cavity in order to reduce the round trip time such as integrated semiconductor lasers which repetition rate can be up to 400 GHz [85], [87], [88]. However, the line quality is worse than usual fiber laser. Another approach is combining active and passive mode-locking schemes, so-called hybrid mode-locking. However, the repetition rate is limited by the speed of the optical modulators which is below 100 GHz [89].

In order to preserve the line quality with hundreds GHz repetition rate, a comb filter insert to the fiber laser cavity with nonlinear medium has been proposed by Yoshida et al. in 1997 [79]. The experimental setup is shown in Figure 3.1a. The F-P filter has FSR of 115 GHz and finesse of 75.5. The nonlinear medium is the polarization-maintaining dispersion-shifted fiber (PM-DSF) with the length of 1.2 km. The optical spectrum and the autocorrelation trace of the laser out are shown in Figure 3.1b. They show the laser has 115 GHz mode spacing and the corresponding pulsation output. A year after, this type of laser has been proposed again theoretically and independently by Quiroga-Teixeiro et al. who also named it to DFWM mode-locking [80].

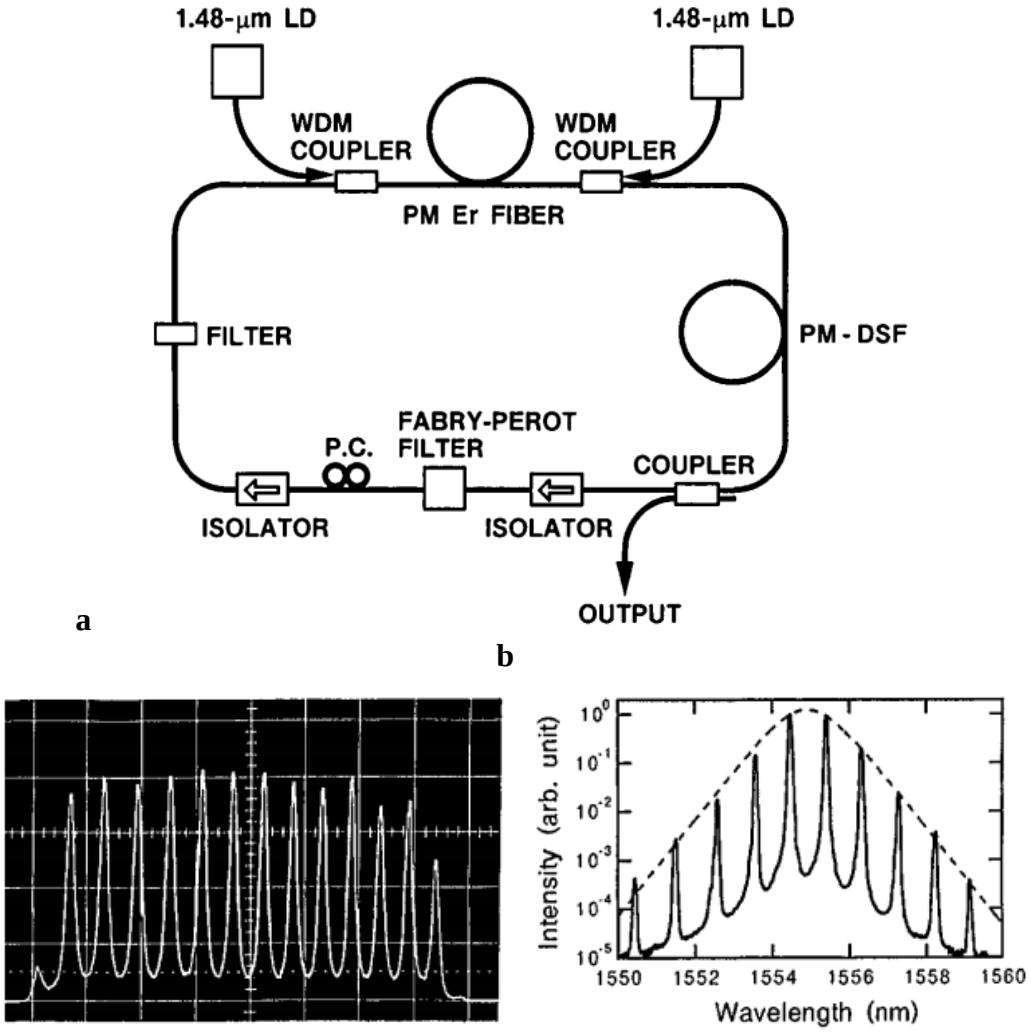

Figure 3.1 (a) The schematic diagram of the laser configuration. (b) The autocorrelation trace (left) and the optical spectrum (right) of the laser output. Figures are adapted from [79].

Quiroga-Teixeiro et al. started from the nonlinear Schrödinger (NLS) equation [65]. First, they consider the optical wave with center frequency ω_0, as Eq. (2.8) while the other frequency components are absorbed to the amplitude of the center frequency, $A(z,t)$. By assuming $A(z,t)$ as the slowly varying wave envelope and the waveguide without gain or loss, the evolution of $A(z,t)$ can be described by NLS equation:

$$\frac{\partial}{\partial z}A = -i\frac{\beta''}{2}\frac{\partial^2}{\partial T^2}A + i\gamma|A|^2 A, \tag{3.1}$$

where T is the time of the frame propagates with the wave at the group velocity v_g ($T = t - z/v_g$), and γ is the nonlinear coefficient in Eq. (2.13). We introduce a spectral (dispersive) dependent gain $g(\omega)$ with two peaks equally separated from center frequency ω_0:

$$g(\omega) = g_0 + \beta_g \omega^2 - \kappa_g \omega^4, \tag{3.2}$$

where ω is the frequency respect to ω_0. Figure 3.2 shows the gain spectrum of $g(\omega)$. There are two peaks in the gain region. Outside the gain region, the light experiences net loss.

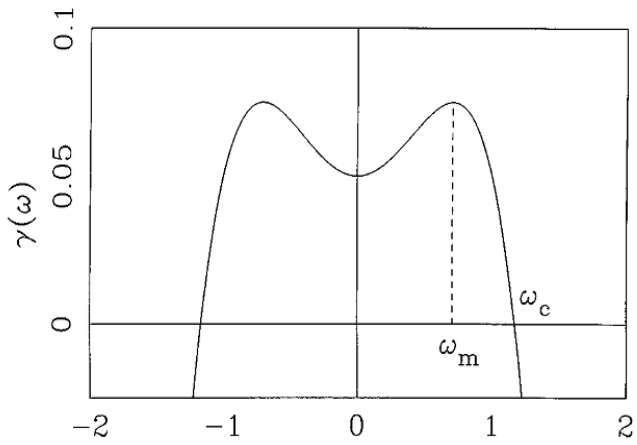

Figure 3.2 The gain spectrum of spectral (dispersive) dependent gain $g(\omega)$. The figures is adapted from [79] which uses $\gamma(\omega)$ to represent $g(\omega)$.

By using Fourier transform, Eq. (3.2) can be transformed to time domain,

$$g(T) = g_0 - \beta_g \frac{\partial^2}{\partial T^2} - \kappa_g \frac{\partial^4}{\partial T^4}. \tag{3.3}$$

By inserting Eq. (3.3) into the NLS equation:

$$\frac{\partial}{\partial z} A = -i\frac{\beta''}{2}\frac{\partial^2}{\partial T^2} A + i\gamma|A|^2 A + \left[g_0 - \beta_g \frac{\partial^2}{\partial t^2} - \kappa_g \frac{\partial^4}{\partial t^4} \right] A, \tag{3.4}$$

the system becomes a Ginzburg–Landau type equation:

$$\frac{\partial}{\partial z} A = \left[g_0 - (i\frac{\beta''}{2} + \beta_g)\frac{\partial^2}{\partial t^2} - \kappa_g \frac{\partial^4}{\partial t^4} \right] A + i\gamma|A|^2 A. \tag{3.5}$$

This type of equation has attracted a considerable interest from the studies of pattern generations and self-organization. Because of it does not have analytical solution, it has to be solved by numerical method. The most commonly used method for this kind of problem is split-step Fourier method [65]. The initial condition of the system is set as a random white noise which simulates the starting ASE from the gain medium. After several hundreds of round trip of the cavity, the system converges to a static state. However, the results depend on the frequency spacing (length of the time window T) and the initial condition. A stable static solution can be achieved for T = 8 (frequency resolution ≈ 0.785 Hz). The spectrum of the static state is shown in Figure 3.3a. There are mainly two wavelengths lasing around the gain peaks with equal amplitude. These two wavelengths generate some harmonics through FWM while those harmonics are at the region of net loss. The system is balanced by transferring the energies from two major wavelengths with gain to their harmonics

with loss. As the energy loss through FWM, the name of this mode-locking scheme has word “dissipative”. If the time window is increased, the results become more independent to the initial condition and converge to similar solution. Figure 3.3b shows the static solution at time domain for T = 100. We can see that a pulse train is formed with the repetition rate equals to the frequency difference between two gain peaks. This system was experimentally demonstrated again using a non-chirped fiber Bragg grating (FBG) filter in 2001 [90].

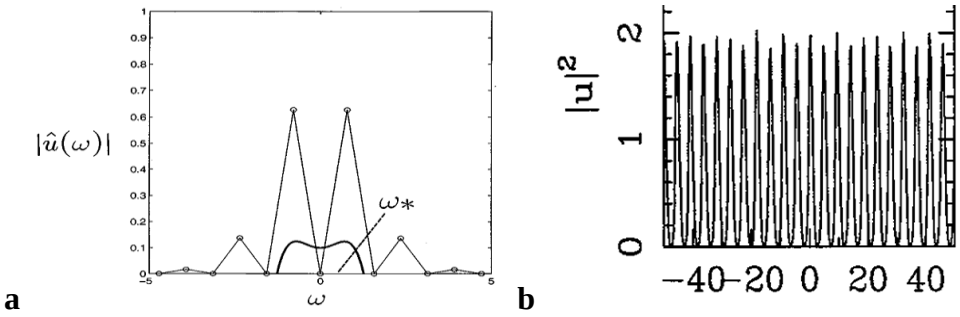

Figure 3.3 (a) The frequency spectrum of the static state (T = 8). (b) Static solution at time domain (T = 100). Figures are adapted from [79] which use $u(z,t)$ to represent $A(z,t)$.

3.2.1 Supermode noise

As a pulse source with repetition rates up to 100 GHz, the temporal and power stabilities of DFWM mode-locking are very crucial in practice. The laser stabilities have been studied by Schröder et al. in 2008 [78]. The laser configuration was based on a Raman fiber laser using HNLF of 1 km as the gain medium, shown in Figure 3.4. The comb filter was a FBG filter with 100 GHz frequency spacing.

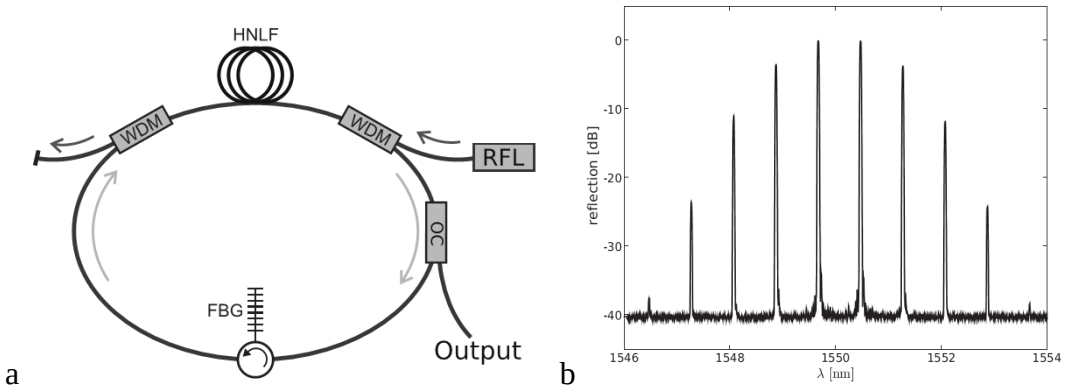

Figure 3.4 (a) Experimental setup. (b) Reflection spectrum of the FBG. Figures are adapted from [78].

When the pump power was increased to 2.22 W, the laser operated under DFWM. The corresponding optical spectrum and the autocorrelation trace are shown in Figure 3.5. We can see a 100 GHz pulses in the autocorrelation trace. However, there are also some kinds of sub-pulses between the regular pulses.

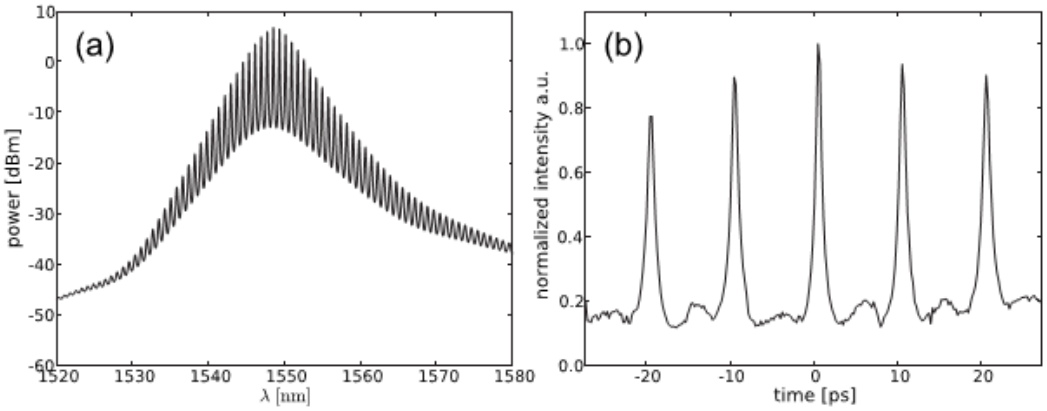

Figure 3.5 (a) Output spectrum and (b) autocorrelation of the laser at pump power of 2.22 W. Figures are adapted from [78].

In order to clarify the source of these sub-pulses, Schröder et al. performed a numerical analysis based on the one used by Quiroga-Teixeiro et al.:

$$\frac{\partial}{\partial z}A + i\frac{\beta''}{2}\frac{\partial^2}{\partial t^2}A = i\gamma|A|^2 A + \frac{g_0}{1+Q/I_s}A - \alpha A. \tag{3.6}$$

where Q, I_S, g_0 and α are the average normalized power, saturation parameter, small signal gain of the EDFA, and waveguide amplitude absorption coefficient, respectively. Eq. (3.8) can be further normalized:

$$\frac{\partial}{\partial \zeta}U + i\kappa\frac{\partial^2}{\partial \tau^2}U = i|U|^2 U + \frac{G}{1+Q/I_s}U - lU\,,$$
$$\zeta = \frac{z}{L}, \tau = ft, U = \frac{A}{\sqrt{P}}, P = \frac{1}{\gamma L}, \kappa = \frac{\beta'' f^2 L}{2}, G = g_0 L, l = \alpha L\,, \tag{3.7}$$

where L is there cavity length, f is the FSR of the F-P filter. Since Quiroga-Teixeiro et al. has made the assumption of short cavity, it may not be suitable for general long cavity fiber laser. Therefore, instead of expressing the wavelength selective gain inside the Ginzburg–Landau type equation, Schröder et al. multiply the intracavity field U by a comb filter function.

The autocorrelations of the simulated result is shown in Figure 3.6a which obviously shows a number of subpulses similar to the experimental results. The origin of these subpulses can be explained by the pulse trains in the original solution, as shown in Figure 3.6b. There are several brunches of individual pulse trains exist in the cavity simultaneously. They have the repetition rates slight different from the

frequency spacing of the comb filter. As mentioned in Section 2.5.1, this is due to the FWHM of the filter is too wide compared with the laser cavity mode spacing. The large number of modes allowed to exist in the cavity causes the "supermode noise" which has been studied deeply in active mode-locking [91], [92], [93], [94]. It makes a number of possible frequency combinations for the coupling among those modes. Those coupled modes of different frequency spacing superpose to generate the pulses train with different repetition rates. Since the frequency spacings of those pulse trains are different, they cannot maintain a phase relationship through FWM efficiently and behave independently. As those pulse trains have a slight phase shift among each other, their overlap resulting subpulses in the autocorrelation trace.

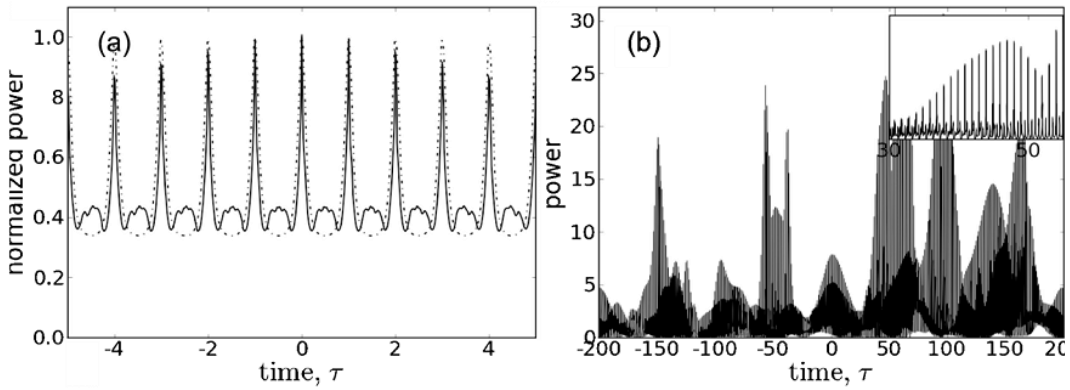

Figure 3.6 (a) Simulated autocorrelation of low, κ =−0.001, G=1, α=0.4, I_S=1 (dashed curve), and high, G=2 (solid curve) gain. (b) Temporal profile of the optical intensity of the high-gain. Figures are adapted from [78].

To suppress the supermode noise, one approach is to narrow the FWHM bandwidth of the comb filter. However, it is hard to achieve the FWHM bandwidth down to the order of MHz in conventional comb filter. Another approach is decreasing the number of cavity modes by insert several sub-cavities inside the fiber

cavity, as comb filters with FSR comparable to the main cavity, via Vernier effect. Schröder et al. has used two sub-cavities to reduce the number of modes from 20000 to 200.

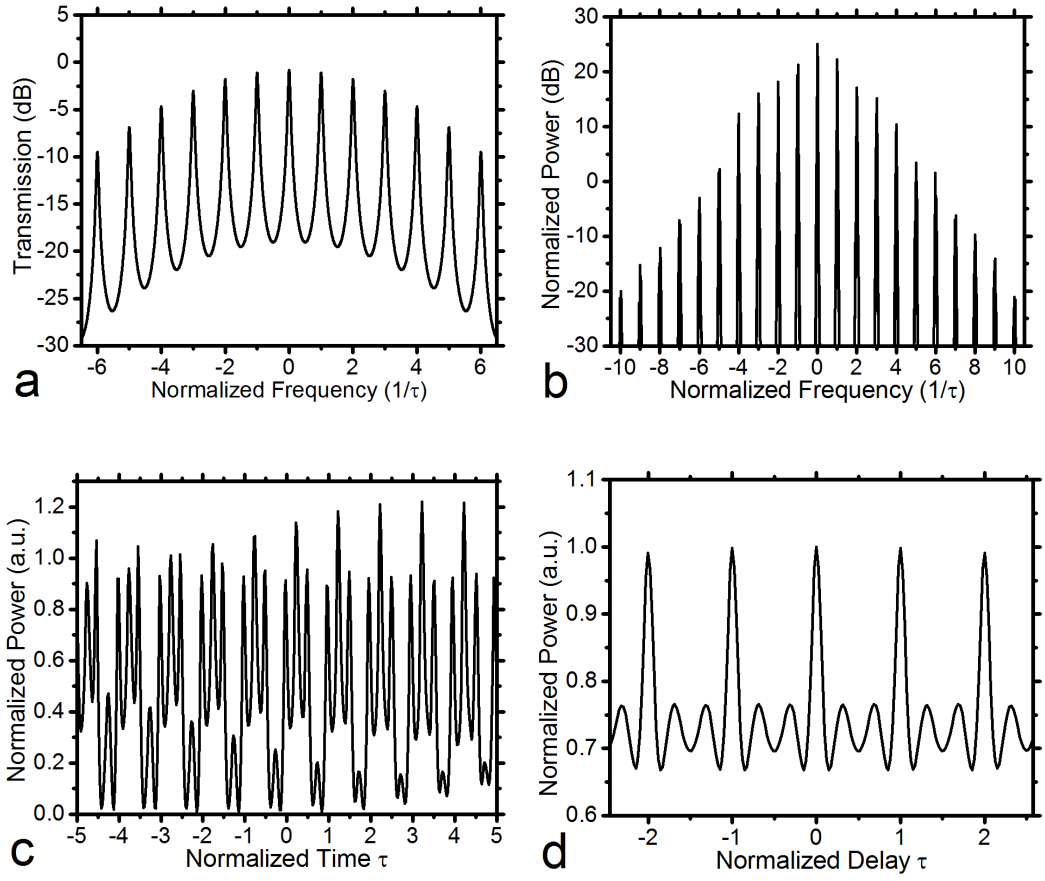

Figure 3.7 (a) Artificial function of broad bandpass filter and comb filter. (b) Simulated intracavity spectrum after 150 round trip. (c) Temporal profile of the optical intensity, (d) and corresponding autocorrelation.

We 的 in previous chapter (see Appendix B for a sample numerical code). For simplification, the broad bandpass filter (grating couplers) is merged to the comb filter function, as shown in Figure 3.7a. At high gain case (G = 2). Figure 3.7b shows

the stabilized intracavity spectrum after 150 round trip. Similar to [78], there exist several pulse trains in the time domain due to supermode noise, shown in Figure 3.7c. The corresponding autocorrelation is shown in Figure 3.7d. We can see that there are two subpulses in each period which is similar to the autocorrelation of multiwavelength laser in last chapter (Figure 2.23). It indicates those subpulses maybe came from the supermode noise.

3.2.2 Filter-driven dissipative four-wave mixing

To avoiding the instability due to the long cavity length, it is possible to combine the nonlinear medium and the comb filter to a single device which has been proposed and demonstrated by Peccianti at el. [81]. The configuration is shown in Figure 3.8.

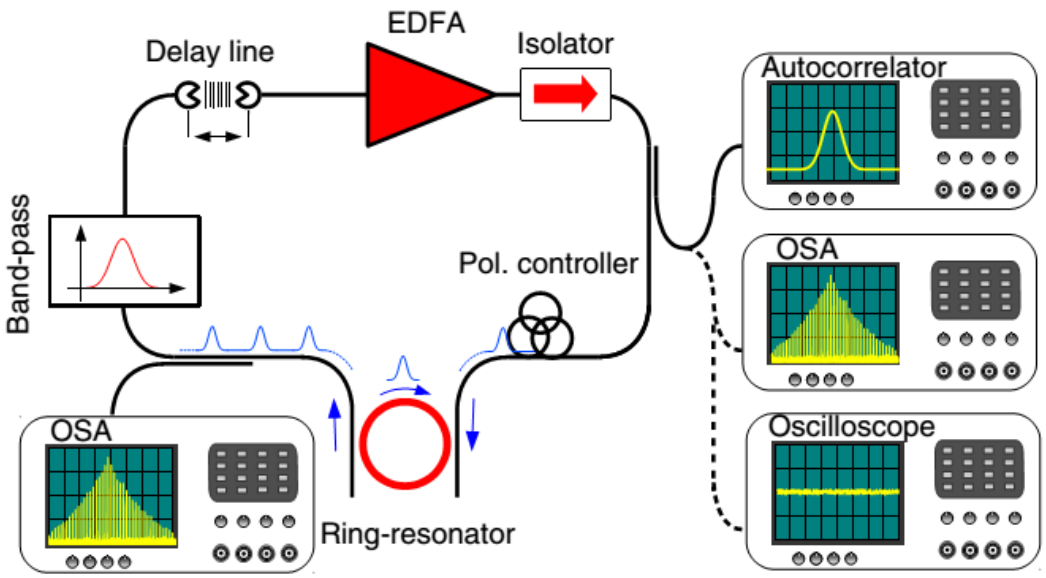

Figure 3.8 Experimental setup of FD-FWM using nonlinear silica MRR. Figures are adapted from [81].

They used a high-*Q* integrated silica MRR (with *Q* = 1.2 million) as the comb filter. By using the Kerr nonlinearity of the silica and the resonance enhancement of the MRR, a DFWM mode-locked laser has been achieved. The optical spectra and the

autocorrelation traces are shown in Figure 3.9. Because of the FWM is occurred inside the comb filter, they named this method as FD-FWM.

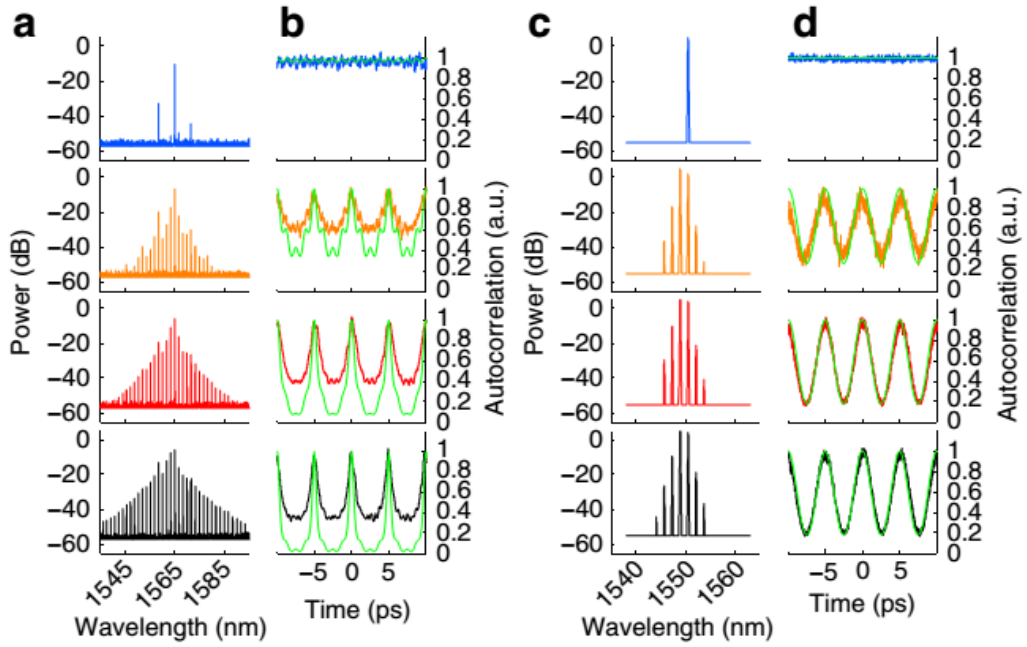

Figure 3.9 The optical power spectrum and autocorrelation: long cavity laser (a) and (b); short cavity laser (c) and (d). Figures are adapted from [81].

However, the supermode noise still occurs in the laser for long cavity, as shown in Figure 3.9a,b. In Figure 3.9b, the green curves are the ideal autocorrelation traces, by assuming the modes in the corresponding optical spectra in Figure 3.9a are all in phase, while other curves are the measurement results. As the filter Q = 1.2 million, therefore, the FWHM bandwidth of the filter is ~160 MHz which is comparable to the laser cavity mode spacing. It is possible to suppress the supermode noise and achieve single longitudinal lasing for each mode. By shortening the cavity length down to 3 m, a stable DF-FWM mode-locking operation is achieved by tuning the delay line in the laser cavity (for matching the cavity mode spacing to the filter).

Figure 3.9c,d show the idea autocorrelation traces which match well to the measured results.

DF-FWM with single longitudinal mode lasing has some advantages over the integrated OPO. For example, the line width is much narrower since it is the original cavity mode rather than the mode of the MRR. Also, the power induced or thermal drift of the resonant wavelengths will not directly affect the lasing wavelengths which mainly depend on the cavity modes. Therefore, the power and thermal instability of the wavelength is better.

3.3 Nonlinear microresonators

3.3.1 Modeling

In order to design a suitable MRR for FD-FWM, we have to first understand how it works. MRR is basically a closed-loop waveguide with one or two bus waveguides coupled aside, as shown in Figure 3.10. The closed-loop forms a cavity which define the resonant modes while the bus waveguides are used to couple the light in or out to the cavity.

In order to achieve a comb filter, two bus waveguides are chosen to form a 4-port MRR. Based the model from Yariv, MRR can be modeled analytically by separated into 4 parts: two directional coupler and two segments of waveguides between them [95]. The directional coupler has the transfer matrix:

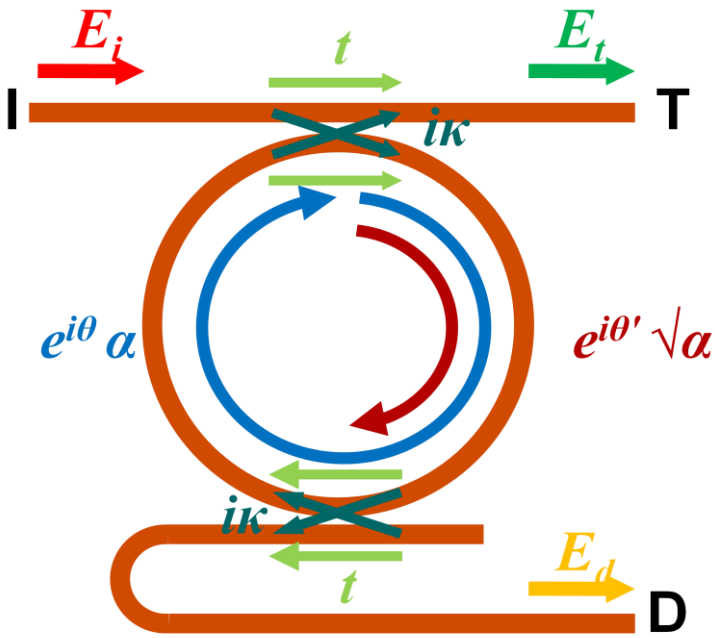

Figure 3.10 Schematic diagram of symmetric MRR (4-port) with input port (**I**), throughput port (**T**) and drop port (**D**).

$$\begin{pmatrix} E_3 \\ E_4 \end{pmatrix} = \begin{pmatrix} t & i\kappa \\ -i\kappa^* & t^* \end{pmatrix} \begin{pmatrix} E_1 \\ E_2 \end{pmatrix}, \tag{3.8}$$

where t, κ are the coupling coefficients of the input field E_1, E_2 and the output field E_3, E_4. Assuming the coupler is lossless, the transfer matrix is unity:

$$|t|^2 + |\kappa|^2 = 1. \tag{3.9}$$

Defining the total cavity round trip introduces the loss and the phase shift to the field:

$$E_{end} = \alpha E_{start} e^{i\theta}, \tag{3.10}$$

where α is the field round trip loss factor, θ is the round trip phase shift, E_{start} and E_{end} are the starting field and the end field of single round trip, repectively. The round trip phace shift $\theta = 2\pi L_{rt} n_{eff} / \lambda_o$ where L_{rt} is the physical roundtrip length, n_{eff} is the effective index of the waveguide mode and λ_0 is the wavelength in vacuum. If the MRR is symmetric, therefore, the two couplers are separated equally in the cavity and have same transfer matrix, $t = t_1 = t_2$ and $\kappa = \kappa_1 = \kappa_2$ (the '1' and '2' subscripts refer to the each coupler, respectively). We define the input field as E_i incident through input port I; the field passing through cavity and then coupled out from the input coupler as E_t to the throughput port T; the field coupled out from the output coupler as E_d to the drop port D. By assuming t , κ and α are indenpent of wavelength, the relationship of those field can be expressed as:

$$\frac{E_t}{E_i} = \frac{t(e^{-i\theta} - \alpha)}{e^{-i\theta} - \alpha t^2}, \quad \frac{E_d}{E_i} = \frac{i\sqrt{\alpha}\kappa^2 e^{i\theta'}}{1 - \alpha t^2 e^{i\theta'}}, \tag{3.11}$$

where $\theta' = \pi L_{rt} n_{eff} / \lambda_o$ is the phase shift reached to the output coupler with half of the round-trip.

If we consider the dispersion of the waveguides, waveguide mode effective index vary with wavelength $\partial n_{eff}/\partial \lambda_o = (n_{eff} - n_g)/ \lambda_o$, where n_g group index of the waveguide. Then FSR can be expressed by:

$$FSR = \frac{\lambda_m^{\ 2}}{n_g L_{rt}}. \tag{3.12}$$

3.3.2 Quality factor

The MRR has a very useful parameter, quality factor, Q which can be defined by FWHM bandwidth of its transmission spectrum:

$$Q = \frac{\lambda_m}{\delta\lambda_0}. \tag{3.13}$$

where λ_m is the wavelength at m-order resonance and $\delta\lambda_0$ is the FWHM of the resonant peaks (drop port) or dips (throughput port). It can be related to the fineness of F-P filter:

$$\textit{finesse} = \frac{FSR}{\delta\lambda_0} = \frac{\lambda_m^{\,2}}{\delta\lambda_0 n_g L_{rt}} = Q\frac{\lambda_m}{n_g L_{rt}}, \tag{3.14}$$

therefore, higher Q means higher finesse. Furthermore, Q also means how long does the photon stay inside the cavity [96]:

$$\begin{aligned} Q &= \omega_o \tau_{ph} \\ &= \omega_o \frac{T_{rt}}{\delta_c} \\ &= \omega_o \frac{1}{\delta_c}\frac{L_{rt} n_g}{c}, \\ &= \frac{2\pi}{\lambda_0}\frac{L_{rt} n_g}{\delta_c} \end{aligned} \tag{3.15}$$

where ω_o is optical angular frequency; τ_{ph} is the photon lifetime inside the cavity; T_{rt} is roundtrip time; δ_c is total cavity loss factor; c is the speed of light; λ_o is wavelength in vacuum. The our model, the cavity loss factor can be separated to intrinsic loss

factor δ_c and extrinsic loss factor δ_e which can be expressed by the cavity field loss factor α and coupler coefficient t:

$$\begin{aligned}\delta_c &= \delta_i + \delta_e \\ &= \ln\left(\frac{1}{\alpha^2}\right) + \ln\left(\frac{1}{|t|^2 \cdot |t|^2}\right) \\ &= 2\ln\left(\frac{1}{\alpha|t|^2}\right)\end{aligned}. \tag{3.16}$$

Therefore, Q becomes:

$$Q = -\frac{\pi L_{rt} n_g}{\lambda \ln(\alpha|t|^2)}, \tag{3.17}$$

Furthermore, since the MRR can trap the photon for lifetime, it can also consider the photon run inside the cavity for an effective length L_{eff}:

$$L_{eff} = \tau_{ph} \cdot \frac{c}{n_g} = Q\frac{\lambda}{2\pi n_g}. \tag{3.18}$$

This result shows that high-Q MRR would be able to replace a long waveguide for nonlinear process, e.g. FWM. In case of the MRR with Q = 1.2 million in [81], it provides an effective length of 19.7 cm.

3.4 Device design

In order to achieve 100 GHz repetition rate, the FSR of the microring should be matched to 100 GHz, therefore, ~0.8 nm wavelength spacing. By Eq. (3.12), the round trip length should be 750 μm. By using the same fabrication process of p-i-n

waveguide structure mentioned in previous chapter, the microring resonators with different coupling coefficient κ were fabricated. The optical image of typical device is shown in Figure 3.11a.

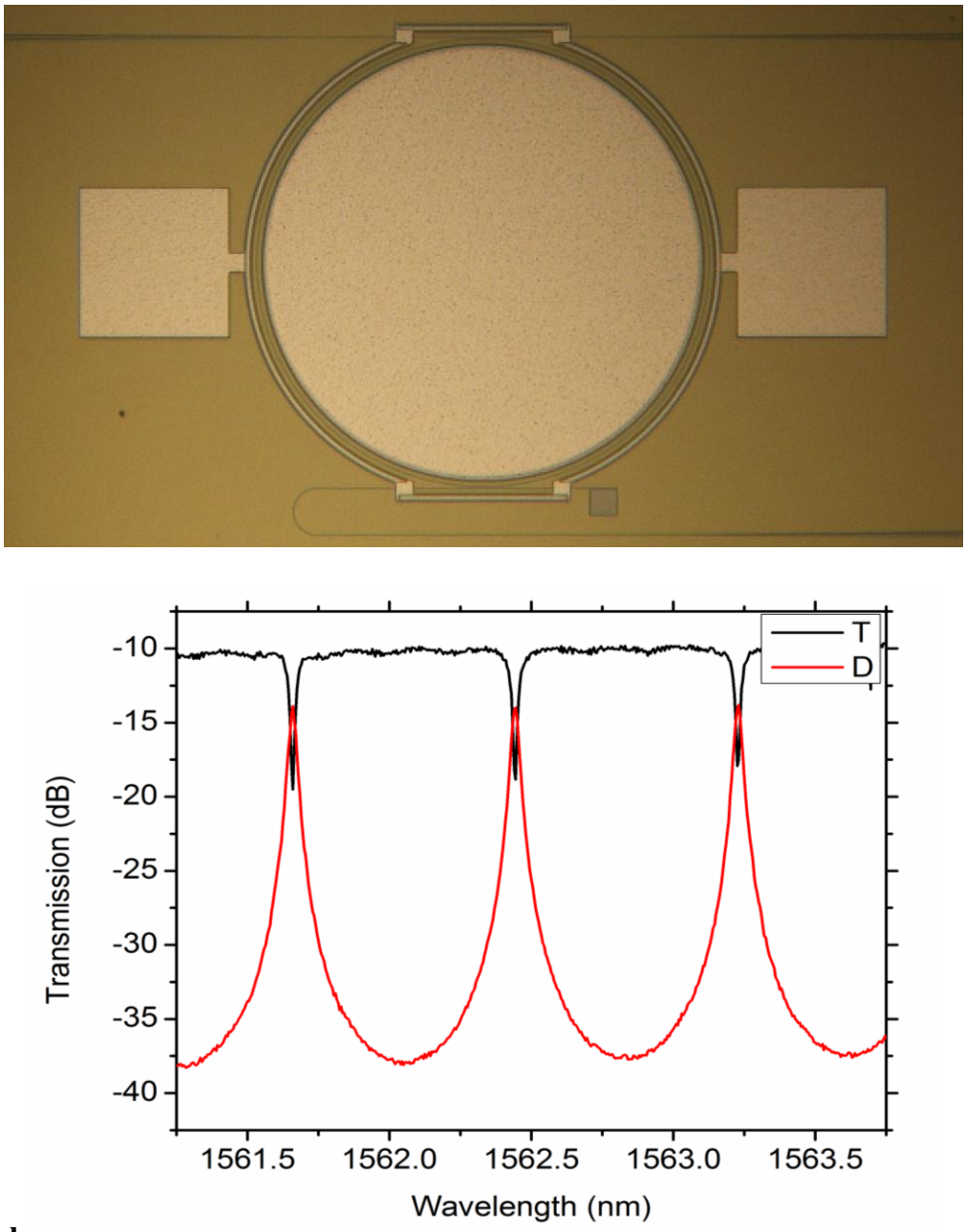

Figure 3.11 (a) Optical image and (b) Fiber-to-fiber transmission spectrum of SOI MRR (p-i-n diode) with 0.8 nm FSR.

For microring resonators, in order to have a better control of the coupling between the ring cavities and the bus waveguides, the race-track type geometry was used. They were fabricated with 6 μm coupling length and 120 μm bending radius, and thus with 766 μm round-trip length. The optical microscopic image of the fabricated MRR is shown in Figure 3.11a. Figure 3.11b shows the fiber-to-fiber transmission of the throughput port and drop port of the silicon MRR. We can see that drop port can work as a comb filter. It also indicates the typical FSR and *Q* are 0.78 nm and 52000, respectively.

3.5 Experimental setup

The cavity configuration is similar to the multiwavelength laser cavity in previous chapter. The only difference is the comb filter integrated into the silicon photonic chip, shown in Figure 3.12. An erbium-doped fiber amplifier (EDFA) provided the optical gain in the cavity. The isolator inside the EDFA fixed the laser in unidirectional operation as a ring cavity. The silicon MRR is inserted after the output 10/90 optical coupler (OC) and the polarization controller (PC) following the EDFA

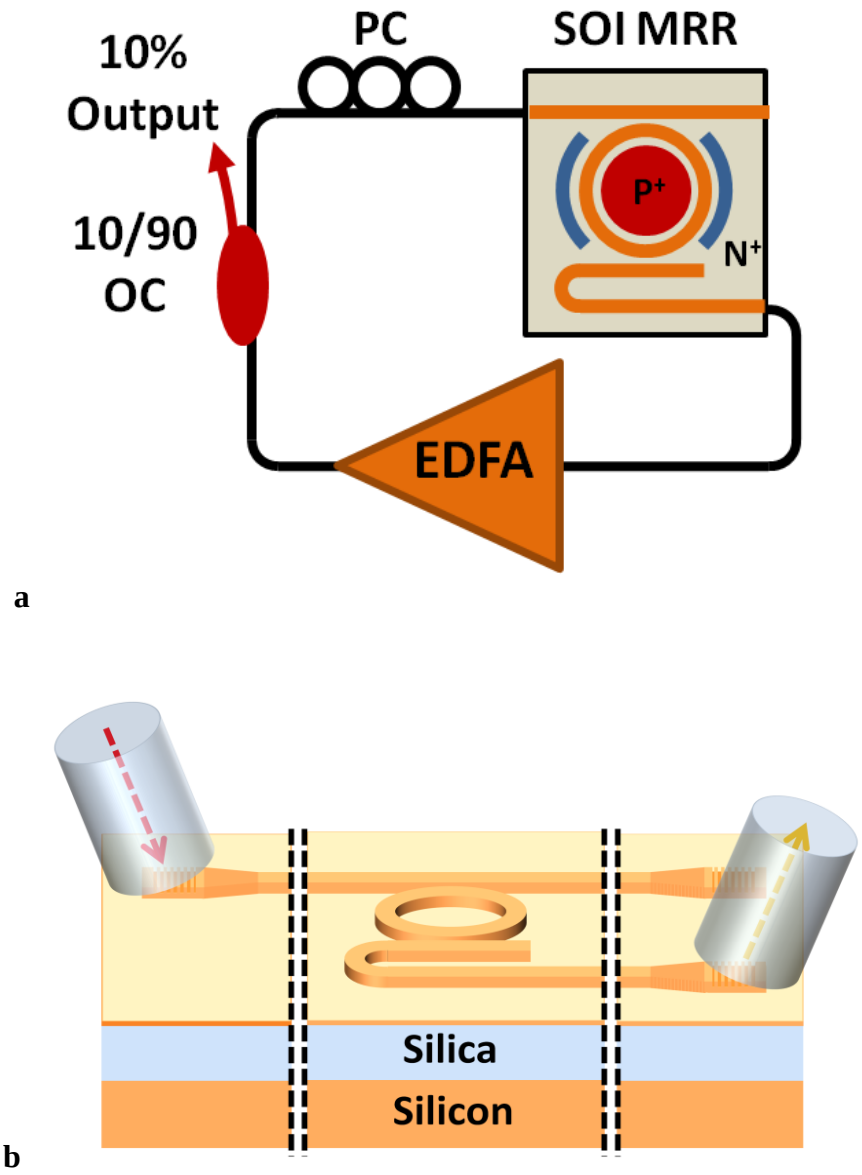

Figure 3.12 Schematic diagram of (a) experimental setup, and (b) coupling between SMF and silicon waveguide through grating couplers.

in order to ensure reasonable optical power in the silicon for triggering FWM. The coupling between silicon waveguide and the single mode fiber was via a grating coupler, shown in Fig. 1b. The coupling efficiency of the grating coupler is polarization dependent and was optimized by adjusting the PC [76].

3.6 Results & discussions

3.6.1 Fundamental FD-FWM mode-locking

When the output power of the EDFA was set to 27 dBm, the laser was mode-locked. The TPA in the silicon waveguide produced a photocurrent of 0.87 mA at 6 V reverse bias applied across the diode of the silicon MRR. The optical spectrum is

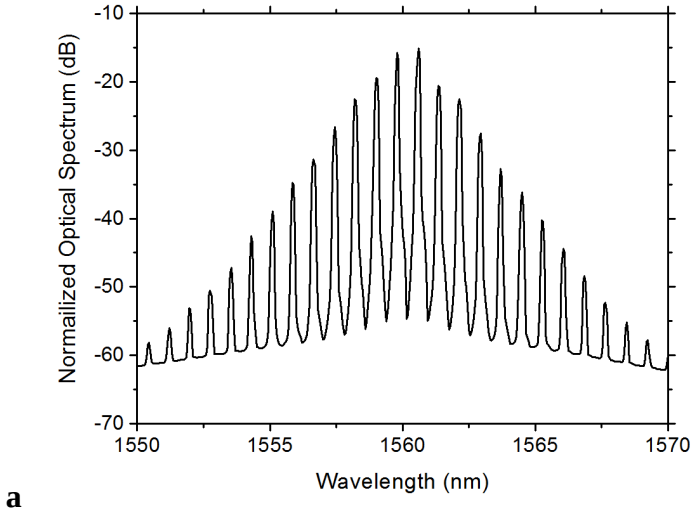

a

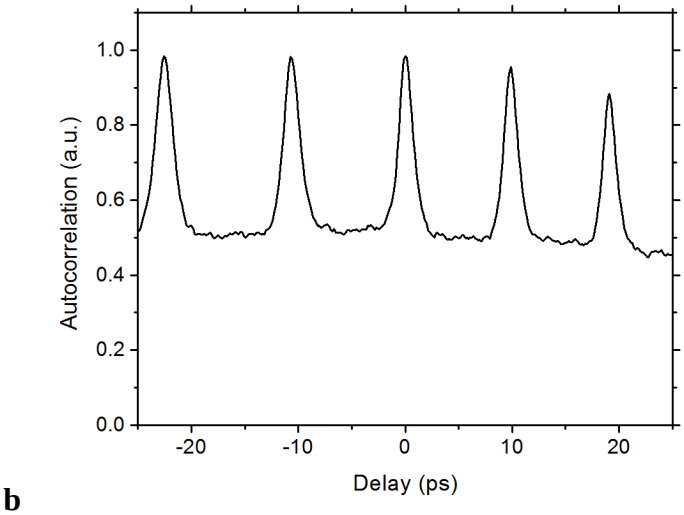

b

Figure 3.13 (a) Normalized optical spectrum and (b) autocorrelation trace of the mode-locked laser.

shown in Figure 3.13a. The central wavelength is 1544.4 nm with 0.78 nm mode spacing (96.1 GHz). The measured line width shown in the figure is limited by the resolution of the optical spectrum analyzer.

The autocorrelation trace of the laser output is shown in Figure 3.13b. The repetition rate is about 100 GHz. The non-zero background is similar to the results of 33 m cavity length with silica MRR in [81]. The full-width-half-maximum (FWHM) of the pulse is about 4 ps, therefore, the duty cycle is 0.4. The peak-to-background ratio is 2.1:1. The mode-locking state can be maintained for longer than an hour in room temperature and without any active vibration isolation.

3.6.2 Harmonic FD-FWM mode-locking

As the phases of the lasing mode are locked by FWM, if the filter spectral profile provides slightly uneven gain among ring resonant modes, it is possible to induce uneven energy transfer via FWM. We can simulate this situation by adding perturbation to the comb filter function in the model in Section 3.2.1 (see Appendix B). We first suppress the odd harmonics of the comb filter, as shown in Figure 3.14a. The intracavity spectrum after 150 round trips is shown in Figure 3.14c. We can observe that the odd harmonics are suppressed over 80 dB. Figure 3.14e shows the corresponding autocorrelation. The repetition rate is doubled. We can call it second harmonic DFWM mode-locking. If suppress the other harmonics except the third harmonic and it multiples, as shown in Figure 3.14b, the intracavity spectrum will be dominated by those unsuppressed harmonics, as shown in Figure 3.14d. The repetition rate is triple in the autocorrelation, as shown in Figure 3.14f. Again, we call it third harmonic DFWM mode-locking.

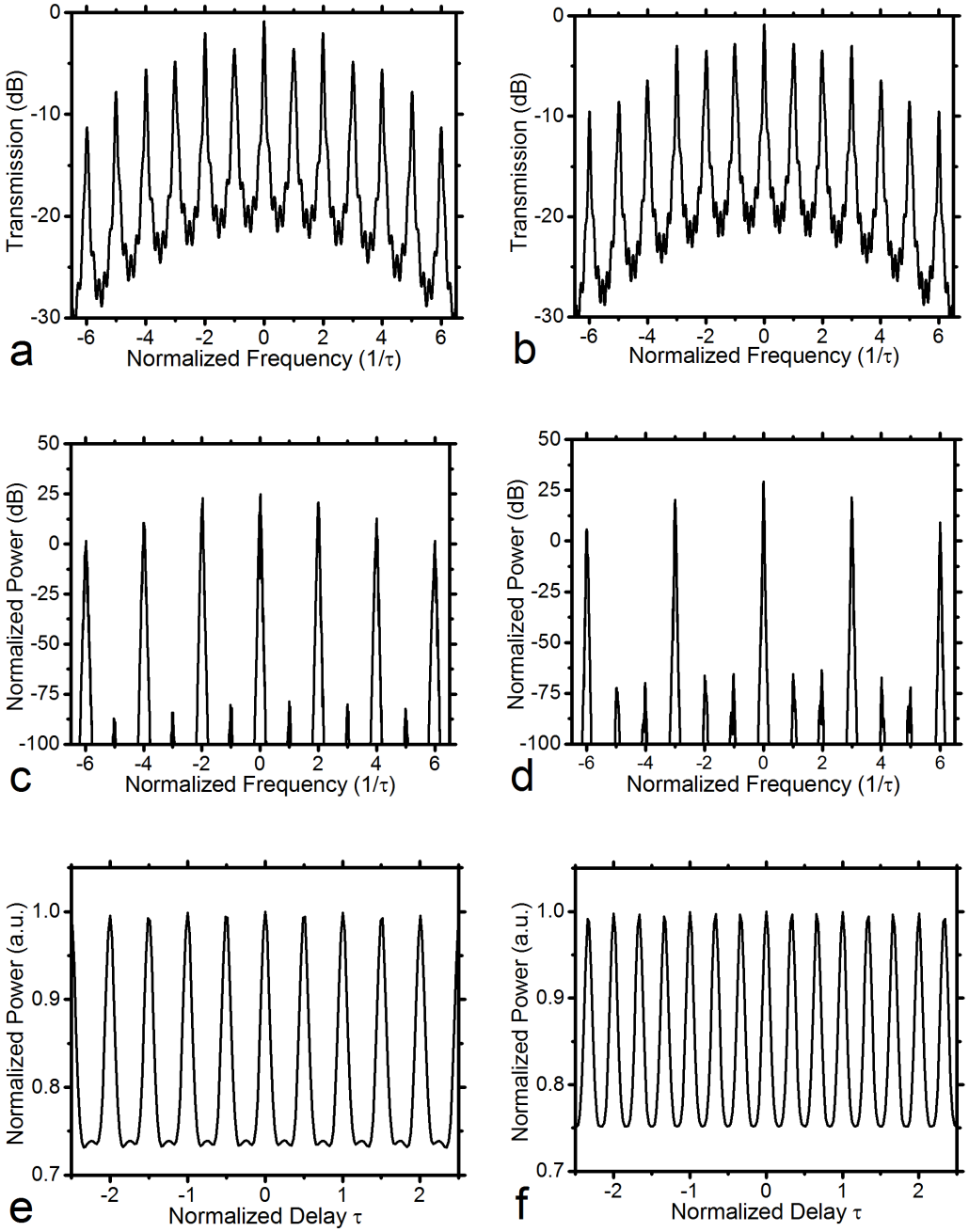

Figure 3.14 The perturbated comb filter functions, simulated intracavity spectra after 150 round trip, and autocorrelations: (a,c,e) second harmonic mode-locking; and (b,d,f) third harmonic mode-locking.

Peccianti et al. have demonstrated harmonic mode-locking in FD-FWM with the same silica MRR in [97], [98]. By tuning the bandpass filter (FWHM of 8 nm) and cooperating with the slightly uneven transmission loss among the MRR resonant modes, the laser exhibits phase-locking the lasing modes separated by 803.2 GHz. The optical spectrum and the autocorrelation trace of the laser output are shown in Figure 3.15. The autocorrelation shows a quasi-sinusoidal output in 803.2 GHz.

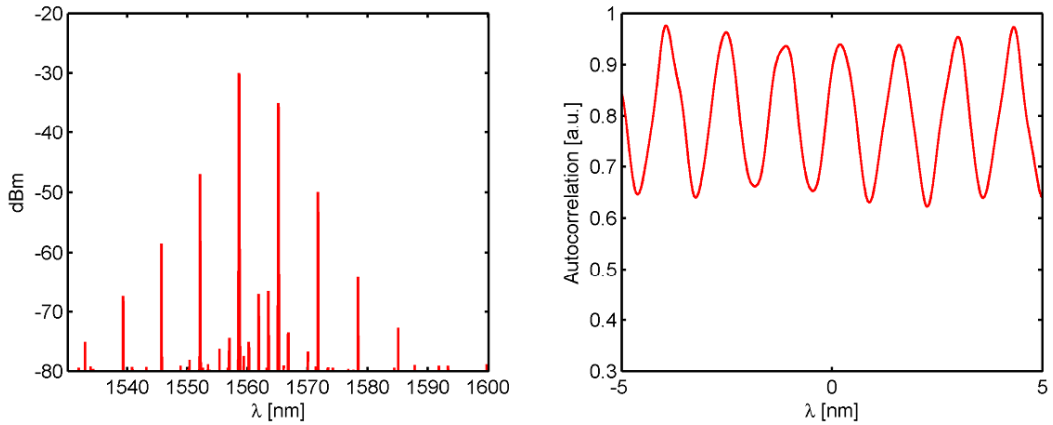

Figure 3.15 Spectrum (left) and autocorrelation (right) of the laser output in the 803.2GHz quasi-sinusoidal operating regime, adapted from [97], [98].

In principle, our silicon MRR FD-FWM configuration is in similar situation as the silica one. The grating couplers are basically a pair of broadband tunable bandpass filters. If we slightly detune the fiber position as we mention in Chapter 2, the transmission spectrum of the drop port will slightly shifted, as shown in Figure 3.16. As the same as the silica case, the silicon MRR would have slightly different insertion loss among the resonant modes which is due to the wavelength dependent coupling efficiency of bus waveguide coupling and the wavelength dependent propagation loss of the waveguide. If we tune the fiber to certain position, the laser

started to mode-lock the modes with 288.3 GHz, as the optical spectrum shown in Figure 3.17a. We can see that the phase-locked modes have higher power level among the others. It means they extract most of the energy of the laser and transfer it to the phase-matched modes. Figure 3.17b shows the autocorrelation trace. There is also a quasi-sinusoidal output in about 300 GHz. We named it as "harmonic FD-FWM".

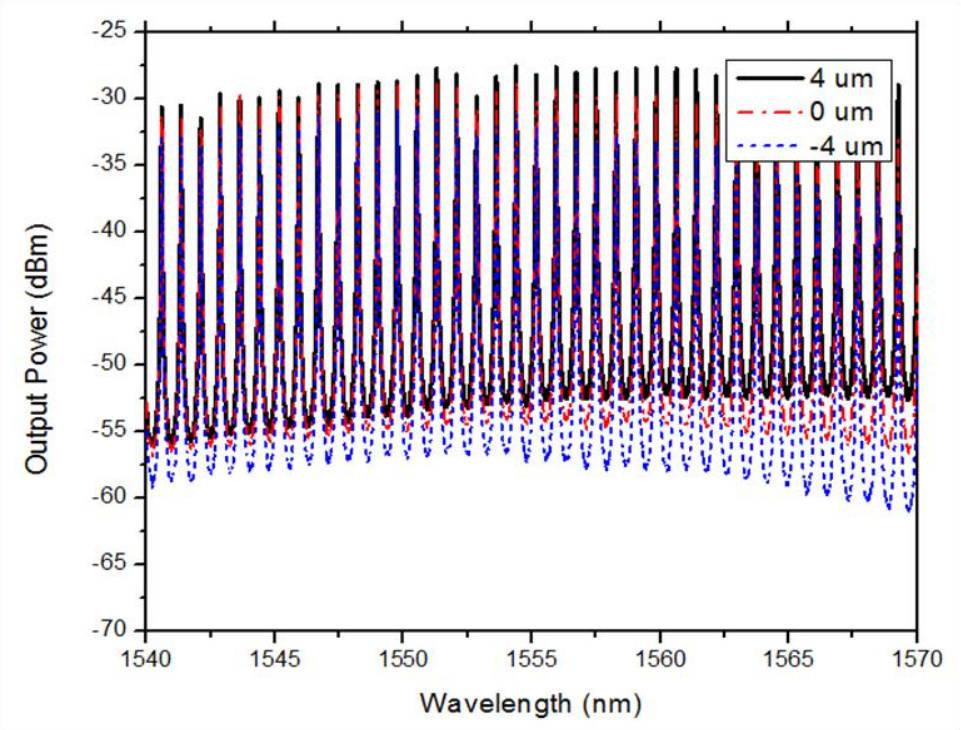

Figure 3.16 Fiber-to-fiber transmission spectra of SOI MRR with different fiber positions.

If we further adjust the fiber position, the laser is able to mode-lock the modes with 384.4 GHz, as the optical spectrum shown in Figure 3.17c. However, the major tones have about 4 dB power different which may be due to the larger gain different among them (asymmetric transmission spectrum of the grating). Also, we can see

that the lines between two major modes are not suppressed well as 300 GHz one. Also, the harmonics of these two modes are at the similar power level to the others. It may they have not efficiently transfer the energy to their harmonic tones which may be due to their uneven power level and the less efficient FWM for larger wavelength spacing. Figure 3.17d shows the autocorrelation trace. Since the major tones have about 4 dB power different and unsuppressed (unwanted) modes between them,

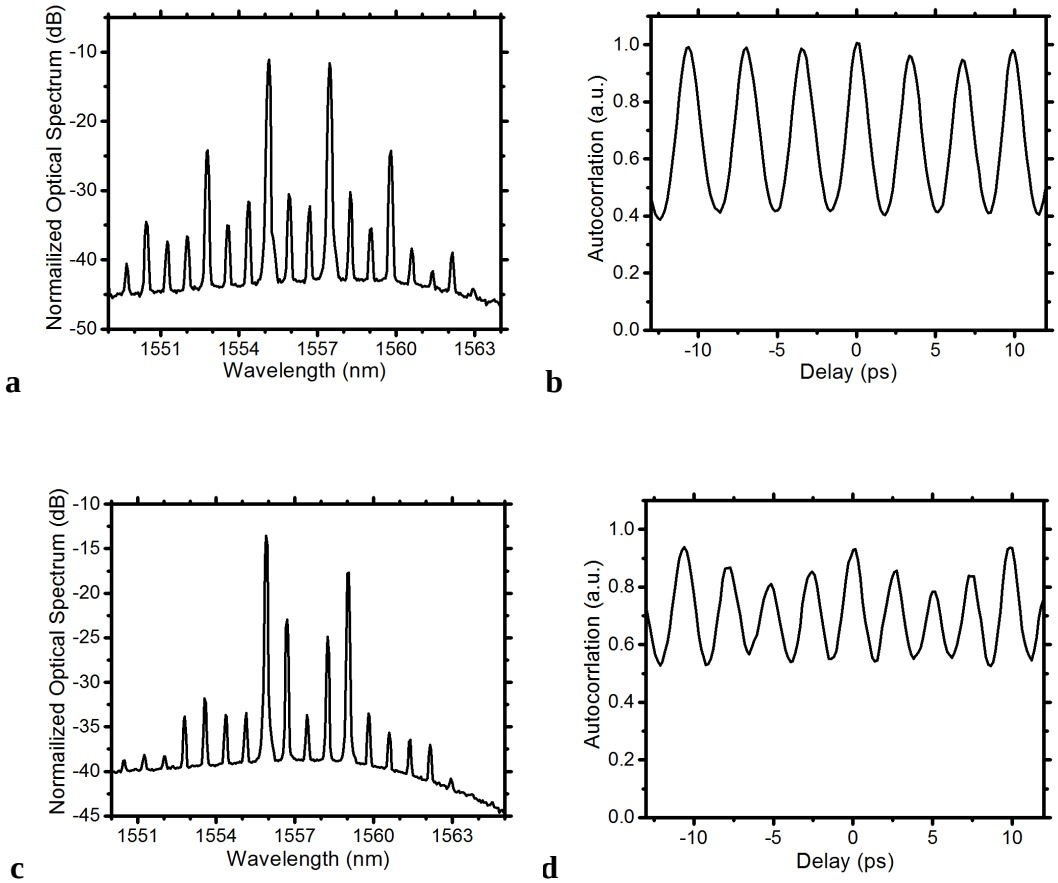

Figure 3.17 Normalized optical spectra and autocorrelation traces of the mode-locked laser: (a,b) 3rd harmonic (288.3 GHz); (c,d) 4th harmonic (384.4 GHz).

the quasi-sinusoidal output in about 400 GHz has shallower modulation depth and varying envelope.

In fact, this kind of harmonic FD-FWM can be control by cascading another MRR with different FSR in the same chip via Vernier effect. Their lasing wavelength and their frequency spacing can be tuned by adding the integrated thermal heater on top of the silicon MRR and using thermal-optic effect [56]. Also, as we mention before, it is possible to further integrate the optical components to the chip for simplifying the laser system. The power requirement of the EDFA may be reduced considerably by using apodizing grating couplers and low loss waveguides [76]. Furthermore, if we want to achieve single longitudinal mode lasing as the silica MRR, it may be possible to use the MRR based on etchless silicon waveguides which avoids the scattering loss due to the sidewall roughness during the dry etching process. Etchless silicon MRR with intrinsic Q of 760,000 has been reported recently [99].

3.7 Conclusions

In conclusion, we proposed and demonstrated a FD-FWM mode-locked fiber laser based on nonlinear silicon MRR. It shows that the silicon MRR has sufficient nonlinearity and quality factor (Q ~50000) for successful operation of the FD-FWM scheme. The mode-locked laser was stable for over an hour at room temperature without any active feedback stabilization. The laser provides a potentially compact and low-cost high repetition rate pulse train source for possible applications in high speed communication and on-chip optical clock.

4 Graphene on silicon waveguides and ultrafast passive mode-locked lasers

4.1 Introduction

Ultrafast laser with short pulse width and high peak power have a number of potential applications, such as basic scientific research, medicine, and materials processing. Also, such kind of pulse source also plays a role as the seed of supercontinuum generation which is widely used in spectroscopy. On-chip high peak power pulse source provides an attractive solution for compact and low cost sensing and spectroscopy systems.

In last chapter, the passive FD-FWM mode-locked laser provides an ultrahigh repetition rate pulse source. However, the peak power of each pulse is only at the similar order of the laser average power. It is due to the small number of modes which is hard to form a short time duration pulse. Also, the high repetition rates limits the energy per pulse, therefore, the peak power approaches to the average power of the gain medium. To achieve high peak power laser pulses, the most common approach is passive mode-locked lasers using saturable absorbers. This kind of saturable absorbers is currently dominated by semiconductor saturable absorber mirrors (SESAMs) in the market. In silicon photonic platform, there is a similar option to grow or deposit a layer of III-V semiconductors on top of the silicon core layer as an integrated saturable absorber. However, these materials have very narrow working wavelengths, tens of nanometers, and involve a number of complex and

non-complementary metal–oxide–semiconductor (CMOS) compatible processes which increase the fabrication cost.

A potential alternative solution is using single-walled carbon nanotubes (SWNTs) which provide a low cost and a wide range of working wavelengths. Passive mode-locked fiber lasers using SWNTs has been demonstrated [100], [101], [102], [103], [104]. The bandgap energy of SWNTs is controlled by their diameters and chiralities [100], [101]. In order to have a broadband saturable absorber, the composite of SWNTs with a range of diameter and chirality distribution has to be used [102]. However, in practice, only part of the SWNTs matching the right bandgap energy works as the saturable absorber while the others only provide pure insertion loss. It largely limits the performance of devices. Fortunately, graphene, as an unrolled SWNT, provides an alternative solution as a broadband saturable absorber. Because of the unique linear dispersion around the Fermi level, there is always a pair of electron-hole matching the resonant condition for a range of photon energies. Also, the ultrafast massless-like carrier dynamics and the strong light absorption of 2.3% in a monolayer of 0.7 nm thickness provided that graphene can act as a fast saturable absorber. Having those advantages, graphene based broadband passive mode-locked fiber lasers have attracted considerable interest recently [105], [106], [107], [108].

On the other hand, following the success of graphene based electronic devices [109], [110], graphene also provides an attractive optoelectronic integrated platform for high speed optical communication and on-chip interconnect [111], [112], [113], [114], [115]. By using the ultrafast carrier dynamics, high speed integrated graphene on silicon optoelectronic devices such as electroabsorption modulators and photodetectors have been reported [111], [112], [113]. Some of those devices relied

on the advantaged of graphene-silicon waveguide hybrid structure which offers the advantage of the in-plane propagation. It greatly increases the interaction length compared to the geometry with light incident normal to the graphene plane. Large optical modulation depth and large optical nonlinearities have been reported for graphene in the in-plane geometry recently [114]. However, the saturable absorption and passive mode-locking using the in-plane saturable absorption of graphene on silicon waveguides has not been investigated yet.

In this chapter, we study saturable absorption in graphene on silicon waveguide. We observed a large saturable absorption in this kind of devices, as high as 50% change in transmission. Furthermore, we propose and demonstrate a mode-locking of an erbium fiber laser using a graphene on silicon waveguide. By using the saturable absorption of graphene in the evanescent field of the waveguide mode, a stable mode-locked fiber laser is achieved. The structure is compatible with silicon optical waveguides and may be easily integrated with other passive waveguide devices such as tunable filters or silicon modulators for making tunable mode-locked lasers.

4.2 Graphene photonics

4.2.1 Electronic structure

The unique physical properties of graphene are come from the electronic band structure. For a sheet of ideal graphene, the carbon atoms are in a planar hexagonal lattice, honeycomb lattice, as shown in Figure 4.1 [116]. The distance between the two nearest neighbor atoms (labeled A and B) is 1.42 Å. The primitive unit cell is drawn in dashed lines and the primitive lattice vectors are $\vec{t}_1$ & $\vec{t}_2$ with length *a* of 2.46 Å. The reciprocal lattice is also a hexagonal lattice with different orientations by

simply rotating the real space by π/2, as shown in Figure 4.1. The corresponding primitive reciprocal lattice vectors of the Brillouin zone are $\vec{K}_1$ & $\vec{K}_2$ with length of $2/\sqrt{3}\,a$.

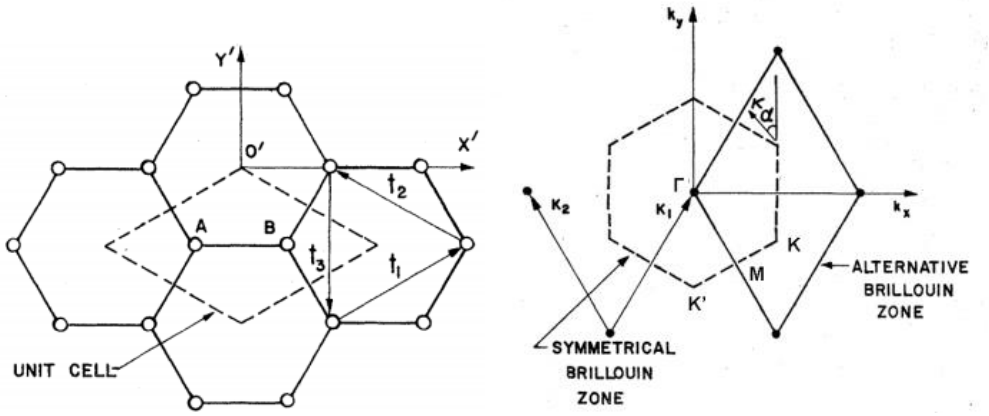

Figure 4.1 Real (left) and reciprocal (right) space lattices of graphene adapted from [116].

In real space, each atom is covalently bound with three nearest neighbor atoms by three sp^2 σ-bonds, and forms an σ-band with the sp^2 electrons of all other carbon atoms. The fourth valence electron is in p_z state which is oriented normal to the graphene sheet. It will form π-bonds with all other p_z electron in order to form a π-band. A single C-C σ-bond is typically stronger than a single π-bond, hence the σ-band, has lower energy compared with π-band, therefore, it should be occupied first. By the results from simple tight binding (TB) model, the bonding π-band is always energetically below the antibonding π^*-band for all wave vectors except at the corner points of the Brillouin zone boundary *K*-points, as shown in Figure 4.2 [117], [118].

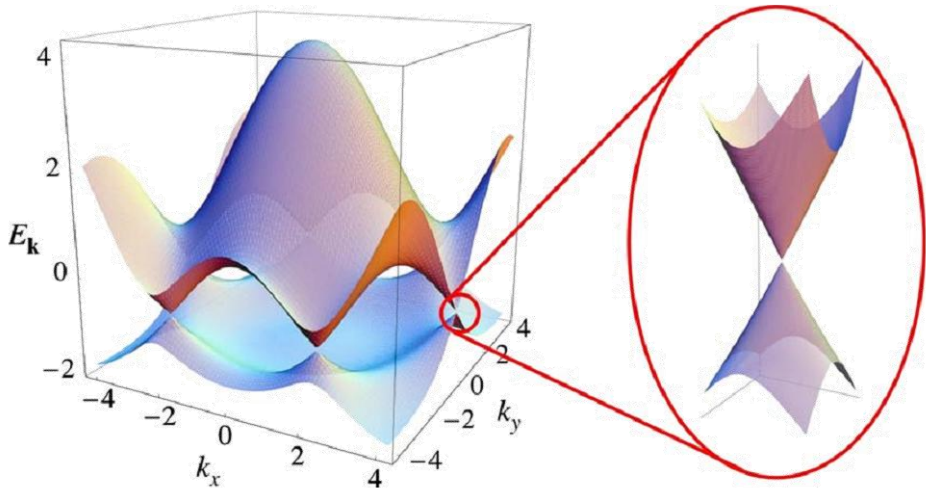

Figure 4.2 Dispersion relations of the π-(lower half) and π^*-(upper half) bands in graphene using TB approximation. The energy unit is the nearest-neighbor C-C overlap integral $\gamma_0 \cong 3.0$ eV and the scale is measured from the Fermi level ε_F. The figure is adapted from [118].

The Fermi level, ε_F, is crossing the *K*-points. The six *K*-points of the central Brillouin zone are given by

$$\vec{k}_F = \pm(\vec{K}_1 - \vec{K}_2)/3; \pm(2\vec{K}_1 - \vec{K}_2)/3; \pm(\vec{K}_1 - 2\vec{K}_2)/3. \qquad (4.1)$$

However, only two of these points are inequivalent due to the periodic boundary condition and translational symmetry, they are labeled ***K*** and ***K'***. They form four spin degenerate states ε_F. Furthermore, the density of states (DOS) is zero at ε_F. Graphene cannot be characterized as metal or semiconductor, but so-called zero-DOS metal or zero-gap semiconductor. Moreover, it is very interesting that the Taylor expansion of

the dispersion relations of graphene $\varepsilon_{\pm}(\vec{k})$ at *K*-points in terms of $\vec{\kappa} = \vec{k} - \vec{k}_F$, small displacement from *K*-points, is valid in first-order term. In first-order approximation:

$$\varepsilon_{\pm}(\vec{k}) = \varepsilon_F \pm \hbar v_F \left| \vec{k} - \vec{k}_F \right|, \tag{4.2}$$

where v_F is the Fermi velocity and $\hbar$ is the reduced Planck constant. It means the dispersion relation near the Fermi level is approximately linear. Therefore, the effective mass of the electron at this state is zero [119]. The v_F is 1.1×10^8 cm/s. The dynamic of electrons and holes can be described by the Hamiltonian at *K*-points, shifted the energy origin to ε_F:

$$H^K = v_F \vec{\sigma} \bullet \vec{\kappa}, \tag{4.3}$$

where $\vec{\sigma} = \left(\vec{\sigma}_x, \vec{\sigma}_y, \vec{\sigma}_z\right)$ are the Pauli matrices. The positive (negative) energy solutions are corresponding to the particles (antiparticles) as the electrons (holes) in the conduction (valence) band. Eq. (4.3) is exactly the same as the Dirac equation for 2D massless spin-1/2 Fermions. Therefore, the carriers in graphene always travel at the same velocity v_F is in 1.1×10^8 cm/s. This ultra-relativistic carries dynamics of graphene exhibits a number of interesting electronic transport behaviors such as anomalous quantum hall effect [120], [121], ultrahigh room temperature mobility (μ > 200,000 cm^2/Vs, limited by the scattering of acoustic phonons) [122], [123], and Klein tunneling [124], [125].

4.2.2 Universal absorbance

For optical properties, graphene has been predicted to have a frequency independent optical absorption, from infrared to visible range. The value is fixed at $\pi\alpha$ = 2.293%, with

$$\alpha = \frac{e^2}{\hbar c}, \tag{4.4}$$

where α is the fine structure constant, e is the elementary charge, and c is the speed of light in vacuum (in cgs units). The reason of this universal absorbance is related to the frequency independent optical conductivity of graphene:

$$\sigma = \frac{\pi}{4} G_0, \tag{4.5}$$

where $G_0 = 2e^2/h$ is the quantum conductance which is the intrinsic property of 2D massless Fermions. This property has been confirmed experimentally by several groups in 2008 [126], [127], [128]. Figure 4.3 shows the absorbance of normal incident over the range of photon energies between 0.5 and 1.2 eV in [128]. The value of measured absorbance belongs to $\pi\alpha$ within 10% for 3 different samples.

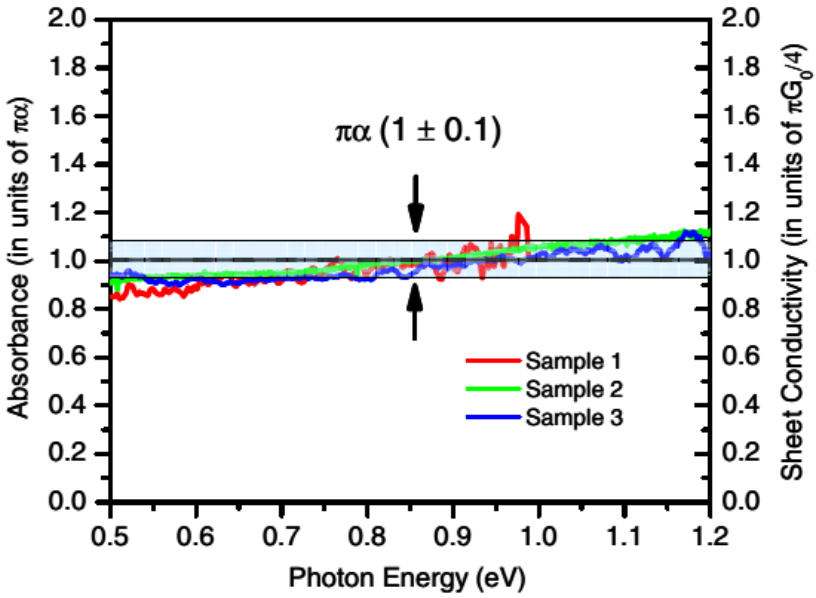

Figure 4.3 Absorption spectra of three different samples of graphene, adapted from [128].

4.2.3 Saturable absorption

Another interesting optical property is saturable absorption. The processes is illustrated in Figure 4.4 [105]. When interband photo-excitation occur, electron-hole pairs are generated which induce a nonequilibrium carrier thermal distribution, shown in Figure 4.4a. These hot (energetic) electrons and holes will cool down and excited other carries to form a hot Fermi-Dirac distribution after ~100 fs, with electronic temperature T_e [129], [130], shown in Figure 4.4b. These excited carries may block some of the optical excitation in the range of photon energies in range of $k_B T_e$ by Pauli exclusion principle, where k_B is the Boltzmann constant. The electron and holes will be further cool down and recombined until recover to the origin distribution with ~1 ps [131], [132]. The decrease of absorption is not significant and still can be regarded as linear absorption. However, if the optical intensity is too

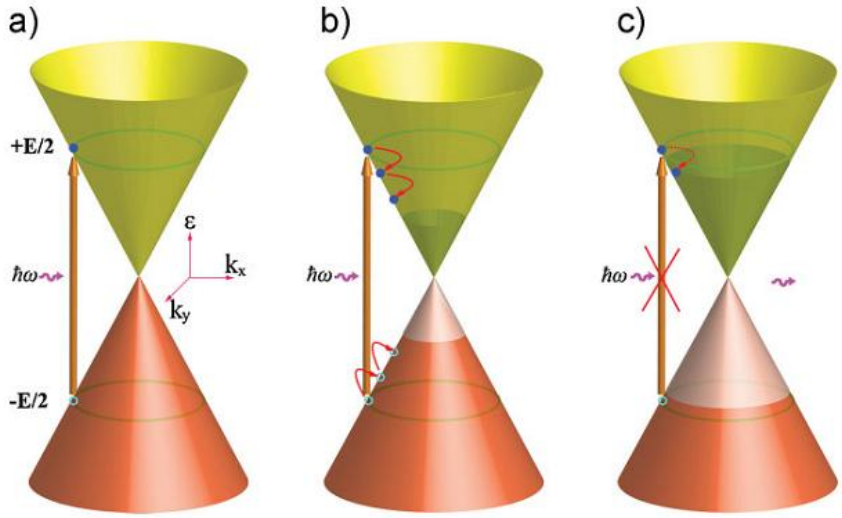

Figure 4.4 Schematic diagram of light absorption of light in graphene: (a) at low light intensity, interband photo-excitation generates electron-hole pairs which induce a nonequilibrium carrier thermal distribution; (b) excited carries may block some of the optical excitation in the range of photon energies in range of $k_B T_e$; at high light intensity, the photogenerated carries fill up the conduction and valence band and no more absorption. Figures are adapted from [105].

high enough, the photogenerated carries fill up the conduction and valence band and no more absorption is allowed which makes the graphene becomes transparent to the other photons, the absorbance start to decrease [133], as shown in Figure 4.4c.

Figure 4.5 shows the saturable absorption of a graphene-polymer composite (~50 μm thick) sandwiching between two fiber connectors in [107]. The saturable absorption occurs at the wavelength between 1548 nm and 1568 nm, with ~1.3% change in transmission.

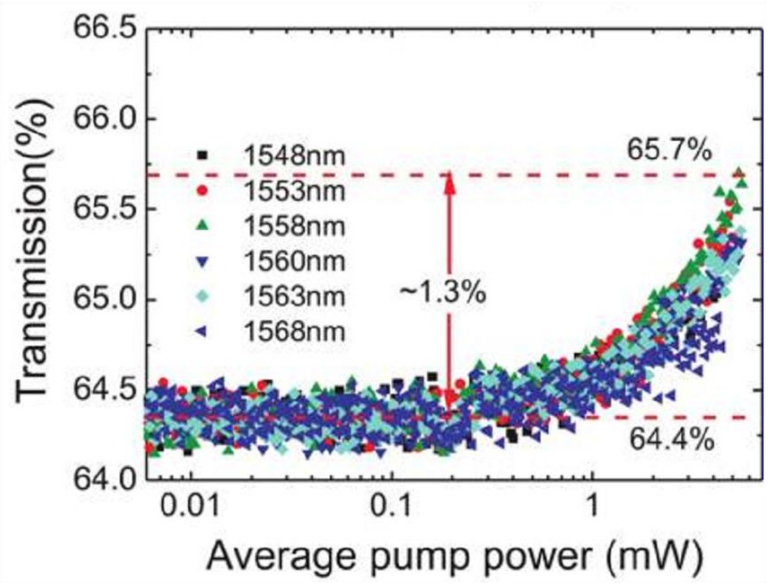

Figure 4.5 Transmission of the graphene composite of different average pump powers for six excitation wavelengths, adapted from [107].

4.3 Graphene on silicon waveguide

Since graphene has a number of optical properties which are related to its electronics structure, it is straight forward to modify the optical response by electric control. It has been demonstrated that by tuning the Fermi level of graphene by field effect, the absorption spectrum can be changed [127]. It is due to the carrier distribution follows the change of Fermi level. If the Fermi level is decreased by $0.5\hbar\omega$ from the Dirac point (*K*-point), there will be no electron from the valance band can be excited by photon with energy $\leq \hbar\omega$ (or the holes in valance band are filled to block the excitation of holes in conduction band). In other extreme, if the Fermi level is increased by $0.5\hbar\omega$ from the Dirac point, the electrons are filled in conduction band which blocks the excitation of electrons in valance band (or no hole from the conduction band can be excited by photon with energy $\leq \hbar\omega$).

However, the absorption change in 2.3% in normal incident is not enough for the practical applications, e.g. optical modulators. In order to increase the absorption, in-plain propagation has been proposed. The graphene on silicon waveguide structure offers the advantage of greatly increasing the interaction length compared to the geometry with light incident normal to the graphene plane. In 2011, a broadband electroabsorption modulator based on a graphene on silicon waveguide structured demonstrated for working frequency up to 1.2 GHz [112]. By using the advantage of in-plain absorption, it only needs a length of 40 μm graphene on silicon waveguide to achieve 3 dB modulation depth in 1.2 GHz. By using similar approach, ultra low power FWM has been demonstrated in graphene on silicon photonic crystal cavity.

In order to take advantage of in-plain propagation in for integrated saturable absorber, we employed the graphene on silicon waveguide structure. In order to avoid TPA and induced FCA, which can be regarded as reverse saturable absorption since the absorption increases with intensity [134], the waveguide should be as short as possible. Therefore, we have to employ focusing subwavelength grating couplers. To ensure better process control in the definition of the waveguide grating coupler by using a deep etch through the top silicon rather than a shallow etch (in which the etch depth is dependent on etch rate), we employed silicon suspended membrane waveguide (SMW) structure [135]. The structure of the graphene on silicon SMW is schematically shown in Figure 4.6.

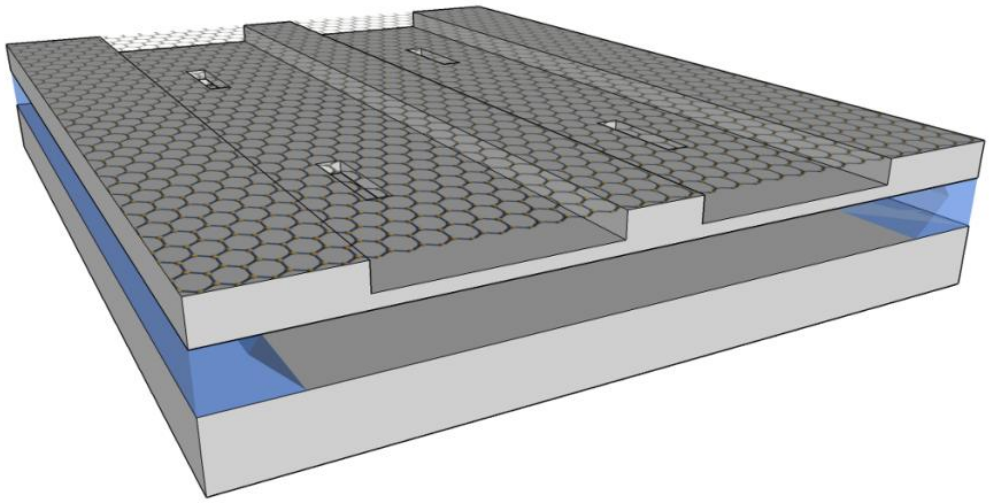

Figure 4.6 Schematic diagram of graphene on silicon waveguide

The silicon waveguide was fabricated on an SOI wafer with 340 nm top silicon layer and 2 μm buried oxide (BOX). The waveguide width and etching depth is 500 nm and 500 nm, respectively, in order to satisfy the single mode condition of quasi-transverse electric (TE) mode at wavelength of 1560 nm. In order to remove the BOX layer under the waveguide, rectangular holes were etched beside the waveguide periodically.

4.4 Sample fabrication

The fabrication processes employed the electron beam lithography (EBL). The SOI wafer was spin coated a layer of positive resist (ZEP520A). The waveguides were patterned by EBL system (Elionix ELS7800 80kV). After the development, the waveguides were defined by inductively coupled plasma / reactive ion etching (ICP/RIE) (Oxford Plasma Lab 100 Dual Chamber ICP Dry Etcher) with C_4F_8 and SF_6 mixture. By repeating the above steps with different etching depth (etching

through to the BOX), the grating couplers and the periodical holes besides the waveguides were defined. The final step was removing the BOX in the stirred 5:1 water: hydrofluoric acid (HF) (48%–51% concentration) solution. It is noted that a ~30 nm protective layer of silicon nitride was deposited on top silicon layer before the fabrication processes using plasma-enhanced chemical vapor deposition (PECVD) (Oxford Plasma Lab 80+ PECVD System) in order to prevent any top surface damage during fabrication process. This layer would be removed by HF solution in the final step.

The focusing subwavelength grating couplers was designed for coupling between the quasi-transverse electric (TE) mode of the silicon waveguide and conventional single mode fiber (SMF). It was measured with a coupling efficiency of ~50% and ~30% at 1530 nm and 1560 nm, respectively. The straight silicon waveguide length was 175 μm and the input and output focusing grating couplers were each 30 μm in length [136].

For the graphene, the large area monolayer graphene was synthesized on a copper foil by chemical vapor deposition (CVD). It had to be transferred on top of the membrane waveguide. A thin poly(methyl methacrylate) (PMMA) layer was spin coated on the graphene/copper film and then cured at 180 ℃ for 1 minute. The copper substrate was removed in ammonium persulfate ($(NH_4)_2SO_4$) solution at room temperature for over 12 hours. The PMMA supported graphene was rinsed by deionized water and then transferred onto the waveguide, and then cured at 180 ℃ for 3 minutes. Finally, the PMMA was dissolved by acetone for 30 minutes.

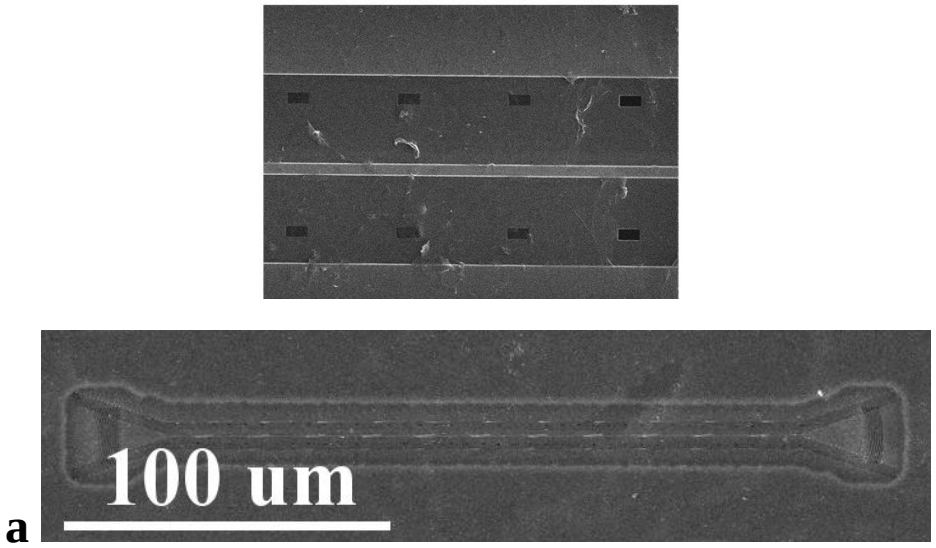

a

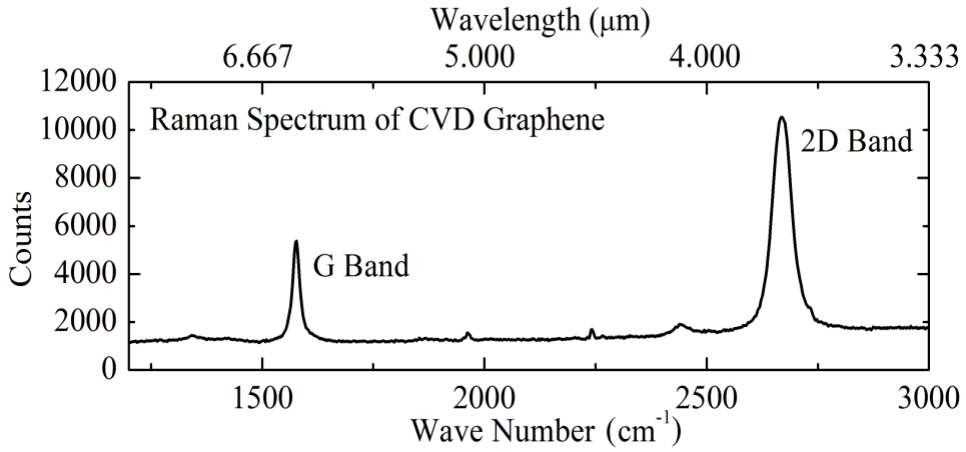

b

Figure 4.7 (a) SEM images of fabricated device. (b) Raman spectroscopy directly of the fabricated device surface.

Figure 4.7a shows the SEM image of fabricated device. We can see that a layer of graphene is covering on top of the silicon waveguide. And the periodic holes beside the waveguide are open and part of the BOX is etched away. In order to further verify the existence of the graphene and the number of graphene layer, we employed a Raman spectroscopy directly on the fabricated device. The result is shown in Figure 4.7b. It shows a symmetric 2D peak at 2671 cm^{-1} with a FWHM of 41.8 cm^{-1}.

Also, the G-to-2D peak intensity ratio is <0.5. They show that the graphene exists on the silicon waveguides and is single layer.

The total insertion loss of graphene on waveguide (175 μm) and two focusing subwavelength grating couplers is ~21 dB and ~25 dB at 1530 nm and 1560 nm, respectively. By comparing the insertion loss of sample with different waveguide lengths, we obtain the propagation loss of the graphene on waveguide of ~0.088 dB/μm which matches the value in Figure 6.1 for the graphene optical modulator at absorbing operation.

4.5 Saturable absorption

To verify the saturable absorption in this hybrid waveguide structure, a power dependent transmission measurement is performed. The experimental setup is show in Figure 4.8. A figure-eight mode-locked fiber laser generates a mode-locked pulse train with, repetition rate of 18 MHz, pulsewidth of 840 fs and centre wavelength of 1565 nm. The pulses are amplified by an EDFA. The optical power of is controlled by a variable optical attenuator (VOA). 10% of the optical power is tapped out and measured by power meter for monitoring, further attenuated before the power meter for protection. 90% will go to the graphene on silicon waveguide with PC for optimizing the coupling with input grating coupler. Finally, the output from the waveguide is measured by another power meter. By varying the input power, we obtain the power dependent transmission ratio, as shown in Figure 4.9.

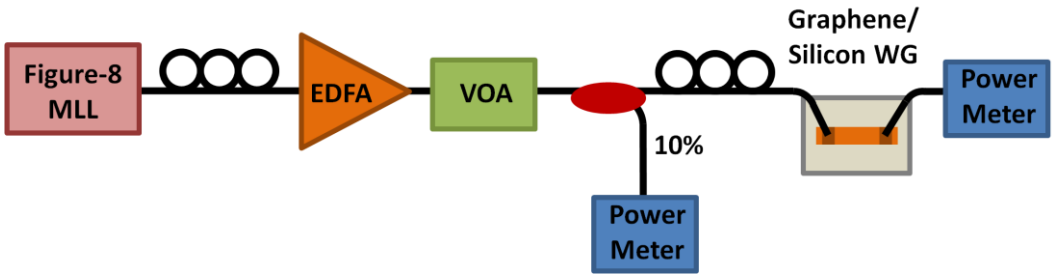

Figure 4.8 Experimental setup of saturable absorption measurement.

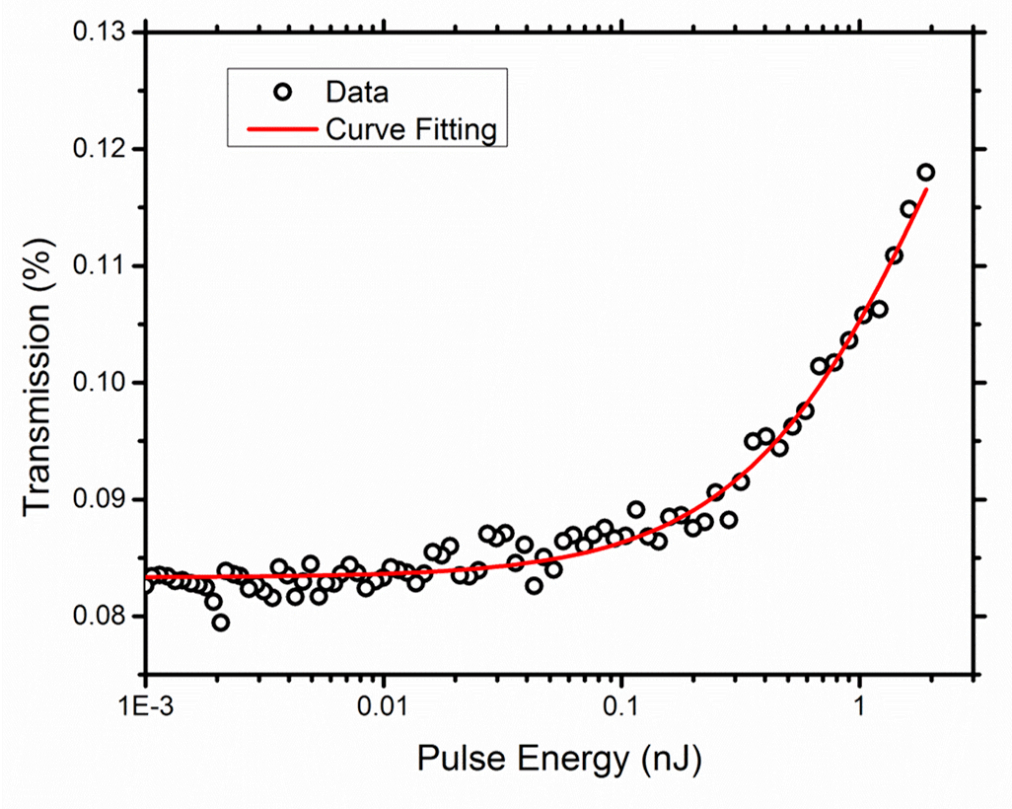

Figure 4.9 Power dependent transmission ratio of graphene on silicon waveguide.

We can see that the transmission dramatically increases at pulse energy around 0.2 nJ. When the pulse energy is up to 2 nJ, the transmission ratio is about 50% higher than low power regime. It clearly shows the saturable absorption occurs in our

sample and the change of transmission is higher than the case of normal incident [107].

4.6 Passive mode-locked laser

To achieve a passive mode-locked laser, the laser configuration using the hybrid waveguide is shown in Figure 4.10. A 2.8 m length of erbium-doped fiber (EDF, Liekki Er-80) acts as the optical gain medium. The gain medium was pumped by a 1480 nm laser diode through a wavelength-division-multiplexer (WDM). An isolator (ISO) after the EDF ensures the laser operating unidirectionally in the ring cavity. The graphene on silicon waveguide was placed after the 10/90 output coupler of the laser. As the coupling efficiency of the grating coupler between fiber and silicon waveguide is polarization dependent, polarization controller (PC) was inserted following the output coupler in order to ensure reasonable optical power in the

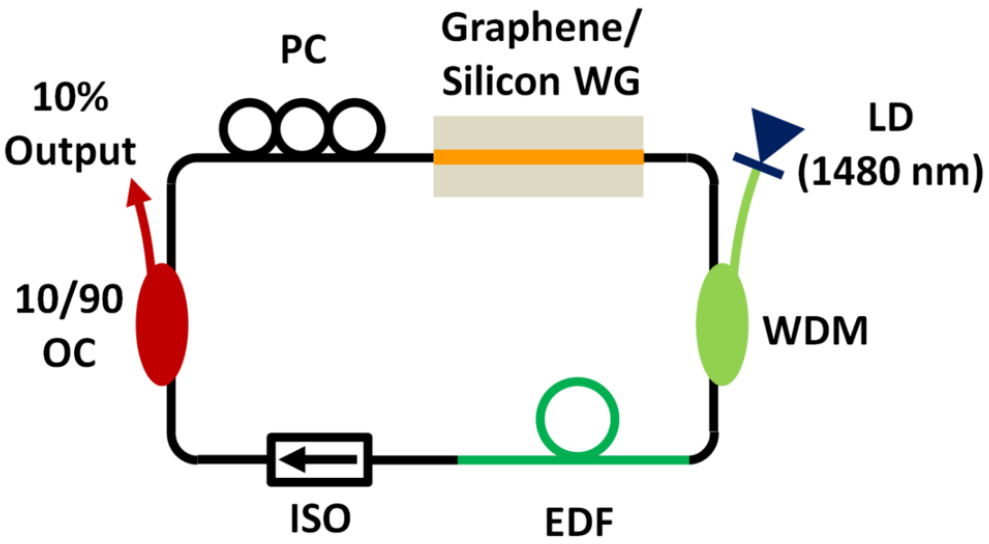

Figure 4.10 Laser configuration of graphene on silicon waveguide mode-locked laser.

silicon for the triggering sufficient saturable absorption. The total cavity length is 11.5 m.

In order to confirm the EDF is able to compensate the cavity loss (including the insertion loss of the chip), we measured the small signal gain of an input signal at 1555 nm with power of -30 dBm. Figure 4.11 shows the gain as a function of pump laser driving current. We can see that the maximum gain is over 30 dB which is sufficient to compensate the cavity loss.

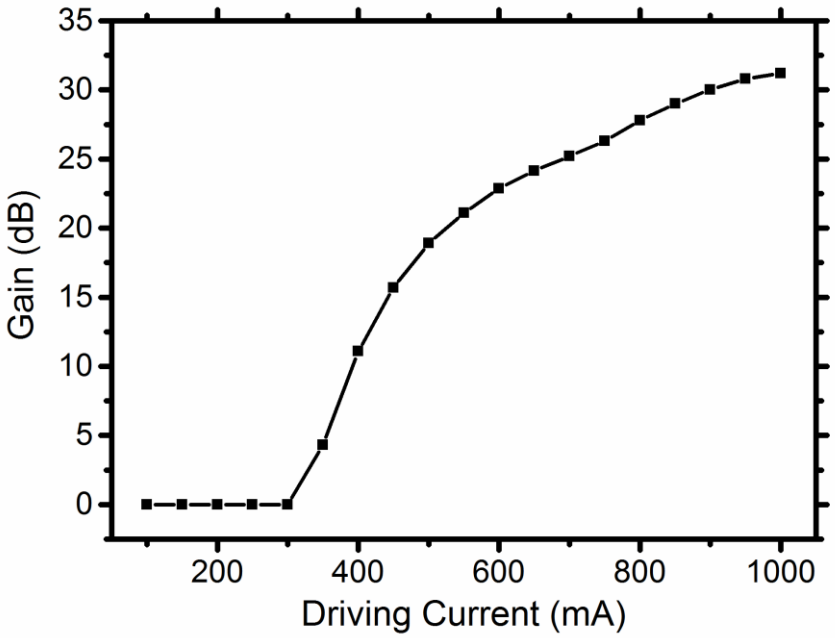

Figure 4.11 Small signal gain of a 2.8 m length of EDF.

4.7 Results and discussions

The continuous wave (CW) lasing threshold of pump power is ~110 mW. By adjusting the PC, a stable mode-locked pulse train was obtained at pump power of 140 mW. The repetition rate of 17.8 MHz matches the cavity roundtrip time, as

shown in Figure 4.12a,b. Mode-locking was maintained when the pump power was decreased to ~120 mW. The mode-locking threshold is higher than the 100 mW

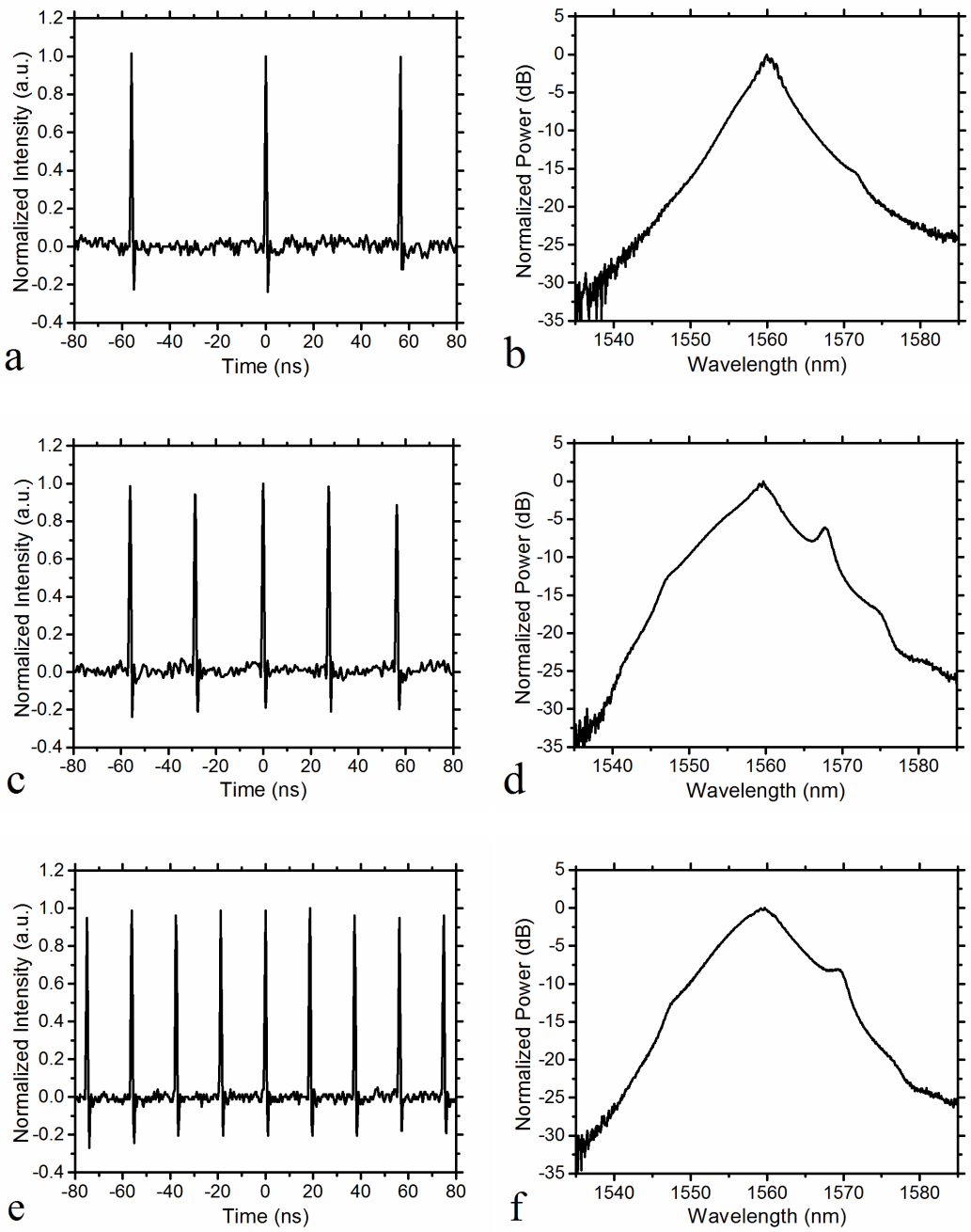

Figure 4.12 The oscilloscope traces of pulse trains and optical spectra of the laser using graphene on silicon waveguide: (a,b) 1st harmonic mode-locking; (c,d) 2nd harmonic mode-locking; (e,f) 3rd harmonic mode-locking.

threshold obtained in previous work using normal incidence to the graphene in an all-fiber cavity [137] because of the excess loss of the waveguide. When the pump power was low, there was residual CW light at ~1560 nm in the laser output. By increasing the pump power, the CW output was decreased and the laser started 2nd harmonic mode-locking at pump power of ~160 mW with repetition rate 35.6 MHz, as shown in Figure 4.12c,d. When the pump power was increased to ~180 mW, the residual CW was suppressed and the laser starts 3rd harmonic mode-locking with repetition rate 53.4 MHz, as shown in Figure 4.12e,f. The central wavelength of the output spectrum is ~1560 nm. The full-width-half-maximum (FWHM) spectral bandwidth is ~7 nm.

Fig. 2c shows the autocorrelation trace of the pulse measured by autocorrelator with 5.5 m of SMF from the laser output, with FWHM of 2.2 ps. By assuming a $sech^2$ pulse profile, the deconvolved pulse width is 1.4 ps FWHM. The length of the graphene on silicon waveguide was not optimized in this laser.

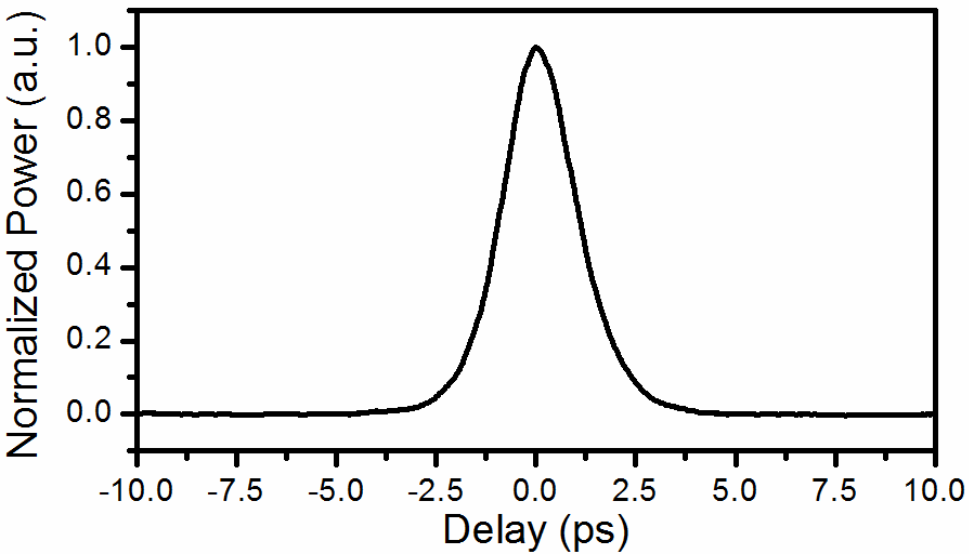

Figure 4.13 Autocorrelation pulse trace of 3rd harmonic mode-locked laser.

There is excess in-plane absorption loss from the graphene, of about 8 dB. The excess loss may be reduced by shortening the length of the graphene on silicon waveguide.

4.8 Conclusions

In conclusion, a graphene on silicon waveguide based saturable absorber was fabricated and used to successfully demonstrate a passive mode-locked fiber laser at central wavelength of ~1560 nm. Stable pulse trains were produced at 20.7-53.4 MHz repetition rates with 7 nm spectral bandwidth and 1.4 ps pulse width. The results show the graphene on silicon waveguide hybrid structure provides a compact and low-cost saturable absorber for graphene based silicon photonics and can be easily integrated with other waveguide devices (such as WDM coupler, output coupler and tunable filters) for a compact fiber laser.

5 Beyond near-infrared

5.1 Introduction

In previous chapters, we have focused on the integrated laser systems for sensing and communication applications in near-infrared (near-IR) region. In fact, for remote gas detection, biomolecular sensing and infrared spectroscopy, it is more useful to extend the wavelengths to mid-infrared (mid-IR), 2-6 μm since the vibrational and rotational resonances of common molecular bonds fall within the mid-IR spectral range [138], [139], as shown in Figure 5.1. For communication, 3-5 μm is the common atmospheric transmission window for free-space communication in commercial and military applications [140], [141], [142].

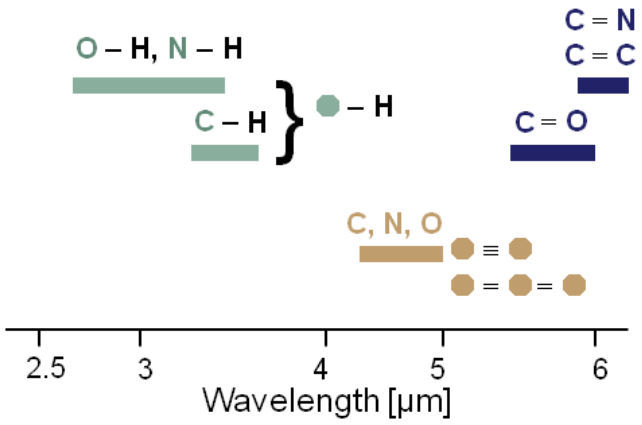

Figure 5.1 Absorption resonances of common molecular bonds within mid-IR.

Silicon photonics in mid-IR have attracted a great interest because of their potential to transfer their successes of sensing and communications to mid-IR region

since silicon has the transmission window in 2-8 μm. As mentioned in previous chapters, the nonlinear effects of silicon in near-IR are limited by TPA and FCA. Although the FCA can be suppressed by using p-i-n diode structure, TPA is unavoidable. In the wavelength beyond 2 μm, TPA in silicon is not possible and the three-photon absorption is almost negligible. The applications of optical nonlinearities in silicon can be faster and more efficient. High efficient parametric optical amplifier and wavelength conversion by setting the pump wavelength in ~2.2 μm have been demonstrated in SOI waveguide recently [71], [143], [144], [145], [146]. It is natural to extend our works in previous chapters to mid-IR region.

In order to transfer the integrated EDF lasers to mid-IR, we have to find the mid-IR counterparts of the laser building blocks. One of the major components is the active fiber for mid-IR. However, fused silica has high absorption at wavelengths between 2.6-6.0 μm (with a narrow transparent window around 3.2 μm) [140], [147], [148], as shown in Figure 5.2. It limits the conventional silica fiber technologies to

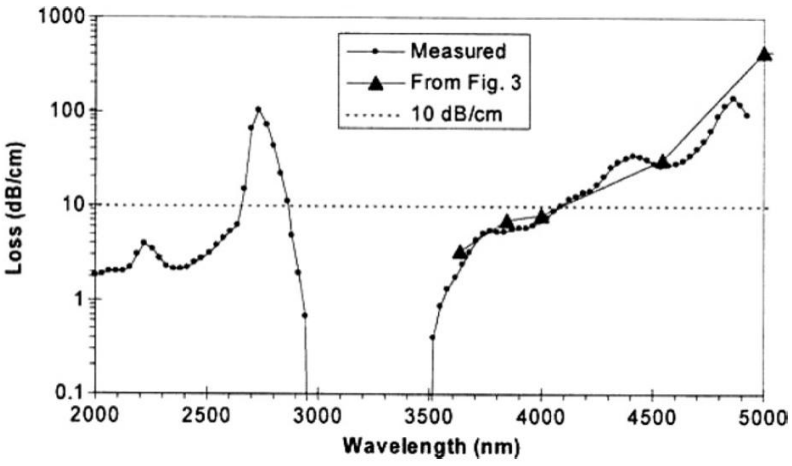

Figure 5.2 Absorption loss of glassy SiO_2 at 300 K between 2-5 μm, adapted from [140].

<2.6 μm or ~3.2 μm. There are several alternative materials for mid-IR fibers. One type of the most promising materials is fluoride glass which is a class of non-oxide optical glasses formed by a composite of different fluorides. The famous example is

ZBLAN glass group which is composed of zirconium, barium, lanthanum, aluminum, and sodium fluorides (ZrF_4-BaF_2-LaF_3-AlF_3-NaF). ZBLAN fiber has very low optical attenuation up to 6 μm. Moreover, it can be doped to make an active fiber with gain wavelengths 2.7-3.0 μm [149].

As the same reason as optical fiber, the conventional SOI based devices are not suitable for mid-IR because of the BOX layer. Fortunately, silicon-on-sapphire (SOS) provides an alternative potential platform for mid-IR devices due to the high transparency of sapphire in mid-IR [140], as shown in Figure 5.3. SOS based waveguides have been proposed and demonstrated experimentally in the wavelength range of 1.5-5.6 μm [150], [151]. Recently, microring resonators were reported operating in the 5.5 μm wavelength range [152]. Furthermore, a number of fiber-based components in near-IR are hard to find their mid-IR versions, for examples,

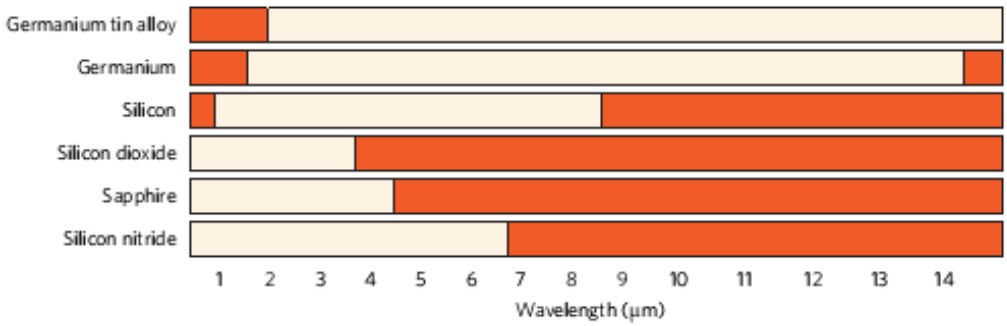

Figure 5.3 Propagation losses for different materials. The white areas represent optical transparency (loss is <2 dB/cm). Figure is adapted from [141].

comb filters and directional couplers. By making use of the flexibility of silicon photonic platform, these components can be fabricated on the chip for mid-IR if there are the near-IR counterparts. To be the first step, MRR is a reasonable choice for developing the fabrication processes and characterization methods of mid-IR silicon photonic platform.

For MRR, thermal stability is crucial in practical usage. The thermo-optic coefficient of silicon is higher than silica, and has a value of $(1.86\pm0.08)\times10^{-4}$ K^{-1} at 1.5 μm wavelength [153]. Silicon waveguide devices are thus more sensitive to temperature than devices based on silica [154]. The thermo-optic coefficient of bulk silicon has been measured in mid-IR range up to 6.0 μm [25]. However, the value of strained silicon thin film such as epitaxial layer of SOS have not been studied in mid-IR range as it is difficult to form a conventional etalon (such as described in [153]) since the thickness of the silicon layer can be less than the wavelength in the mid-IR range.

In this chapter, we report on the measurement of the thermal-optic coefficient of SOS waveguides and *Q* factor measurement of MRRs at a wavelength of 2.75 μm. We fabricated mid-IR microring resonators which support a fundamental quasi-TE mode. The devices were characterized by thermal tuning using a fixed wavelength Er/Pr-codoped ZBLAN fiber laser at 2.75 μm [40]. A method of *Q* factor estimation by temperature scanning transmission curve is proposed. It does not need any curve fitting. Similar results are obtained if we assume the ratio of resonant period (in temperature) to the FWHM of resonant dip/peak, $\Delta T/\delta T$, is equal to the cavity finesse [41]. Finally, the thermo-optic coefficient of the epitaxial silicon layer of SOS is also

estimated by perturbation method [42], [43]. The measurement techniques were verified with conventional SOI microring resonators in near-IR.

5.2 Mid-infrared microring resonators

In the 2.3-3.0 μm range, there are a number of potential applications of microresonators for chemical sensing and nonlinear generation of mid-IR light. For chemical sensing, the hydroxyl (OH) group and ammonia NH_3 have strong absorption peaks spectrum in this region Figure 5.4 [155], [156], and thus the sensitivity of evanescent optical waveguide based sensors [32], [157], may be sufficient to detect trace concentrations.

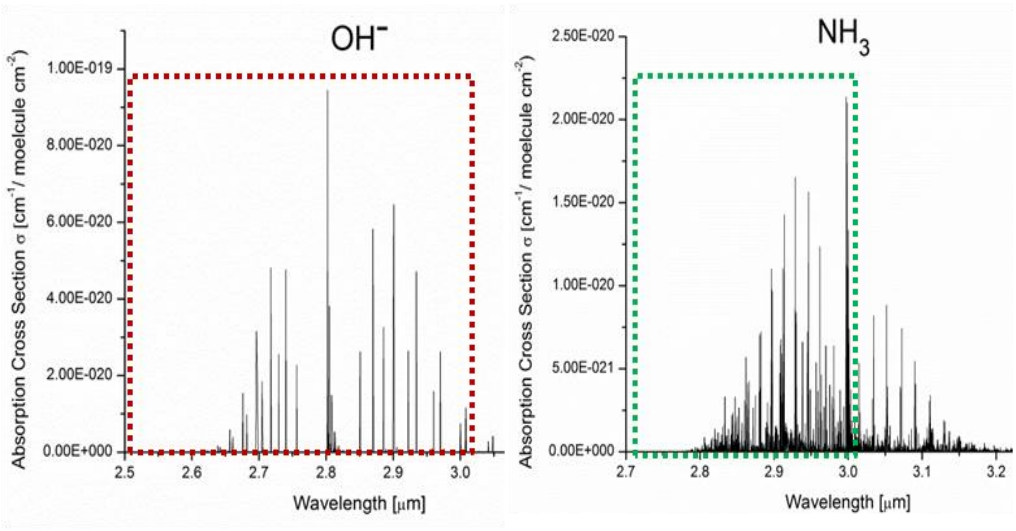

Figure 5.4 Absorption spectra of hydroxyl and ammonia from HITRAN database [156].

For optical nonlinearities, silicon in the mid-IR is also of interest for use in generating different mid-IR wavelengths such as mid-IR silicon Raman amplifier [143], [144], or optical parametric amplifiers [145], [146]. Making use of the

intensity enhancement in MRR, it is possible to further enhance the nonlinear processes and decrease the footprint of the devices. In case of high-*Q* MRRs, it is possible to achieve Raman lasers or OPOs. According to the experimental measurement of the Kerr coefficient of silicon, n_2, the parametric process will decrease dramatically for the wavelengths beyond 3.0 μm since it is too far from the resonance wavelength ~1.12 μm (silicon band gap energy of 1.12 *e*V). On the other hand, the TPA will be absent in photon energy below half of the band gap, about beyond 2.3 μm. Also, there will be much less free-carriers which lead to shifts in resonances of the MRRs and introduce the instability to the system, e.g. bistability [158], [159]. Therefore, 2.3-3.0 μm range is the wavelength window of high Kerr nonlinearity without TPA for silicon photonics. Comparing with SOI, SOS wavelength will not be limited to the wavelength <2.6 μm due to the high absorption of BOX layer. It is an ideal platform for making the mid-IR versions of the integrated optical sensing laser systems proposed in previous chapters.

As the first step, we have to develop the characterization skill in mid-IR. The most important parameter of MRR is *Q*. However, the measurement method of *Q* at mid-IR is limited. In 2.3-3.0 μm range, there is a lack of narrow linewidth tunable laser sources. In 3-6 μm range, the conventional quantum cascade lasers (QCLs) provide limited spectral resolution in the order of 0.1 nm and set a limit on the maximum measurable *Q* using this source. In order to overcome the limitation of the laser source, there is a need of an alternative *Q* measurement method with narrow linewidth laser sources such as a mid-IR He-Ne laser. Since the refractive index of silicon is not depended on wavelength only, we can change another parameter to control the resonant condition of the MRR for fixed wavelength. As mentioned

above, silicon refractive index is very sensitive to temperature. If we are able to control the temperature of the MRR, it is possible to get the information of *Q* from the temperature dependent transmission.

5.3 ZBLAN fiber laser

The mid-IR laser source in the 2.6-3.0 μm range is very limited. There is no commercial QCL in this range. The linewidth of mid-IR OPO is quite broad due to its pulsation nature. It is a reasonable choice to choose the ZBLAN fiber laser since we are target to achieve mid-IR integrated fiber laser. Also, high power ZBLAN fiber laser have been demonstrated, with average power up to 24 W, recently [160].

Mid-IR emission around 2.7 μm in ZBLAN fiber can be achieved by doping Er^{3+} (Erbium) ions via the transition $^4I_{11/2}$ to $^4I_{13/2}$, as shown in Figure 5.5 [161]. However, the life time of $^4I_{13/2}$ (lower state) is longer than $^4I_{11/2}$ (upper state). Therefore, the electrons will be accumulated in $^4I_{13/2}$ and limits the power conversion efficiency. In order to solve this problem by doping Pr^{3+} (Praseodymium) ions which introduce an energy transfer (ET) process to reduce the population of $^4I_{13/2}$.

The ZBALAN fiber core is co-doped by Er and Pr, with concentration of 30000 ppm and 5000 ppm, respectively. The core diameter and the numerical aperture (NA) are 9 μm and 0.25, respectively. Double cladding designed is employed to provide a good coupling to the high intensity pump (wavelength of 975 nm) without thermal damage, as shown in Figure 5.6. The inner cladding (as the core for pump wavelength) has the diameter and NA of 140 μm and 0.5, respectively.

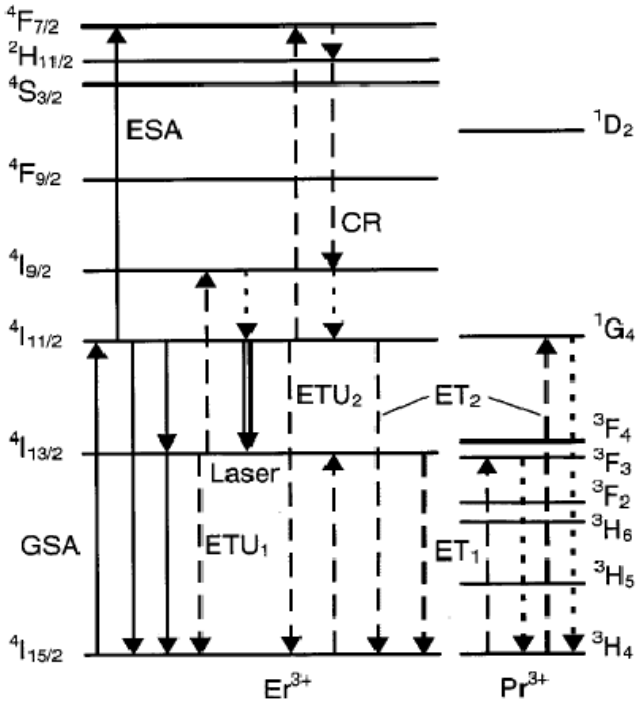

Figure 5.5 The energy-levels of erbium and praseodymium ions, adapted from [161].

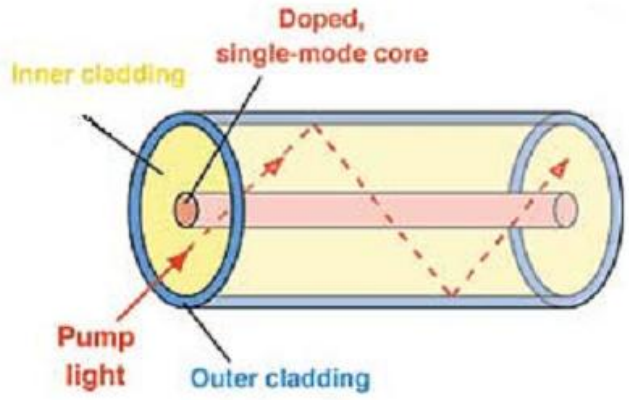

Figure 5.6 Schematic diagram of the double cladding ZBLAN fiber.

By using a 975nm multimode laser diode as the pump laser (Bookham Co.), the ZBLAN fiber (~4 m) will have ASE in 2.7-2.8 μm with green light as byproduct, as shown in Figure 5.7a. If the pump power is up to 3.4 W, the fiber starts to lase by compensation to the loss of two fiber facets (~4% back reflection due to the facets). Figure 5.7b shows the output spectrum of the laser and the ASE below threshold. The center wavelength of the laser is about 2.75 μm. The line width is limited by the resolution of the spectrometer.

a

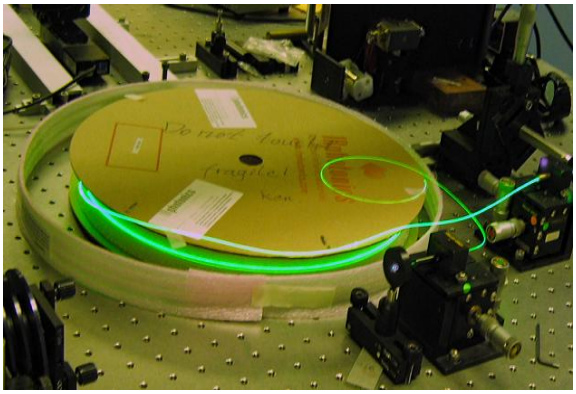

b

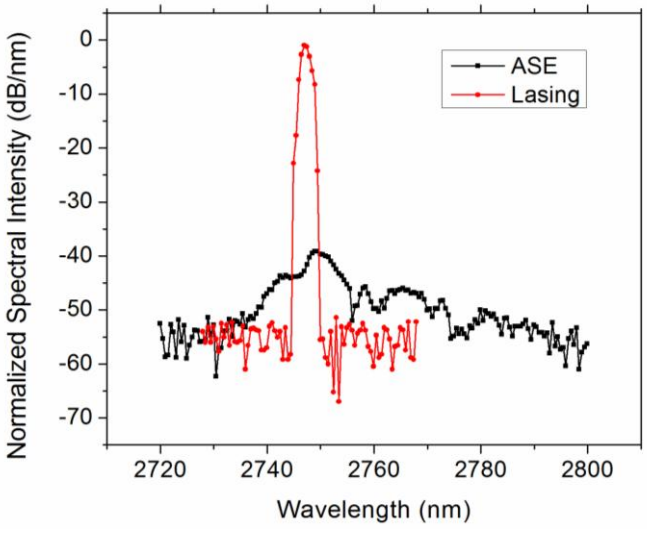

Figure 5.7 (a) Image of 975 nm pumped ZBLAN fiber. (b) Normalized spectral intensity of the Er/Pr co-doped ZBLAN fiber laser compared with ASE.

5.4 Design & fabrication

The silicon strip waveguides were fabricated on SOS with 600 nm thickness and 950 nm width which satisfy the single mode condition of quasi-TE mode at 2.75 μm. The corresponding electric field mode profile are calculated by finite element method (FEM), as shown in Figure 5.9b, with refractive indices of 3.44 (silicon), 1.72 (sapphire) and 1 (air) in mid-IR at room temperature [162]. For microring resonators, in order to have a better control of the coupling between the ring cavities and the bus waveguides, the race-track type geometry was used. They were fabricated with 30-45 μm coupling length and 60-150 μm bending radius, and thus with 437-1032 μm round-trip length. According to simulations using beam propagation method, the bending loss of the waveguides with 60-150 μm bending radius is theoretically negligible compared to the propagation loss of the waveguides. In this paper, microring resonators with two bus waveguides were used. In order to simply the design, the two bus waveguides of each resonator have identical coupling lengths and separation from the ring waveguide.

Grating couplers are used for coupling mid-IR light between the SOS waveguides and single mode ZBLAN fibers with a 10 ° off-vertical orientation [163], as shown in Figure 5.10b. The uniform-1D gratings were 360 nm shallow-etched in a period of 1.055 μm and 0.31 fill factor. They also ensure the light polarization of waveguides and rings in TE mode.

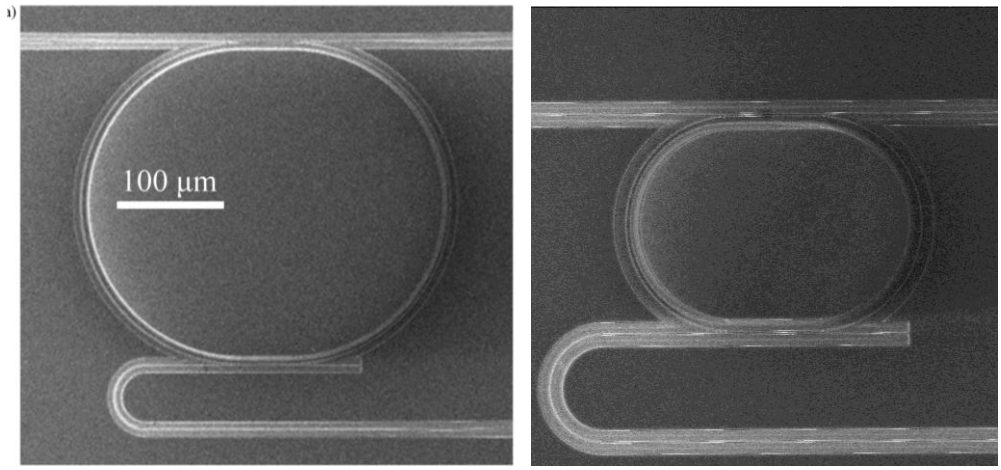

Figure 5.8 SEM image of the race-track microring resonators of 1032 μm round-trip length (left) and 437 μm round-trip length (right).

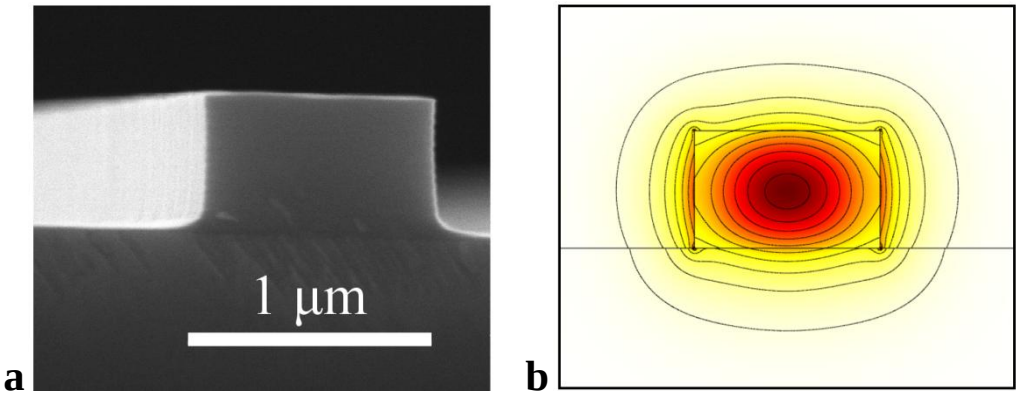

Figure 5.9 (a) SEM image of waveguide cross-section; (b) the electric field mode profile of corresponding quasi-TE mode, calculated by FEM.

The microring resonators and grating couplers were patterned by electron beam lithography with ZEP520A resist and then dry etched by reactive-ion etching with C_4F_8 and SF_6 mixture. The scanning electron microscope (SEM) images of the fabricated microring resonator and the strip waveguide cross-section are shown in Figure 5.8 and Figure 5.9.

For comparison in near-IR, a SOI microring resonator (TE mode) was fabricated on a wafer with 220 nm top silicon layer and 2 μm BOX by deep-UV lithography. The waveguide width and round-trip length are 500 nm and 264 μm respectively.

5.5 Experimental Setup

The experimental setup is shown in Fig. 2. The Er/Pr-codoped ZBLAN fiber laser with lasing wavelength at 2.75 μm and linewidth < 0.12 nm was pumped by a high power 975 nm diode laser. The mid-IR light from the laser was coupled to an un-doped ZBLAN fiber. And then the light is coupled from un-doped ZBLAN fiber to the input of the resonator through grating coupler. Another fiber collected the output light from either the throughput port or the drop port of the resonator by grating couplers. Finally, the output light was captured by a mid-IR photovoltaic detector. In order to increase the signal-to-noise ratio, the signal of the mid-IR detector was measured by a lock-in amplifier with a mechanical chopper modulating the pump laser. The SOS chip was mounted on top of a thermoelectric cooling (TEC) for temperature tuning. A thermal detector was attached on the TEC for monitoring the temperature and TEC control feedback. The light from the throughput port and drop port was measured at 25-85 °C. The received signal is finally normalized by the output of a reference straight waveguide in order to remove the temperature dependence of the coupling efficiency of the grating couplers. In the case of SOI microring measurement, the fibers, laser source and detector were replaced by fused silica single-mode fibers, a tunable laser and an optical power meter for near-IR.

Figure 5.10 Schematic diagram of measurement setup: (a) Mid-IR light coupled into input port (**I**) and coupled out from throughput port (**T**) or drop port (**D**) of the microring resonator on SOS. The temperature of the silicon waveguide is controlled by the TEC attached under the sample and acquired by thermal detector direct attached on TEC. The output signal is collected by mid-IR photodiode with lock-in amplifier and mechanical chopped pump laser. (b) The input light coupled in (red) from undoped ZBLAN fiber to the input port of the microring resonator and coupled out to the fiber from either throughput port (green) or drop port (yellow) through grating couplers.

5.6 Results & analysis

5.6.1 Temperature dependent transmission of small MRR

We first start from a smaller MRR. The temperature dependent transmission of MRR with 437 μm round trip length is plotted in Figure 5.11. By tuning the temperature between 25-85 °C, we can observe four resonances in both throughput and drop ports with ~11 °C temperature spacing and extinction ratio of ~10 dB from

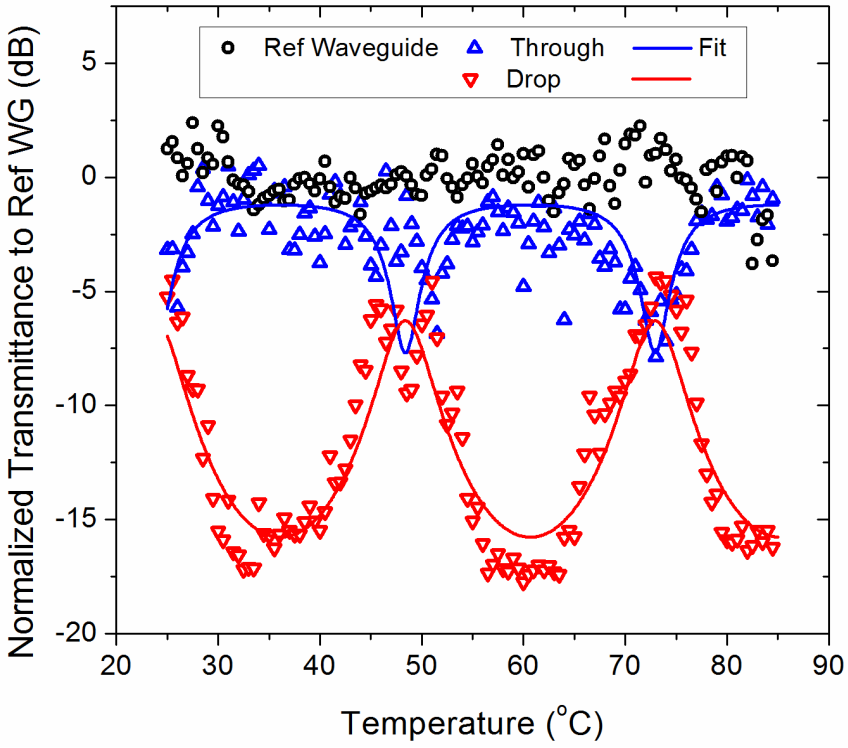

Figure 5.11 Normalized temperature dependence transmission of the quasi-TE MRR (with 437 μm round-trip length) at 25-65 °C of throughput port (blue) and drop port (red).

the drop port. There is ~10 dB loss from the drop port at resonance compared to the reference waveguide (without MRR).

We can observe an extinction ratio of ~10dB from the drop port signal. There is about 6dB loss from the drop port at resonance compared to reference waveguide (black circle). The period is about 25 °C. The measured transmittance was analyzed by a theoretical model of the MRR in Section 3.3.1 (refer to the Eq. (3.11)) with temperature, T, dependent round-trip phase shift $\theta(T) = \theta(T_o) + \Delta\theta(T)$:

$$\Delta\theta(T) \cong 2\pi L_{rt} \left.\frac{\partial n_{eff}}{\partial T}\right|_{\lambda_o} \frac{T - T_o}{\lambda_o}, \tag{5.1}$$

where L_{rt} is the physical round-trip length; n_{eff} is the effective index of the waveguide mode; λ_o is the wavelength in vacuum; T_o is the reference temperature; $\partial n_{eff}/\partial T$ is the thermo-optic coefficient of the waveguide mode which depends on the waveguide material (air, silicon and sapphire) and the mode field profile. In order to simplify the model, the propagation loss and the coupling efficiency between the waveguides and the ring are assumed to be temperature independent. Moreover, the linear thermal expansion of silicon is in the order of 10^{-6} K^{-1} [164] which is two orders of magnitude less than the thermo-optic effect of silicon, and therefore neglected in our analysis. The fitting curves of temperature scanning of the microring, shown in Fig. 3b, agree well with the experimental data with fitting parameters α = 0. 73, $|t|$ = 0.33 and n_{eff} = 2.72. The fluctuations of the data were due to the thermally induced misalignment in the setup. At high temperature, the open system introduces stronger air flow due to the larger different between the air near the sample and the

atmosphere. Such air flow may introduce additional mechanic fluctuations of the fibers.

5.6.2 Temperature dependent transmission of large MRR

To get a better result, we have to decrease the temperature scanning range of the

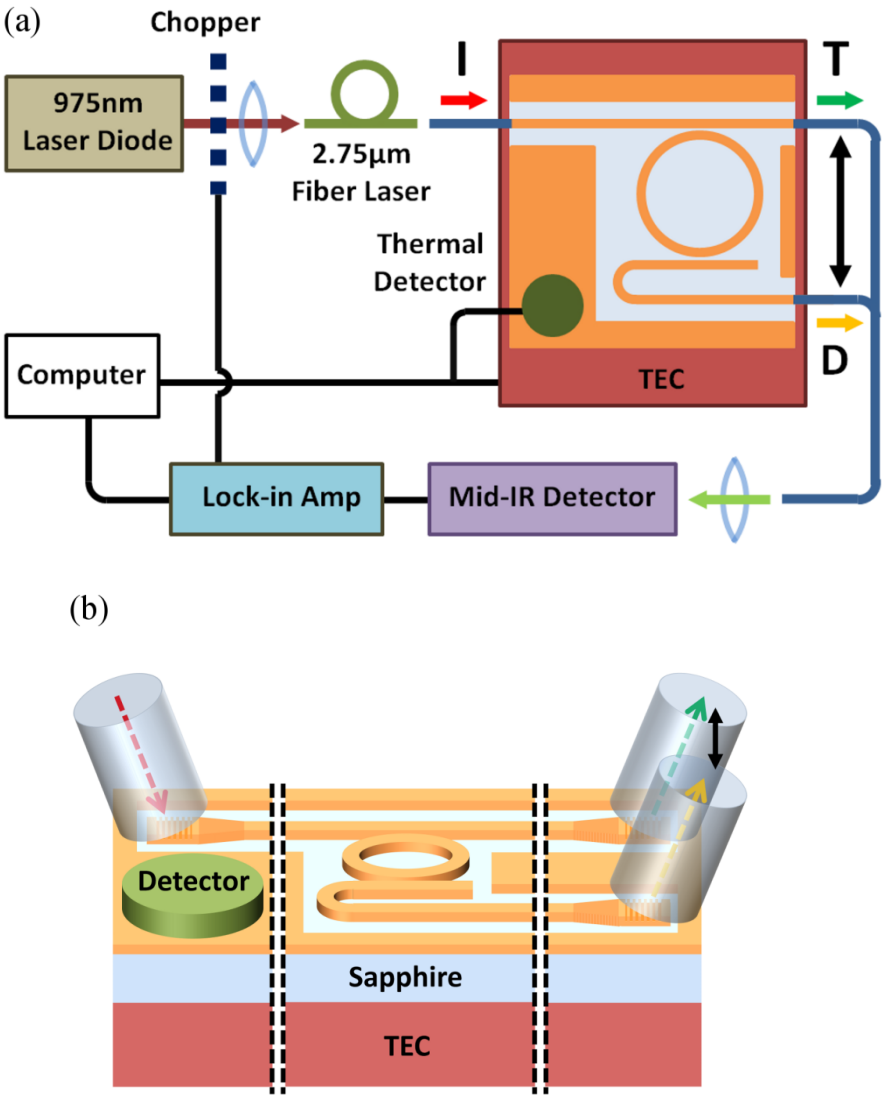

Figure 5.12 Schematic diagram of measurement setup: The temperature of the silicon waveguide is acquired by thermal detector direct attached on the epitaxial silicon.

experiment. It needs a MRR with shorter resonant period in temperature. It can be done by using a MRR with longer round-trip length, by Eq. (5.1). On the other hand, the actual temperature of the silicon layer may have a difference from the TEC due to the thermal resistance of sapphire. Also, there is a delay of the temperature change from TEC to the silicon layer. This delay introduces instability of our thermal control feedback system. In order to solve it, the thermal detector was changed to directly attach on the epitaxial silicon for monitoring the exact surface temperature and providing faster TEC control feedback. Figure 5.12 shows the new experimental configuration.

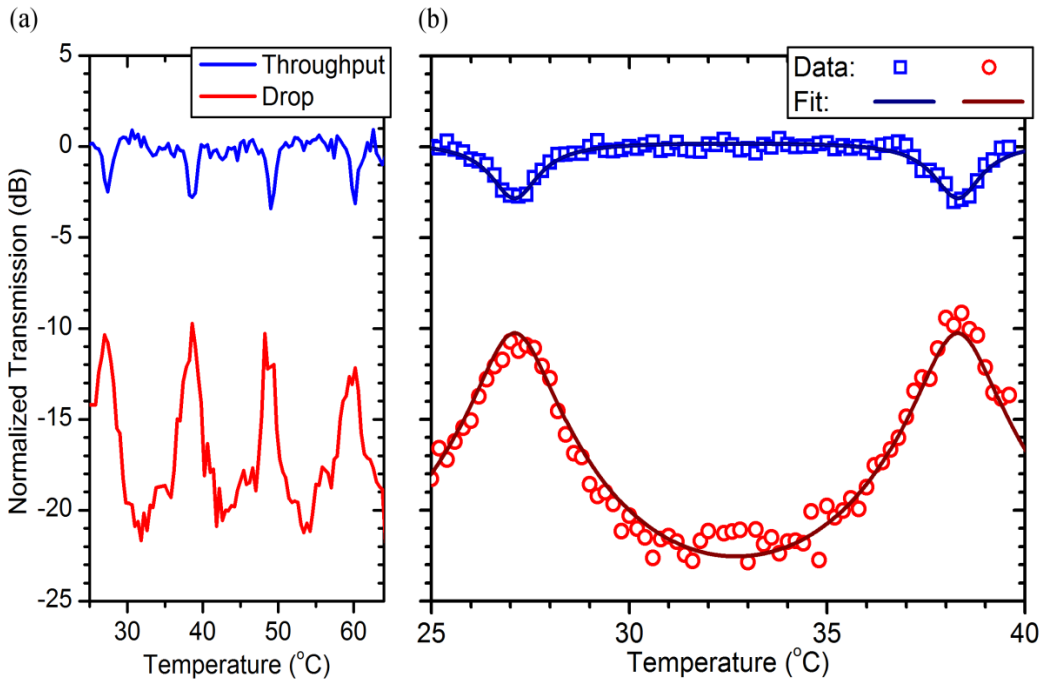

Figure 5.13 Normalized temperature dependence transmission of the quasi-TE microring with 1032 μm round-trip length: (a) temperature scanning at 25-65 °C of throughput port (blue) and drop port (red); (b) temperature scanning at 25-40 °C of throughput port (blue squares) and drop port (red circles) with theoretical fitting curves.

The temperature dependent transmission of the largest MRR with 1032 μm round trip length is plotted in Figure 5.13. By tuning the temperature between 25-65 °C, we can observe four resonances in both throughput and drop ports with ~11 °C temperature spacing and extinction ratio of ~10 dB from the drop port. There is ~10 dB loss from the drop port at resonance compared to the reference waveguide (without resonator). We can see the much more stable transmission curves compared to former ones. The fluctuations of the measurement data in Figure 5.13a may be due to instability in the fiber laser as there laser longitudinal mode hopping and wavelength drift noise may be present during temperature scanning of the microresonator. The measured results could be improved by reducing the temperature scan range (25-40 °C), as shown in Figure 5.13b.

The fitting curves of temperature scanning of the microring, shown in Figure 5.13b, agree well with the experimental data with fitting parameters α = 0.71, $|t|$ = 0.93 and n_{eff} = 2.72. There are fluctuation in the measured values at the drop port, between normalized level -21 dB and -23 dB because of the noise background of the setup.

5.6.3 Quality factor

In order to develop and verify the method for *Q* factor estimation from temperature dependent transmission curve, we can start with a conventional SOI microring for near-IR. The transmission spectrum at 25 °C is shown in Fig. 4a, which shows the *FSR* as 2.08±0.014 nm. Fig. 4b shows the resonant dip of the throughput port centered at 1546 nm with FWHM $\delta\lambda_o$ = 0.08±0.014 nm. The corresponding *Q* factor is about 19900±3500. The figure also shows the resonant wavelength red (blue) shifted with increasing (decreasing) the temperature. We can see that the shape of the

spectral profile of the resonant dip is almost unchanged in this temperature range. For the thermal tuning measurement, we fixed the laser wavelength at the resonant wavelength at 25 °C (1546 nm) and tuned the temperature. When the resonance is shifted by about half of $\delta\lambda_o$ at a temperature shift $\delta T/2$, the output power is changed to the half of resonant dip. Therefore, the temperature shift δT behaves as the FWHM of the resonance in the temperature tuning domain. The relationship between δT and $\delta\lambda_o$ can be obtained directly by considering the resonant condition of the resonator at m-order resonance of λ_m at temperature T with waveguide mode group index $n_g = (n_{eff} - \partial n_{eff}/\partial\lambda_o)/\lambda_o$, the resonant wavelength changes with temperature (see Appendix D):

$$\frac{d\lambda_m}{dT} = \frac{\lambda_m}{n_g}\left.\frac{\partial n_{eff}}{\partial T}\right|_{\lambda_m}, \text{ then } \delta\lambda_o \cong \frac{\lambda_m}{n_g}\left.\frac{\partial n_{eff}}{\partial T}\right|_{\lambda_m}\delta T. \tag{5.2}$$

The thermo-optic coefficient of the waveguide mode can be obtained by considering temperature difference between two resonances in temperature domain, ΔT, of same wavelength λ_o:

$$\left.\frac{\partial n_{eff}}{\partial T}\right|_{\lambda_o} \cong \frac{\lambda_o}{L_{rt}\Delta T}. \tag{5.3}$$

By combining Eqs. (5.2) and (5.3), Q can be expressed as:

$$Q = \frac{\lambda_m}{\delta\lambda_o} \cong \frac{\Delta T}{\delta T}\frac{n_g L_{rt}}{\lambda_m}. \tag{5.4}$$

From the thermal transmission curves at 1546 nm, shown in Fig. 4c-d, the resonant period ΔT is and FWHM δT are 24.7±1.0 ^{o}C and 0.74±0.03 ^{o}C respectively. The mode group index is 4.35 which is obtained by $FSR = \lambda_m^2/n_g L_{rt}$. By Eq. (5), the resulting Q is about 24800±2000. The measured values of Q from the wavelength

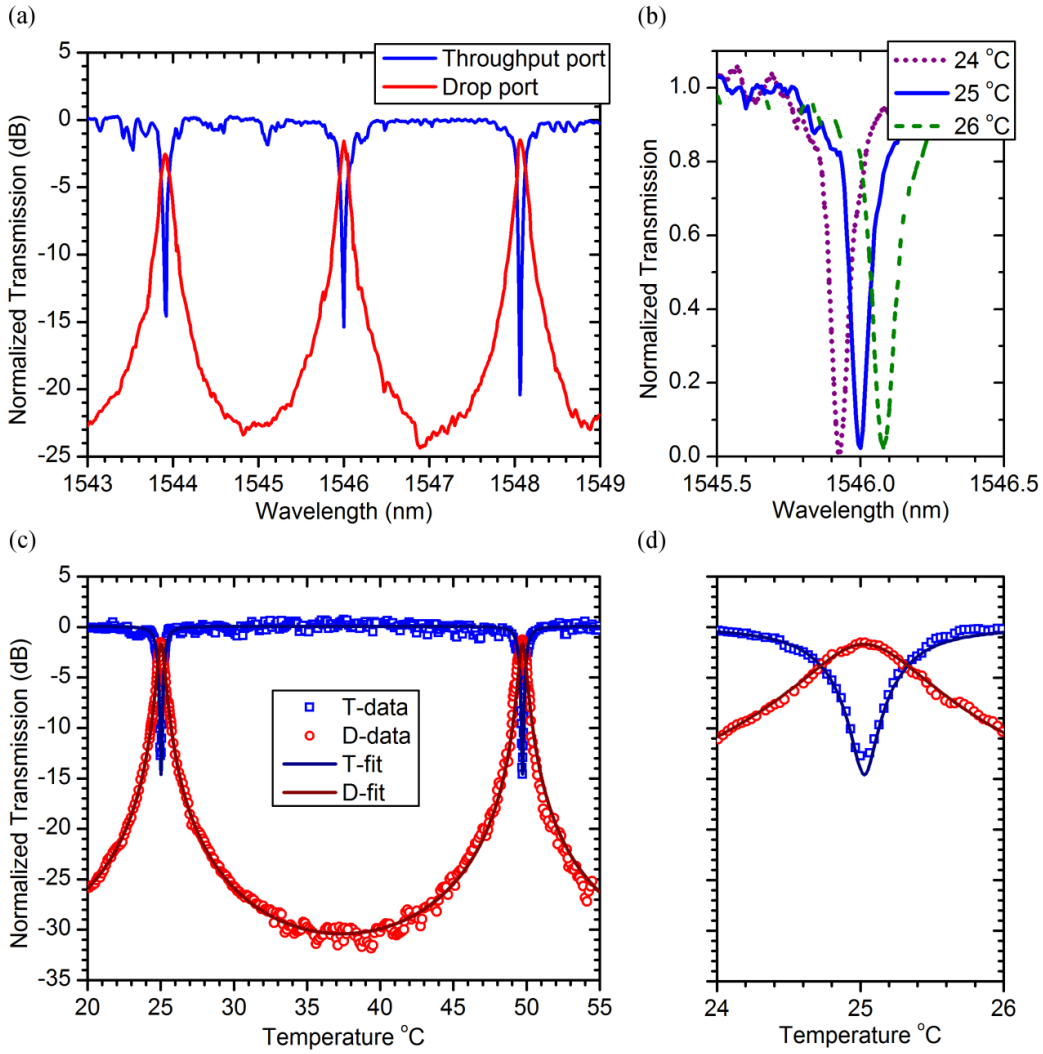

Figure 5.14 Normalized transmission curves of quasi-TE microring with 264 μm round-trip length: (a) wavelength scanning at 25 °C; (b) temperature dependent resonant dip of throughput port in linear scale; (c,d) temperature scanning at 20-55 °C and 24-26 °C fixed in 1546 nm with theoretical fitting curves.

scanning and thermal tuning techniques agree to within the error bars of the different measurement techniques.

By combining Eq. (5.4) and $FSR = \lambda_m^2/n_g L_{rt}$:

$$\frac{\Delta T}{\delta T} \cong \frac{FSR}{\delta \lambda_o} = F \,. \tag{5.5}$$

This gives similar results as obtained by assuming $\Delta T/\delta T$ as being equal to the finesse [41].

As this proposed method works well in near-IR, it was applied in the SOS microring resonators at mid-IR. From Fig. 3b, the resonant period ΔT and dip FWHM δT are 11.2±0.4 ^{o}C and 1.48±0.06 ^{o}C respectively. The theoretical mode group index is 4.01 calculated by FEM. The resulting Q is about 11400±800.

Since the power stability and the linewidth of the ZBLAN fiber laser is not as good as the external-cavity tunable laser, the measurement results of our system, in fact, are the convolution of the actual resonator transmission spectral function and the power spectrum of the laser. Therefore, the features would be averaged or broadened. The estimated Q factor may be underestimated. Using this method with a narrow linewidth laser (such as a mid-IR He-Ne laser), the maximum measurable Q can be up to 10^6 by using a temperature controller system with temperature stability and set point resolution in 0.01 ^{o}C, which is commercially available. This limit is over 10 times of wavelength scanning with QCLs.

5.6.4 Thermo-optic coefficient

The thermo-optic coefficient of the waveguide mode, from Eq. (5.3), can be used to estimate the thermo-optic coefficient of the epitaxial silicon core, $\partial n_{Si}/\partial T$, of SOS by perturbation method [42], [43]. This method is more accurate than conventional mode weighted average method for high index contrast waveguide [165]. A small perturbation of the waveguide materials refractive indices induces the small change of effective index in waveguide mode δn_{eff}:

$$\delta n_{eff} \cong \frac{\int_{\infty}\left(\frac{\partial n(\boldsymbol{r})}{\partial T}\delta T\right) n(\boldsymbol{r})\left|\boldsymbol{E}\right|^2 d\boldsymbol{r}}{Z_o \int_{\infty} \mathrm{Re}\{\boldsymbol{E}\times\boldsymbol{H}^*\}\cdot\boldsymbol{e}_z d\boldsymbol{r}} \cong \Gamma_{Si}\frac{n_g}{n_{Si}}\frac{\partial n_{Si}}{\partial T}\delta T\,, \qquad \text{with } \Gamma_{Si} = \frac{\int_{Si} n(\boldsymbol{r})^2\left|\boldsymbol{E}\right|^2 d\boldsymbol{r}}{\int_{\infty} n(\boldsymbol{r})^2\left|\boldsymbol{E}\right|^2 d\boldsymbol{r}}, \tag{5.6}$$

$$\frac{\partial n_{eff}}{\partial T} \cong \frac{\delta n_{eff}}{\delta T} \cong \Gamma_{Si}\frac{n_g}{n_{Si}}\frac{\partial n_{Si}}{\partial T}\,, \tag{5.7}$$

where Z_o is the impedance of vacuum; and Γ_{Si} is defined as the conventional electric field confinement factor of the mode in silicon core region. In Eq. (5.6), because of the thermo-optic coefficients of sapphire and air is much smaller than silicon [166], [167], and the electric field is highly confined in the silicon core, we can neglect the contribution of them. Moreover, the high thermal conductivity of silicon ensures the temperature can be approximately constant in the core. Again, we start from the SOI counterpart in near-IR. The $\partial n_{eff}/\partial T$ is obtained as $2.37\pm0.10\times10^{-4}$ K^{-1} and then the resulting $\partial n_{Si}/\partial T$ of silicon core of SOI is $2.07\pm0.08\times10^{-4}$ K^{-1} which agrees well to

the result in [153]. The value is smaller than the waveguide mode thermo-optic coefficient since $\Gamma_{Si} \cdot n_g/n_{Si}$ is larger than 1. It is because n_g is larger than n_{Si} while Γ_{Si} is close 1. It indicates that the light in guided mode with large group index spends more time, therefore, experience higher thermo-optic effect than in bulk material for given a length [43].

In case of SOS microring, $\partial n_{eff}/\partial T$ and theoretical group index are obtained as $2.38\pm0.08\times10^{-4}$ K^{-1} and 4.01 respectively. Then $\partial n_{Si}/\partial T$ of epitaxial silicon on SOS is $2.11\pm0.08\times10^{-4}$ K^{-1}. We can see that the resulting value of epitaxial silicon on SOS is similar to the bulk silicon.

5.7 Conclusions

In conclusion, we have fabricated and characterized microring resonators on SOS at wavelength of 2.75 μm by thermal tuning. The measured *Q* factor was about 11400±800 under normal (~60% relative humidity) atmospheric condition. The thermo-optic coefficient of epitaxial silicon on SOS is estimated as $2.11\pm0.08\times10^{-4}$ K^{-1} by perturbation method. The characterization methods have been verified by SOI microring in near-IR with comparable results. The thermal tuning technique for *Q* factor measurement is of practical use for characterizing resonator at wavelengths where there is limited tunability and spectral resolution of laser source and the technique may find applications for other types of cavities such as Fabry–Pérot cavities in mid-IR.

6 Conclusion and future work

6.1 Conclusion

In summary, this thesis described the study of developing silicon integrated EDFLs for optical sensing and high speed communication systems. By combining the successes of silicon photonics in high speed optical communication and chemical/biological sensing, intra cavity silicon photonic devices provide possibility to achieve flexible, potentially low cost laser systems. As the laser output is directly come out from the silicon waveguide, the light source can be used by the on-chip optoelectronic components for optical interconnect or sensing. It greatly simplifies the laser systems and is possible to provide high speed feedback control back to the laser. Moreover, SOI waveguide-related structures have rich optical properties which can be used to achieve a number of different lasers and further simplify the laser configurations. Several compact and simple EDFLs using intracavity SOI photonic devices are proposed.

In Chapter 2, we study the possibility of using the high optical nonlinearity of SOI waveguides to make a multiwavelength EDFL for optical sensing. We have proposed and demonstrated a multiwavelength EDFL which employed FWM in a silicon waveguide to stabilize its output. Using an intracavity F-P comb filter with 100 GHz mode spacing, six lasing wavelengths between 1560.9-1564.9 nm is achieved. In order to enhance the FWM in the SOI waveguide, application of a reverse-bias to remove the free carriers generated by TPA in the SOI waveguide was employed. The power fluctuation of each wavelength due to the gain competition of EDF is reduced from over 40 dB to less than 0.65 dB by the FWM. The proposed laser system should

make possible short cavity length multiwavelength fiber lasers which are suitable for integrated optical sensors. Also, we have observed the high speed periodic pattern in time domain of the laser output. It shows that this kind of laser is also operated under a mode-locking scheme called DFWM which may be able to make a high repetition rate pulse source for optical communication.

In Chapter 3, we continue to simplify the laser system by combining the comb filter and nonlinear SOI wavelength together: making a nonlinear SOI MRR. In DFWM, this kind of configuration, using the filter as the nonlinear components, is called FD-FWM which has been demonstrated using nonlinear high-*Q* silica MRR. However, it is a question whether the lower *Q* silicon MRR has sufficient nonlinearity to achieve FD-FWM. By making use of p-i-n structure to the SOI MRR, we successfully demonstrated a FD-FWM mode-locked fiber laser based on nonlinear silicon MRR. It shows that the silicon MRR has sufficient nonlinearity and quality factor (Q ~50000) for successful operation of the FD-FWM scheme. The mode-locked laser was stable for over an hour at room temperature without any active feedback stabilization. The laser provides a potentially compact and low-cost high repetition rate pulse train source for possible applications in high speed communication and on-chip optical clock.

In Chapter 4, since the limited peak power and pulsewidth in DFWM are not suitable for several optical sensing applications, passive mode-locking scheme using a saturable absorber is introduced. In order to achieve saturable absorption in SOI waveguides, a graphene on silicon waveguide was fabricated. We have clarified the saturable absorption in such device and observed a 50% change in optical transmission. We also successfully demonstrate a passive mode-locked fiber laser at

central wavelength of ~1560 nm. Stable pulse trains were produced at 20.7-53.4 MHz repetition rates with 7 nm spectral bandwidth and 1.4 ps pulse width. The results show the graphene on silicon waveguide hybrid structure provides a compact and low-cost saturable absorber for graphene based silicon photonics. The EDFLs in those chapters can be further simplified by integrated with other waveguide devices, such as WDM coupler, output coupler and tunable filters for achieving compact lasers.

In Chapter 5, we study the possibility to extend our works from near-IR to mid-IR since there are attractive potential sensing/communication applications and more efficient optical nonlinear processes of silicon in this wavelength range. We first started to fabricate and characterize one of the most fundamental silicon photonic devices we have used, the MRR. However, we had to change the SOI platform to SOS platform in order to avoid the high optical attenuation of BOX layer. Also, since there is leak of tunable laser in our wavelength range, we had developed a *Q* measurement method by using a fixed wavelength laser. Finally, we have fabricated and characterized MRRs on SOS at wavelength of 2.75 μm by thermal tuning. The measured *Q* factor was about 11400±800 under normal (~60% relative humidity) atmospheric condition. The thermo-optic coefficient of epitaxial silicon on SOS is estimated as $2.11\pm0.08\times10^{-4}$ K^{-1} by perturbation method. The characterization methods have been verified by SOI microring in near-IR with comparable results. The thermal tuning technique for *Q* factor measurement is of practical use for characterizing resonator at wavelengths where there is limited tunability and spectral resolution of laser source and the technique may find applications for other types of cavities such as Fabry–Pérot cavities in mid-IR.

6.2 Prospects of future work

6.2.1 Alternative gain media

For achieving multiwavelength fiber laser for WDM applications, there are several alternative gain media such as Raman amplifier and semiconductor optical amplifier (SOA) mentioned in Chapter 2 [47], [48]. Both of them do not suffer from gain competition due to their inhomogeneous gain broadening nature. However, Raman amplifier requires higher pump power and highly nonlinear fiber. And it is polarization dependent gain which increases the complexity laser cavity. For SOA, it introduces one more non-fiber structures and also suffers from polarization dependent gain and high temperature sensitivity. Both of them are more complex compared to EDF-based fiber laser.

Similar to EDF, the erbium-doped waveguide amplifier may provide a more compact solution with the advantages of low noise figure and polarization insensitive [168]. By employing erbium-doped waveguide amplifier as the external gain, it may help to achieve a more compact silicon embedded fiber laser. Moreover, it can be integrated to SOI waveguide monolithically [169]. However, the heat generation is still a problem for totally on-chip laser cavity as mentioned before.

6.2.2 Higher nonlinear waveguides

In Chapter 2 and 3, we are basically using the high nonlinearity, Kerr nonlinearity, of the SOI waveguides. There are a number of methods to further enhance the nonlinear processes in SOI platform. The first approach is decreasing the propagation loss of the waveguides, e.g. using etchless waveguide mentioned in Chapter 3 [99],

[170]. Another approach is slow down group velocity of the light (increase the group index). This approach has been used for demonstration of THG in silicon photonic crystal waveguides [63].

The above approaches are still limited by the nonlinearity of silicon itself. In order to break this limit, we can introduce other materials into silicon. One possible solution is using high nonlinear organic material filled slot waveguides [171]. However, the high absorption loss and the life time of this kind of material is still an issue. The better solution may be the one we have used in Chapter 4: graphene. High nonlinearity of graphene has been measured [114]. Also, graphene has much higher availability and higher chemical stability than those organic nonlinear materials. FWM have been demonstrated in graphene on silicon photonic crystal cavity. However, the high linear absorption, as we have measured in Chapter 4, limits the interaction length in graphene on silicon waveguide. Fortunately, this linear absorption depends on the Fermi level of the graphene [112], [127]. From the results of graphene electroabsorption modulator, we can applied the field effect or chemical doping to make graphene becomes “transparent” to certain wavelengths, shown in Figure 6.1 [112]. Furthermore, the electric field induced band gap of bi-layer graphene can also be used to make it transparent to the wavelengths with photon energy less than the band gap energy [127], [172]. However, the nonlinearity of graphene in those “transparent” conditions is still a question but it really worth to study.

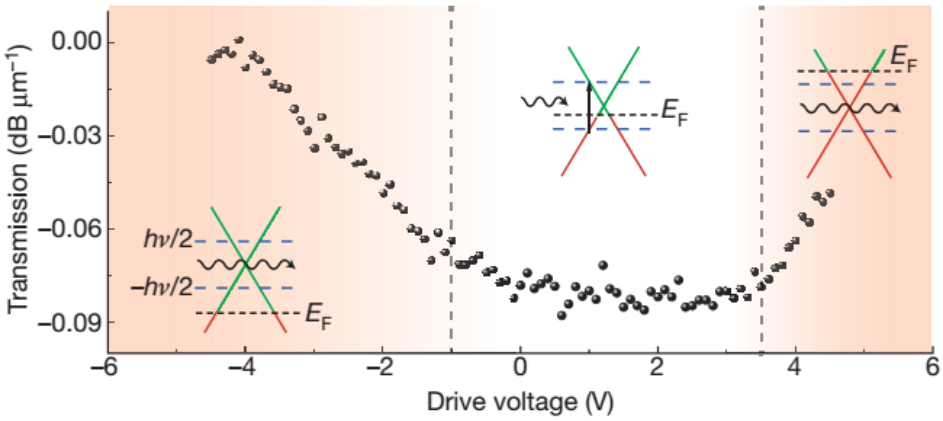

Figure 6.1 Electro-optical response of the device at different drive voltages, adapted from [112].

6.2.3 Nonlinear polarization rotation

In Chapter 4, we used graphene as basis of the saturable absorber to generate high peak power and ultrashort time duration pulses by passive mode-locking. In fact, it may be able to achieve such kind of passive mode-locking by the parametric process only. One of these mode-locking schemes is called nonlinear polarization rotation (NPR) [86], [173]. The schematic illustration is shown in Figure 6.2. If the Kerr medium (waveguide) supports two orthogonal polarization propagation modes, we can launch the light into the waveguide with certain elliptic polarization to excite both polarization modes. If the intensity of the light is high enough, the SPM of two modes will changes their effective indices. The uneven change of their effective indices leads to the rotation of the combined polarization at the waveguide output. If we add a polarization selective element (analyzer) after the waveguide, this system can works as an intensity dependent filter, or so-called “artificial saturable absorber”. As the polarization of the waveguide output rotated, it is the reason of the name of

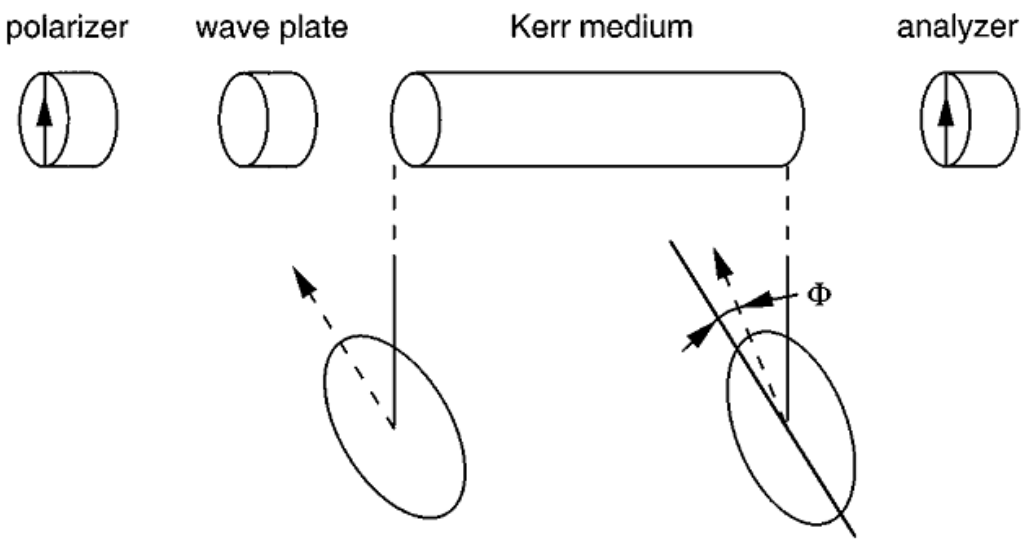

Figure 6.2 Construction of saturable absorber using rotation of elliptic polarization in isotropic medium, adapted from [86].

this effect. Since the parametric process is ultrafast, NPR can be treated as a real fast saturable absorber compared with the others, e.g. SESAM.

NPR has been proposed and demonstrated in SOI waveguides for ultrafast all-optical switching in 2009-2010 [174], [175]. In principle, it can be used for achieving passive mode-locking laser. However, the 1D grating couplers we used in our works can only couple to one polarization, quasi-TE, of the SOI waveguide. In [175], inverse tappers have been used. They can couple both polarizations but the chip is limited by side-way coupling. If we want to make use of the advantages of grating couplers, we still can use polarization diversity grating couplers (2D) grating couplers with on-chip polarization rotator to couple both polarizations to SOI waveguide (or even pure quasi-TE polarization without polarization rotator as normal SOI MZI structures) [176], [177], [178]. However, it will increase the design difficulty of the grating couplers and scarify the coupling efficiency. If we can

achieve on-chip polarization controller, 1D grating couplers can be used for fiber-waveguide coupling and then the polarization of the light can be changed for NPR inside the waveguide.

6.2.4 Mid-infrared integrated laser

In Chapter 5, we have developed the mid-IR SOS platform. In principle, all of our works in near-IR can be transfer to SOS platform. However, the measured propagation loss of SOS waveguide is much higher than the SOI wavelength in near-IR. It is due to the defects of the strained silicon epitaxial layer. It can be solved by using the custom made, ultralow defect SOS wafer.

In order to use commercially available silicon wafer, we can employ silicon SMW structure in Chapter 4 to make use of the mature and high quality single crystallize layer of SOI wafer. By etching out the BOX layer, silicon SMW can guide mid-IR light with low attenuation. We have demonstrated mid-IR silicon SMW platform in 2012 [135], [179]. The TE and TM grating couplers and MRRs has been fabricated and characterized. Silicon SMW can provide a wide low dispersion region from 2.0–5.0 μm for certain waveguide dimension [135]. Furthermore, it can operate at the wavelength range up to 8 μm while SOS is limited by 6 μm due to the sapphire substrate. Silicon SMW provides a potential platform for making silicon integrated fiber laser systems for mid-IR applications.

References

[1] S. E. Miller, “Integrated Optics: An Introduction,” *Bell System Technical Journal*, vol. 48, no. 7, pp. 2059–2069, 1969.

[2] K. C. Kao and G. A. Hockham, “Dielectric-fibre surface waveguides for optical frequencies,” *Electrical Engineers, Proceedings of the Institution of*, vol. 113, no. 7, pp. 1151–1158, 1966.

[3] “Cisco ONS 15454 4-Band Optical Add/Drop Multiplexer Card.” [Online]. Available: http://www.cisco.com/en/US/products/hw/modules/ps5791/ps5811/index.html.

[4] R. Soref, “The Achievements and Challenges of Silicon Photonics,” *Advances in Optical Technologies*, vol. 2008, pp. 1–7, 2008.

[5] R. Soref, “The past, present, and future of silicon photonics,” *IEEE Journal of Selected Topics in Quantum Electronics*, vol. 12, no. 6, pp. 1678–1687, 2006.

[6] R. A. Soref and B. R. Bennett, “Electrooptical effects in silicon,” *IEEE Journal of Quantum Electronics*, vol. 23, no. 1, pp. 123–129, Jan. 1987.

[7] Q. Xu, B. Schmidt, S. Pradhan, and M. Lipson, “Micrometre-scale silicon electro-optic modulator.,” *Nature*, vol. 435, no. 7040, pp. 325–7, May 2005.

[8] A. W. Poon, L. Zhou, F. Xu, C. Li, H. Chen, T. Liang, and Y. Liu, “Silicon Photonics Research in Hong Kong : Microresonator Devices and Optical Nonlinearities,” no. 2, pp. 156–166, 2008.

[9] G. T. Reed, G. Mashanovich, F. Y. Gardes, and D. J. Thomson, “Silicon optical modulators,” *Nature Photonics*, vol. 4, no. 8, pp. 518–526, Jul. 2010.

[10] D. J. Thomson, F. Y. Gardes, J.-M. Fedeli, S. Zlatanovic, Y. Hu, B. P.-P. Kuo, E. Myslivets, N. Alic, S. Radic, G. Z. Mashanovich, and G. T. Reed, “50-Gb/s Silicon Optical Modulator,” *Photonics Technology Letters, IEEE*, vol. 24, no. 4, pp. 234–236, 2012.

[11] J. Michel, J. Liu, and L. C. Kimerling, “High-performance Ge-on-Si photodetectors,” *Nature Photonics*, vol. 4, no. 8, pp. 527–534, Jul. 2010.

[12] M. W. Geis, S. J. Spector, M. E. Grein, J. U. Yoon, D. M. Lennon, and T. M. Lyszczarz, “Silicon waveguide infrared photodiodes with >35 GHz bandwidth and phototransistors with 50 AW-1 response,” *Optics Express*, vol. 17, no. 7, p. 5193, Mar. 2009.

[13] K. Xu, Z. Cheng, C. Y. Wong, and H. K. Tsang, “Tunable integrated variable bit-rate DPSK silicon receiver.,” *Optics letters*, vol. 37, no. 22, pp. 4738–40, Nov. 2012.

[14] R. Claps, D. Dimitropoulos, and B. Jalali, “Stimulated Raman scattering in silicon waveguides,” *Electronics Letters*, vol. 38, no. 22, p. 1352, 2002.

[15] R. Claps, D. Dimitropoulos, V. Raghunathan, Y. Han, and B. Jalali, “Observation of stimulated Raman amplification in silicon waveguides.,” *Optics express*, vol. 11, no. 15, pp. 1731–9, Jul. 2003.

[16] O. Boyraz and B. Jalali, “Demonstration of directly modulated silicon Raman laser,” *Optics Express*, vol. 13, no. 3, p. 796, Oct. 2005.

[17] H. Rong, A. Liu, R. Jones, O. Cohen, D. Hak, R. Nicolaescu, A. Fang, and M. Paniccia, “An all-silicon Raman laser.,” *Nature*, vol. 433, no. 7023, pp. 292–4, Jan. 2005.

[18] H. Rong, Y. Kuo, S. Xu, A. Liu, R. Jones, O. Cohen, and O. Raday, “Monolithic integrated Raman silicon laser,” vol. 14, no. 15, pp. 6705–6712, 2006.

[19] M. a Foster, A. C. Turner, J. E. Sharping, B. S. Schmidt, M. Lipson, and A. L. Gaeta, “Broad-band optical parametric gain on a silicon photonic chip.,” *Nature*, vol. 441, no. 7096, pp. 960–3, Jun. 2006.

[20] A. W. Fang, H. Park, O. Cohen, R. Jones, M. J. Paniccia, and J. E. Bowers, “Electrically pumped hybrid AlGaInAs-silicon evanescent laser.,” *Optics Express*, vol. 14, no. 20, pp. 9203–9210, 2006.

[21] J. E. Bowers, D. Liang, A. W. Fang, H. Park, R. Jones, and M. J. Paniccia, “Hybrid Silicon Lasers: The Final Frontier to Integrated Computing,” *Optics and Photonics News*, vol. 21, no. 5, p. 28, May 2010.

[22] L. C. Kimerling and J. Michel, “Toward a Germanium Laser for Integrated Silicon Photonics,” *IEEE Journal of Selected Topics in Quantum Electronics*, vol. 16, no. 1, pp. 124–131, 2010.

[23] D. Liang and J. E. Bowers, “Recent progress in lasers on silicon,” *Nature Photonics*, vol. 4, no. 8, pp. 511–517, Jul. 2010.

[24] R. E. Camacho-Aguilera, Y. Cai, N. Patel, J. T. Bessette, M. Romagnoli, L. C. Kimerling, and J. Michel, “An electrically pumped germanium laser.,” *Optics express*, vol. 20, no. 10, pp. 11316–20, May 2012.

[25] B. J. Frey, D. B. Leviton, and T. J. Madison, “Temperature-dependent refractive index of silicon and germanium,” in *Proc. SPIE 6273, Optomechanical Technologies for Astronomy*, 2006, vol. 6273, p. 62732J.

[26] A. M. Armani, R. P. Kulkarni, S. E. Fraser, R. C. Flagan, and K. J. Vahala, "Label-free, single-molecule detection with optical microcavities.," *Science (New York, N.Y.)*, vol. 317, no. 5839, pp. 783–7, Aug. 2007.

[27] K. De Vos, I. Bartolozzi, E. Schacht, P. Bienstman, and R. Baets, "Silicon-on-Insulator microring resonator for sensitive and label-free biosensing.," *Optics express*, vol. 15, no. 12, pp. 7610–5, Jun. 2007.

[28] X. Fan, I. M. White, S. I. Shopova, H. Zhu, J. D. Suter, and Y. Sun, "Sensitive optical biosensors for unlabeled targets: a review.," *Analytica chimica acta*, vol. 620, no. 1–2, pp. 8–26, Jul. 2008.

[29] W. Fung and L. J. Guo, "Polymer microring resonators for biochemical sensing applications," *IEEE Journal of Selected Topics in Quantum Electronics*, vol. 12, no. 1, pp. 134–142, Jan. 2006.

[30] D.-K. Qing and I. Yamaguchi, "Analysis of the sensitivity of optical waveguide chemical sensors for TM modes by the group-index method," *Journal of the Optical Society of America B*, vol. 16, no. 9, p. 1359, Sep. 1999.

[31] B. Kuswandi, Nuriman, J. Huskens, and W. Verboom, "Optical sensing systems for microfluidic devices: a review.," *Analytica chimica acta*, vol. 601, no. 2, pp. 141–55, Oct. 2007.

[32] A. Densmore, D. Xu, P. Waldron, S. Janz, P. Cheben, J. Lapointe, A. Delâge, B. Lamontagne, J. H. Schmid, and E. Post, "A Silicon-on-Insulator Photonic Wire Based Evanescent Field Sensor," vol. 18, no. 23, pp. 2520–2522, 2006.

[33] J. T. Robinson, L. Chen, and M. Lipson, "On-chip gas detection in silicon optical microcavities.," *Optics express*, vol. 16, no. 6, pp. 4296–301, Mar. 2008.

[34] M. R. Lee and P. M. Fauchet, "Two-dimensional silicon photonic crystal based biosensing platform for protein detection.," *Optics Express*, vol. 15, no. 8, pp. 4530–4535, 2007.

[35] A. Nitkowski, L. Chen, and M. Lipson, "Cavity-enhanced on-chip absorption spectroscopy using microring resonators.," *Optics express*, vol. 16, no. 16, pp. 11930–6, Aug. 2008.

[36] A. Nitkowski, A. Baeumner, and M. Lipson, "On-chip spectrophotometry for bioanalysis using microring resonators.," *Biomedical optics express*, vol. 2, no. 2, pp. 271–7, Jan. 2011.

[37] D.-X. Xu, M. Vachon, a Densmore, R. Ma, a Delâge, S. Janz, J. Lapointe, Y. Li, G. Lopinski, D. Zhang, Q. Y. Liu, P. Cheben, and J. H. Schmid, "Label-free biosensor array based on silicon-on-insulator ring resonators addressed using a WDM approach.," *Optics letters*, vol. 35, no. 16, pp. 2771–3, Aug. 2010.

[38] B. Thomsen, “24 channel WDM Source.” [Online]. Available: http://bennthomsen.wordpress.com/2012/01/17/optical-networks/.

[39] M. A. Mirza and G. Stewart, “Multiwavelength Operation of Erbium-Doped Fiber Lasers by Periodic Filtering and Phase Modulation,” *Journal of Lightwave Technology*, vol. 27, no. 8, pp. 1034–1044, Apr. 2009.

[40] X. Zhu and R. Jain, “Numerical analysis and experimental results of high-power Er/Pr:ZBLAN 2.7 μm fiber lasers with different pumping designs,” *Applied optics*, vol. 45, no. 27, pp. 7118–7125, 2006.

[41] R. Adar, Y. Shani, C. H. Henry, R. C. Kistler, G. E. Blonder, and N. A. Olsson, “Measurement of very low-loss silica on silicon waveguides with a ring resonator,” *Applied Physics Letters*, vol. 58, no. 5, p. 444, 1991.

[42] T. Baehr-Jones, M. Hochberg, C. Walker, D. Koshinz, W. Krug, and A. Scherer, “Analysis of the tuning sensitivity of silicon-on-insulator optical ring resonators,” *Journal of Lightwave Technology*, vol. 23, no. 12, pp. 4215–4221, Dec. 2005.

[43] J. T. Robinson, K. Preston, O. Painter, and M. Lipson, “First-principle derivation of gain in high-index-contrast waveguides.,” *Optics express*, vol. 16, no. 21, pp. 16659–69, Oct. 2008.

[44] W. Yang, D. B. Conkey, B. Wu, D. Yin, A. R. Hawkins, and H. Schmidt, “Atomic spectroscopy on a chip,” *Nature Photonics*, vol. 1, no. 6, pp. 331–335, Jun. 2007.

[45] N. A. Yebo, P. Lommens, Z. Hens, and R. Baets, “An integrated optic ethanol vapor sensor based on a silicon-on-insulator microring resonator coated with a porous ZnO film.,” *Optics express*, vol. 18, no. 11, pp. 11859–66, May 2010.

[46] C. A. Barrios, “Integrated microring resonator sensor arrays for labs-on-chips.,” *Analytical and bioanalytical chemistry*, vol. 403, no. 6, pp. 1467–75, Jun. 2012.

[47] G. Ning, P. Shum, S. Aditya, D. Liu, Y. Gong, N. Q. Ngo, and M. Tang, “Multiwavelength Raman fiber lasers with equalized peak power using a sampled chirped fiber Bragg grating,” *Applied Physics B*, vol. 83, no. 2, pp. 249–253, Mar. 2006.

[48] Z. Luo, W.-D. Zhong, Z. Cai, C. Ye, and Y. J. Wen, “High-performance SOA-based multiwavelength fiber lasers incorporating a novel double-pass waveguide-based MZI,” *Applied Physics B*, vol. 96, no. 1, pp. 29–38, May 2009.

[49] R. Paschotta, *Encyclopedia of Laser Physics and Technology*, 1st ed. Berlin: Wiley-VCH, 2008, p. 844.

[50] a. M. Ramzia Salem, M. H. Al-Mansoori, H. Hizam, S. B. Mohd Noor, M. H. Abu Bakar, and M. a. Mahdi, "Multiwavelength L-band fiber laser with bismuth-oxide EDF and photonic crystal fiber," *Applied Physics B*, vol. 103, no. 2, pp. 363–368, Nov. 2010.

[51] M. S. Demokan and H. Y. Tam, "Stable and broad bandwidth multiwavelength fiber ring laser incorporating a highly nonlinear photonic crystal fiber," *IEEE Photonics Technology Letters*, vol. 17, no. 12, pp. 2535–2537, Dec. 2005.

[52] X. Liu and C. Lu, "Self-stabilizing effect of four-wave mixing and its applications on multiwavelength erbium-doped fiber lasers," *IEEE Photonics Technology Letters*, vol. 17, no. 12, pp. 2541–2543, Dec. 2005.

[53] S. Pan, C. Lou, and Y. Gao, "Multiwavelength erbium-doped fiber laser based on inhomogeneous loss mechanism by use of a highly nonlinear fiber and a Fabry-Perot filter.," *Optics express*, vol. 14, no. 3, pp. 1113–8, Feb. 2006.

[54] Y.-G. Han, T. V. A. Tran, and S. B. Lee, "Wavelength-spacing tunable multiwavelength erbium-doped fiber laser based on four-wave mixing of dispersion-shifted fiber.," *Optics letters*, vol. 31, no. 6, pp. 697–9, Mar. 2006.

[55] Z. Luo, M. Zhou, Z. Cai, C. Ye, J. Weng, G. Huang, and H. Xu, "Graphene-Assisted Multiwavelength Erbium-Doped Fiber Ring Laser," *IEEE Photonics Technology Letters*, vol. 23, no. 8, pp. 501–503, Apr. 2011.

[56] J. Leuthold, C. Koos, and W. Freude, "Nonlinear silicon photonics," *Nature Photonics*, vol. 4, no. 8, pp. 535–544, Jul. 2010.

[57] S. Afshar Vahid and T. M. Monro, "A full vectorial model for pulse propagation in emerging waveguides with subwavelength structures part I: Kerr nonlinearity," *Optics Express*, vol. 17, no. 4, p. 2298, Feb. 2009.

[58] Y. R. Shen, *The Principles of Nonlinear Optics*, 1st ed. Wiley-Interscience, 1984, p. 576.

[59] R. W. Boyd, *Nonlinear Optics, Third Edition*, 3rd ed. Academic Press, 2008, p. 640.

[60] Q. Lin, O. J. Painter, and G. P. Agrawal, "Nonlinear optical phenomena in silicon waveguides: modeling and applications.," *Optics express*, vol. 15, no. 25, pp. 16604–44, Dec. 2007.

[61] R. S. Jacobsen, K. N. Andersen, P. I. Borel, J. Fage-Pedersen, L. H. Frandsen, O. Hansen, M. Kristensen, A. V Lavrinenko, G. Moulin, H. Ou, C. Peucheret, B. Zsigri, and A. Bjarklev, "Strained silicon as a new electro-optic material," *Nature*, vol. 441, no. 7090, pp. 199–202, 2006.

[62] J. M. Dudley and S. Coen, “Supercontinuum generation in photonic crystal fiber,” *Reviews of Modern Physics*, vol. 78, no. 4, pp. 1135–1184, Oct. 2006.

[63] B. Corcoran, C. Monat, C. Grillet, D. J. Moss, B. J. Eggleton, T. P. White, L. O. Faolain, and T. F. Krauss, “Green light emission in silicon through slow-light enhanced third-harmonic generation in photonic- crystal waveguides,” *Nature Photonics*, vol. 3, no. April, pp. 206–210, 2009.

[64] B. Jalali, V. Raghunathan, D. Dimitropoulos, and O. Boyraz, “Raman-based silicon photonics,” *IEEE Journal of Selected Topics in Quantum Electronics*, vol. 12, no. 3, pp. 412–421, 2006.

[65] G. Agrawal, *Nonlinear Fiber Optics*, 5th ed. Academic Press, 2012.

[66] M. A. Foster, A. C. Turner, R. Salem, M. Lipson, and A. L. Gaeta, “Broad-band continuous-wave parametric wavelength conversion in silicon nanowaveguides,” *Optics Express*, vol. 15, no. 20, p. 12949, 2007.

[67] P. Cheben, R. Soref, D. Lockwood, and G. Reed, “Silicon Photonics,” *Advances in Optical Technologies*, vol. 2008, no. 14, pp. 1–2, 2008.

[68] D. Taillaert, W. Bogaerts, P. Bienstman, T. F. Krauss, P. Van Daele, I. Moerman, S. Verstuyft, K. De Mesel, and R. Baets, “An out-of-plane grating coupler for efficient butt-coupling between compact planar waveguides and single-mode fibers,” *IEEE Journal of Quantum Electronics*, vol. 38, no. 7, pp. 949–955, Jul. 2002.

[69] W. Bogaerts, S. K. Selvaraja, and P. Dumon, “Technology Paper IMEC_193_01,” *ePIXfab*, 2008. [Online]. Available: http://www.epixfab.eu/.

[70] M. P. Fok, C. Shu, and D. J. Blumenthal, “Dual-pump four-wave mixing in bismuth-oxide highly nonlinear fiber for wide-band DPSK wavelength conversion,” in *National Fiber Optic Engineers Conference*, 2007, no. Di, p. JThA52.

[71] T. K. Liang and H. K. Tsang, “Role of free carriers from two-photon absorption in Raman amplification in silicon-on-insulator waveguides,” *Applied Physics Letters*, vol. 84, no. 15, p. 2745, 2004.

[72] T.-Y. Liow, K.-W. Ang, Q. Fang, J.-F. Song, Y.-Z. Xiong, M.-B. Yu, G.-Q. Lo, and D.-L. Kwong, “Silicon Modulators and Germanium Photodetectors on SOI: Monolithic Integration, Compatibility, and Performance Optimization,” *IEEE Journal of Selected Topics in Quantum Electronics*, vol. 16, no. 1, pp. 307–315, 2010.

[73] S. Faralli, K. N. Nguyen, J. D. Peters, D. T. Spencer, D. J. Blumenthal, and J. E. Bowers, “Integrated hybrid Si/InGaAs 50 Gb/s DQPSK receiver,” *Optics Express*, vol. 20, no. 18, p. 19726, Aug. 2012.

[74] C. Kopp, S. Bernabé, B. B. Bakir, J. Fedeli, R. Orobtchouk, F. Schrank, H. Porte, L. Zimmermann, and T. Tekin, "Silicon Photonic Circuits: On-CMOS Integration, Fiber Optical Coupling, and Packaging," *IEEE Journal of Selected Topics in Quantum Electronics*, vol. 17, no. 3, pp. 498–509, May 2011.

[75] A. C. Turner, C. Manolatou, B. S. Schmidt, M. Lipson, M. a Foster, J. E. Sharping, and A. L. Gaeta, "Tailored anomalous group-velocity dispersion in silicon channel waveguides.," *Optics express*, vol. 14, no. 10, pp. 4357–62, May 2006.

[76] X. Chen, C. Li, C. K. Y. Fung, S. M. G. Lo, and H. K. Tsang, "Apodized waveguide grating couplers for efficient coupling to optical fibers," *Photonics Technology …*, vol. 22, no. 15, pp. 1156–1158, 2010.

[77] Z. Xiao, F. Luan, T.-Y. Liow, J. Zhang, and P. Shum, "Design for broadband high-efficiency grating couplers," *Optics Letters*, vol. 37, no. 4, p. 530, Feb. 2012.

[78] J. Schröder, D. Alasia, T. Sylvestre, and S. Coen, "Dynamics of an ultrahigh-repetition-rate passively mode-locked Raman fiber laser," *Journal of the Optical Society of America B*, vol. 25, no. 7, p. 1178, Jun. 2008.

[79] E. Yoshida and M. Nakazawa, "Low-threshold 115-GHz continuous-wave modulational-instability erbium-doped fiber laser," *Optics letters*, vol. 22, no. 18, pp. 1409–1411, 1997.

[80] M. Quiroga-Teixeiro, C. B. Clausen, M. P. Sørensen, P. L. Christiansen, and P. a. Andrekson, "Passive mode locking by dissipative four-wave mixing," *Journal of the Optical Society of America B*, vol. 15, no. 4, p. 1315, Apr. 1998.

[81] M. Peccianti, A. Pasquazi, Y. Park, B. E. Little, S. T. Chu, D. J. Moss, and R. Morandotti, "Demonstration of a stable ultrafast laser based on a nonlinear microcavity," *Nature communications*, vol. 3, p. 765, Jan. 2012.

[82] S. J. B. Yoo, "Integrated Photonic-Electronic Technologies for Next Generation Data Centers and the Future Internet," in *Photonics in Switching 2012*, 2012, p. Fr–S38–I16.

[83] K. Xu, J. Y. J. Sung, L. Yang, Y. Chen, Z. Cheng, C. W. Chow, C. H. Yeh, and H. K. Tsang, "Experimental Demonstration of Multi-level Modulation on OFDM Signals Using Integrated Silicon Modulators," in *Optical Fiber Communication Conference/National Fiber Optic Engineers Conference 2013*, 2013, p. OW1G.5.

[84] T. J. Kippenberg, R. Holzwarth, and S. a Diddams, "Microresonator-based optical frequency combs.," *Science (New York, N.Y.)*, vol. 332, no. 6029, pp. 555–9, Apr. 2011.

[85] U. Keller, “Recent developments in compact ultrafast lasers.,” *Nature*, vol. 424, no. 6950, pp. 831–8, Aug. 2003.

[86] H. A. Haus, “Mode-locking of lasers,” *IEEE Journal of Selected Topics in Quantum Electronics*, vol. 6, no. 6, pp. 1173–1185, 2000.

[87] T. Habruseva, S. O’Donoghue, N. Rebrova, F. Kéfélian, S. P. Hegarty, and G. Huyet, “Optical linewidth of a passively mode-locked semiconductor laser.,” *Optics letters*, vol. 34, no. 21, pp. 3307–9, Nov. 2009.

[88] Z. Jiao, J. Liu, Z. Lu, X. Zhang, P. J. Poole, P. J. Barrios, and D. Poitras, “A C-Band InAs/InP Quantum Dot Semiconductor Mode-Locked Laser Emitting 403-GHz Repetition Rate Pulses,” *Photonics Technology Letters, IEEE*, vol. 23, no. 9, pp. 543–545, 2011.

[89] T. Pfeiffer and G. Veith, “40 GHz pulse generation using a widely tunable all-polarisation preserving erbium fibre ring laser,” *Electronics Letters*, vol. 29, no. 21, p. 1849, 1993.

[90] T. Sylvestre, S. Coen, O. Deparis, P. Emplit, and M. Haelterman, “Demonstration of passive modelocking through dissipative four-wave mixing in fibre laser,” *Electronics Letters*, vol. 37, no. 14, pp. 881–2, 2001.

[91] M. Nakazawa, K. Tamura, and E. Yoshida, “Supermode noise suppression in a harmonically modelocked fibre laser by selfphase modulation and spectral filtering,” *Electronics Letters*, vol. 32, no. 5, pp. 461–463, 1996.

[92] O. Pottiez, O. Deparis, M. Haelterman, R. Kiyan, P. Emplit, P. Megret, and M. Blondel, “Experimental study of supermode noise of harmonically mode-locked erbium-doped fibre lasers with composite cavity,” *Optics Communications*, vol. 202, no. 1–3, pp. 161–167, 2002.

[93] K. K. Gupta, N. Onodera, M. Hyodo, M. Watanabe, and J. Ravikumar, *Evaluation of amplitude-stabilized optical pulse trains from rational harmonically mode-locked fiber ring lasers*, vol. 22, no. 8. 2004, pp. 1935–1945.

[94] G.-R. Lin, M.-C. Wu, and Y.-C. Chang, “Phase noise and supermode suppression in harmonic mode-locked erbium-doped fiber laser with a semiconductor optical amplifier based high-pass filter,” *Optics Letters*, vol. 30, no. 14, pp. 1834–1836, 2005.

[95] A. Yariv, “Universal relations for coupling of optical power between microresonators and dielectric waveguides,” *Electronics Letters*, vol. 36, no. 4, pp. 321–2, 2000.

[96] A. E. Siegman, *Lasers*, 1st ed. Sausalito, CA: University Science Books, 1986.

[97] M. Peccianti, A. Pasquazi, Y. Park, B. Little, S. T. Chu, D. J. Moss, and R. Morandotti, “Dissipative Four Wave Mixing Sub-ps Laser Based on a CMOS Compatible Integrated Microring Resonator,” *Latin America Optics and Photonics Conference*, no. c, p. TuD4, 2010.

[98] A. Pasquazi, M. Peccianti, Y. Park, B. E. Little, S. T. Chu, D. J. Moss, and R. Morandotti, “Sub-ps Laser Based on a CMOS Compatible Integrated Microring Resonator,” *Optical Fiber Communication Conference/National Fiber Optic Engineers Conference 2011*, no. c, p. OThU2, 2011.

[99] A. Griffith, J. Cardenas, C. B. Poitras, and M. Lipson, “High quality factor and high confinement silicon resonators using etchless process.,” *Optics express*, vol. 20, no. 19, pp. 21341–5, Sep. 2012.

[100] A. G. Rozhin, Y. Sakakibara, S. Namiki, M. Tokumoto, H. Kataura, and Y. Achiba, “Sub-200-fs pulsed erbium-doped fiber laser using a carbon nanotube-polyvinylalcohol mode locker,” *Applied Physics Letters*, vol. 88, no. 5, p. 051118, Feb. 2006.

[101] V. Scardaci, Z. Sun, F. Wang, A. G. Rozhin, T. Hasan, F. Hennrich, I. H. White, W. I. Milne, and A. C. Ferrari, “Carbon Nanotube Polycarbonate Composites for Ultrafast Lasers,” *Advanced Materials*, vol. 20, no. 21, pp. 4040–4043, Nov. 2008.

[102] F. Wang, A. G. Rozhin, V. Scardaci, Z. Sun, F. Hennrich, I. H. White, W. I. Milne, and A. C. Ferrari, “Wideband-tuneable, nanotube mode-locked, fibre laser.,” *Nature nanotechnology*, vol. 3, no. 12, pp. 738–42, Dec. 2008.

[103] Z. Sun, A. G. Rozhin, F. Wang, T. Hasan, D. Popa, W. O’Neill, and A. C. Ferrari, “A compact, high power, ultrafast laser mode-locked by carbon nanotubes,” *Applied Physics Letters*, vol. 95, no. 25, p. 253102, Dec. 2009.

[104] T. Hasan, Z. Sun, F. Wang, F. Bonaccorso, P. H. Tan, A. G. Rozhin, and A. C. Ferrari, “Nanotube-€ “Polymer Composites for Ultrafast Photonics,” *Advanced Materials*, vol. 21, no. 38â□“39, pp. 3874–3899, Oct. 2009.

[105] Q. Bao, H. Zhang, Y. Wang, Z. Ni, Y. Yan, Z. X. Shen, K. P. Loh, and D. Y. Tang, “Atomic-Layer Graphene as a Saturable Absorber for Ultrafast Pulsed Lasers,” *Advanced Functional Materials*, vol. 19, no. 19, pp. 3077–3083, Oct. 2009.

[106] H. Zhang, D. Y. Tang, L. M. Zhao, Q. L. Bao, and K. P. Loh, “Large energy mode locking of an erbium-doped fiber laser with atomic layer graphene,” *Optics express*, vol. 17, no. 20, pp. 17630–5, 2009.

[107] Z. Sun, T. Hasan, F. Torrisi, D. Popa, G. Privitera, F. Wang, F. Bonaccorso, D. M. Basko, and A. C. Ferrari, “Graphene mode-locked ultrafast laser,” *ACS nano*, vol. 4, no. 2, pp. 803–10, Feb. 2010.

[108] Y.-W. Song, S.-Y. Jang, W.-S. Han, and M.-K. Bae, “Graphene mode-lockers for fiber lasers functioned with evanescent field interaction,” *Applied Physics Letters*, vol. 96, no. 5, p. 051122, 2010.

[109] A. K. Geim and K. S. Novoselov, “The rise of graphene,” *Nature Materials*, vol. 6, no. 3, pp. 183–191, Mar. 2007.

[110] A. K. Geim, “Graphene: status and prospects.,” *Science (New York, N.Y.)*, vol. 324, no. 5934, pp. 1530–4, Jun. 2009.

[111] T. Mueller, F. Xia, and P. Avouris, “Graphene photodetectors for high-speed optical communications,” *Nature Photonics*, vol. 4, no. March, pp. 297–301, 2010.

[112] M. Liu, X. Yin, E. Ulin-Avila, B. Geng, T. Zentgraf, L. Ju, F. Wang, and X. Zhang, “A graphene-based broadband optical modulator.,” *Nature*, vol. 474, no. 7349, pp. 64–7, Jun. 2011.

[113] K. Kim, J.-Y. Choi, T. Kim, S.-H. Cho, and H.-J. Chung, “A role for graphene in silicon-based semiconductor devices.,” *Nature*, vol. 479, no. 7373, pp. 338–44, Nov. 2011.

[114] T. Gu, N. Petrone, J. F. McMillan, A. van der Zande, M. Yu, G. Q. Lo, D. L. Kwong, J. Hone, and C. W. Wong, “Regenerative oscillation and four-wave mixing in graphene optoelectronics,” *Nature Photonics*, vol. 6, pp. 554–559, 2012.

[115] H. Li, Y. Anugrah, S. J. Koester, and M. Li, “Optical absorption in graphene integrated on silicon waveguides,” *Applied Physics Letters*, vol. 101, no. 11, p. 111110, 2012.

[116] J. Slonczewski and P. Weiss, “Band Structure of Graphite,” *Physical Review*, vol. 109, no. 2, pp. 272–279, Jan. 1958.

[117] R. Saito and H. Kataura, “Optical Properties and Raman Spectroscopy of Carbon Nanotubes,” in in *Carbon Nanotubes, Topics in Applied Physics Volume 80*, vol. 80, M. S. Dresselhaus, G. Dresselhaus, and P. Avouris, Eds. Berlin, Heidelberg: Springer Berlin Heidelberg, 2001, pp. 213–247.

[118] A. H. Castro Neto, N. M. R. Peres, K. S. Novoselov, and a. K. Geim, “The electronic properties of graphene,” *Reviews of Modern Physics*, vol. 81, no. 1, pp. 109–162, Jan. 2009.

[119] C. Y. Wong, “Electronic Characterization of Individual Single-walled Carbon Nanotubes,” The University of Hong Kong, 2007.

[120] Y. Zhang, Y.-W. Tan, H. L. Stormer, and P. Kim, “Experimental observation of the quantum Hall effect and Berry’s phase in graphene.,” *Nature*, vol. 438, no. 7065, pp. 201–4, Nov. 2005.

[121] K. S. Novoselov, A. K. Geim, S. V Morozov, D. Jiang, M. I. Katsnelson, I. V Grigorieva, S. V Dubonos, and A. A. Firsov, "Two-dimensional gas of massless Dirac fermions in graphene.," *Nature*, vol. 438, no. 7065, pp. 197–200, Nov. 2005.

[122] X. Du, I. Skachko, A. Barker, and E. Y. Andrei, "Approaching ballistic transport in suspended graphene.," *Nature nanotechnology*, vol. 3, no. 8, pp. 491–5, Aug. 2008.

[123] K. I. Bolotin, K. J. Sikes, Z. Jiang, M. Klima, G. Fudenberg, J. Hone, P. Kim, and H. L. Stormer, "Ultrahigh electron mobility in suspended graphene," *Solid State Communications*, vol. 146, no. 9–10, pp. 351–355, Jun. 2008.

[124] O. Klein, "Die Reflexion von Elektronen an einem Potentialsprung nach der relativistischen Dynamik von Dirac," *Zeitschrift für Physik*, vol. 53, no. 3–4, pp. 157–165, Mar. 1929.

[125] A. F. Young and P. Kim, "Quantum interference and Klein tunnelling in graphene heterojunctions," *Nature Physics*, vol. 5, no. 3, pp. 222–226, Feb. 2009.

[126] Z. Q. Li, E. A. Henriksen, Z. Jiang, Z. Hao, M. C. Martin, P. Kim, H. L. Stormer, and D. N. Basov, "Dirac charge dynamics in graphene by infrared spectroscopy," *Nature Physics*, vol. 4, no. 7, pp. 532–535, Jun. 2008.

[127] F. Wang, Y. Zhang, C. Tian, C. Girit, A. Zettl, M. Crommie, and Y. R. Shen, "Gate-variable optical transitions in graphene.," *Science (New York, N.Y.)*, vol. 320, no. 5873, pp. 206–9, Apr. 2008.

[128] K. F. Mak, M. Y. Sfeir, Y. Wu, C. H. Lui, J. a. Misewich, and T. F. Heinz, "Measurement of the Optical Conductivity of Graphene," *Physical Review Letters*, vol. 101, no. 19, p. 196405, Nov. 2008.

[129] G. Moos, C. Gahl, R. Fasel, M. Wolf, and T. Hertel, "Anisotropy of Quasiparticle Lifetimes and the Role of Disorder in Graphite from Ultrafast Time-Resolved Photoemission Spectroscopy," *Physical Review Letters*, vol. 87, no. 26, p. 267402, Dec. 2001.

[130] T. Kampfrath, L. Perfetti, F. Schapper, C. Frischkorn, and M. Wolf, "Strongly Coupled Optical Phonons in the Ultrafast Dynamics of the Electronic Energy and Current Relaxation in Graphite," *Physical Review Letters*, vol. 95, no. 18, p. 187403, Oct. 2005.

[131] P. A. George, J. Strait, J. Dawlaty, S. Shivaraman, M. Chandrashekhar, F. Rana, and M. G. Spencer, "Ultrafast optical-pump terahertz-probe spectroscopy of the carrier relaxation and recombination dynamics in epitaxial graphene.," *Nano letters*, vol. 8, no. 12, pp. 4248–51, Dec. 2008.

[132] J. M. Dawlaty, S. Shivaraman, M. Chandrashekhar, F. Rana, and M. G. Spencer, “Measurement of ultrafast carrier dynamics in epitaxial graphene,” *Applied Physics Letters*, vol. 92, no. 4, p. 042116, Jan. 2008.

[133] R. N. Zitter, “SATURATED OPTICAL ABSORPTION THROUGH BAND FILLING IN SEMICONDUCTORS,” *Applied Physics Letters*, vol. 14, no. 2, p. 73, Jan. 1969.

[134] A. Komarov, H. Leblond, and F. Sanchez, “Passive harmonic mode-locking in a fiber laser with nonlinear polarization rotation,” *Optics Communications*, vol. 267, no. 1, pp. 162–169, Nov. 2006.

[135] Z. Cheng, X. Chen, C. Y. Wong, K. Xu, and H. K. Tsang, “Mid-infrared Suspended Membrane Waveguide and Ring Resonator on Silicon-on-Insulator,” *IEEE Photonics Journal*, vol. 4, no. 5, pp. 1510–1519, Oct. 2012.

[136] Z. Cheng, X. Chen, C. Y. Wong, K. Xu, and H. K. Tsang, “Apodized focusing subwavelength grating couplers for suspended membrane waveguides,” *Applied Physics Letters*, vol. 101, no. 10, p. 101104, 2012.

[137] H. Zhang, D. Y. Tang, L. M. Zhao, Q. L. Bao, K. P. Loh, B. Lin, and S. C. Tjin, “Compact graphene mode-locked wavelength-tunable erbium-doped fiber lasers: from all anomalous dispersion to all normal dispersion,” *Laser Physics Letters*, vol. 7, no. 8, pp. 591–596, Jun. 2010.

[138] M. Ebrahim-Zadeh and I. T. Sorokina, Eds., *Mid-Infrared Coherent Sources and Applications*, 2008th ed. Springer, 2007.

[139] P. Griffiths and J. A. De Haseth, *Fourier Transform Infrared Spectrometry*, 2nd ed. Wiley-Interscience, 2007.

[140] R. a Soref, S. J. Emelett, and W. R. Buchwald, “Silicon waveguided components for the long-wave infrared region,” *Journal of Optics A: Pure and Applied Optics*, vol. 8, no. 10, pp. 840–848, Oct. 2006.

[141] R. Soref, “Mid-infrared photonics in silicon and germanium,” *Nature Photonics*, vol. 4, no. 8, pp. 495–497, Aug. 2010.

[142] R. Soref, “Group IV photonics for the mid infrared,” in *SPIE OPTO*, 2013, pp. 862902–862902–15.

[143] V. Raghunathan, D. Borlaug, R. R. Rice, and B. Jalali, “Demonstration of a Mid-infrared silicon Raman amplifier.,” *Optics express*, vol. 15, no. 22, pp. 14355–62, Oct. 2007.

[144] B. Jalali, V. Raghunathan, R. Shori, S. Fathpour, D. Dimitropoulos, and O. M. Stafsudd, “Prospects for silicon mid-IR Raman lasers,” *IEEE Journal of Selected Topics in Quantum Electronics*, vol. 12, no. 6, pp. 1618–1627, 2006.

[145] X. Liu, R. M. Osgood Jr, Y. A. Vlasov, and W. M. J. Green, “Mid-infrared optical parametric amplifier using silicon nanophotonic waveguides,” *Nature Photonics*, vol. 4, no. 8, pp. 2–5, 2010.

[146] B. Kuyken, X. Liu, G. Roelkens, R. Baets, R. M. Osgood, and W. M. J. Green, “50 dB parametric on-chip gain in silicon photonic wires,” *Optics Letters*, vol. 36, no. 22, pp. 4401–4403, 2011.

[147] R. Shankar, R. Leijssen, I. Bulu, and M. Lončar, “Mid-infrared photonic crystal cavities in silicon,” *Optics express*, vol. 19, no. 6, pp. 5579–86, Mar. 2011.

[148] G. Z. Mashanovich, M. M. Milošević, M. Nedeljkovic, N. Owens, B. Xiong, E. J. Teo, and Y. Hu, “Low loss silicon waveguides for the mid-infrared,” *Optics express*, vol. 19, no. 8, pp. 7112–9, Apr. 2011.

[149] X. Zhu and N. Peyghambarian, “High-Power ZBLAN Glass Fiber Lasers: Review and Prospect,” *Advances in OptoElectronics*, vol. 2010, pp. 1–23, 2010.

[150] T. Baehr-Jones, A. Spott, R. Ilic, A. Spott, B. Penkov, W. Asher, and M. Hochberg, “Silicon-on-sapphire integrated waveguides for the mid-infrared.,” *Optics Express*, vol. 18, no. 12, pp. 12127–35, Jun. 2010.

[151] F. Li, S. D. Jackson, C. Grillet, E. Magi, D. Hudson, S. J. Madden, Y. Moghe, C. O’Brien, A. Read, S. G. Duvall, P. Atanackovic, B. J. Eggleton, and D. J. Moss, “Low propagation loss silicon-on-sapphire waveguides for the mid-infrared,” *Optics express*, vol. 19, no. 16, pp. 15212–20, Aug. 2011.

[152] A. Spott, Y. Liu, T. Baehr-Jones, R. Ilic, and M. Hochberg, “Silicon waveguides and ring resonators at 5.5 μm,” *Applied Physics Letters*, vol. 97, no. 21, p. 213501, 2010.

[153] G. Cocorullo and I. Rendina, “Thermo-optical modulation at 1.5μm in silicon etalon,” *Electronics Letters*, vol. 28, no. 1, pp. 83–85, 1992.

[154] D.-X. Xu, M. Vachon, a Densmore, R. Ma, S. Janz, a Delâge, J. Lapointe, P. Cheben, J. H. Schmid, E. Post, S. Messaoudène, and J.-M. Fédéli, “Real-time cancellation of temperature induced resonance shifts in SOI wire waveguide ring resonator label-free biosensor arrays.,” *Optics express*, vol. 18, no. 22, pp. 22867–79, Oct. 2010.

[155] N. Carlie, J. D. Musgraves, B. Zdyrko, I. Luzinov, J. Hu, V. Singh, A. Agarwal, L. C. Kimerling, A. Canciamilla, F. Morichetti, A. Melloni, and K. Richardson, “Integrated chalcogenide waveguide resonators for mid-IR sensing: leveraging material properties to meet fabrication challenges.,” *Optics express*, vol. 18, no. 25, pp. 26728–43, Dec. 2010.

[156] “The HITRAN Database.” [Online]. Available: http://www.cfa.harvard.edu/hitran/.

[157] G. J. Veldhuis, O. Parriaux, H. J. W. M. Hoekstra, and P. V. Lambeck, “Sensitivity enhancement in evanescent optical waveguide sensors,” *Journal of Lightwave Technology*, vol. 18, no. 5, pp. 677–682, May 2000.

[158] V. R. Almeida and M. Lipson, “Optical bistability on a silicon chip,” *Optics Letters*, vol. 29, no. 20, p. 2387, Oct. 2004.

[159] Q. Xu and M. Lipson, “Carrier-induced optical bistability in silicon ring resonators.,” *Optics letters*, vol. 31, no. 3, pp. 341–3, Feb. 2006.

[160] S. Tokita, M. Murakami, S. Shimizu, M. Hashida, and S. Sakabe, “Liquid-cooled 24 W mid-infrared Er:ZBLAN fiber laser.,” *Optics letters*, vol. 34, no. 20, pp. 3062–4, Oct. 2009.

[161] M. Pollnau and S. D. Jackson, “Energy recycling versus lifetime quenching in erbium-doped 3-μm fiber lasers,” *IEEE Journal of Quantum Electronics*, vol. 38, no. 2, pp. 162–169, 2002.

[162] M. Bass, C. DeCusatis, J. Enoch, V. Lakshminarayanan, G. Li, C. MacDonald, V. Mahajan, and E. Van Stryland, *Handbook of Optics, Third Edition Volume IV: Optical Properties of Materials, Nonlinear Optics, Quantum Optics*, 3rd ed. McGraw-Hill Professional, 2009, p. 1152.

[163] Z. Cheng, X. Chen, C. Y. Wong, C. K. Y. Fung, Y. M. Chen, and H. K. Tsang, “Mid-Infrared Grating Couplers for Silicon-on-Sapphire Waveguides,” *IEEE Photonics Journal*, vol. 4, no. 1, pp. 104–113, Feb. 2012.

[164] Y. Okada and Y. Tokumaru, “Precise determination of lattice parameter and thermal expansion coefficient of silicon between 300 and 1500 K,” *Journal of Applied Physics*, vol. 56, no. 2, p. 314, 1984.

[165] T. J. Johnson, M. Borselli, and O. Painter, “Self-induced optical modulation of the transmission through a high-Q silicon microdisk resonator.,” *Optics express*, vol. 14, no. 2, pp. 817–31, Jan. 2006.

[166] D. Yang, M. E. Thomas, and S. G. Kaplan, “Measurement of the infrared refractive index of sapphire as function of temperature,” in *Proc. SPIE 4375, Window and Dome Technologies and Materials VII*, 2001, vol. 4375, pp. 53–63.

[167] M. Pokrass, Z. Burshtein, and R. Gvishi, “Thermo-optic coefficient in some hybrid organic/inorganic fast sol–gel glasses,” *Optical Materials*, vol. 32, no. 9, pp. 975–981, Jul. 2010.

[168] J. D. B. Bradley, M. Costa e Silva, M. Gay, L. Bramerie, A. Driessen, K. Wörhoff, J.-C. Simon, and M. Pollnau, “170 Gbit/s transmission in an erbium-

doped waveguide amplifier on silicon.," *Optics Express*, vol. 17, no. 24, pp. 22201–8, Nov. 2009.

[169] L. Agazzi, J. D. B. Bradley, M. Dijkstra, F. Ay, G. Roelkens, R. Baets, K. Wörhoff, and M. Pollnau, "Monolithic integration of erbium-doped amplifiers with silicon-on-insulator waveguides.," *Optics Express*, vol. 18, no. 26, pp. 27703–11, Dec. 2010.

[170] J. Cardenas, C. B. Poitras, J. T. Robinson, K. Preston, L. Chen, and M. Lipson, "Low loss etchless silicon photonic waveguides.," *Optics express*, vol. 17, no. 6, pp. 4752–7, Mar. 2009.

[171] C. Koos, P. Vorreau, T. Vallaitis, P. Dumon, W. Bogaerts, R. Baets, B. Esembeson, I. Biaggio, T. Michinobu, F. Diederich, W. Freude, and J. Leuthold, "All-optical high-speed signal processing with silicon-organic hybrid slot waveguides," *Nature Photonics*, vol. 3, pp. 216–219, 2009.

[172] K. Mak, C. Lui, J. Shan, and T. Heinz, "Observation of an Electric-Field-Induced Band Gap in Bilayer Graphene by Infrared Spectroscopy," *Physical Review Letters*, vol. 102, no. 25, p. 256405, Jun. 2009.

[173] L. E. Nelson, D. J. Jones, K. Tamura, H. a. Haus, and E. P. Ippen, "Ultrashort-pulse fiber ring lasers," *Applied Physics B: Lasers and Optics*, vol. 65, no. 2, pp. 277–294, Aug. 1997.

[174] L. Yin, J. Zhang, P. M. Fauchet, and G. P. Agrawal, "Optical switching using nonlinear polarization rotation inside silicon waveguides," *Optics letters*, vol. 34, no. 4, pp. 476–478, 2009.

[175] J. Y. Lee, L. Yin, G. P. Agrawal, and P. M. Fauchet, "Ultrafast optical switching based on nonlinear polarization rotation in silicon waveguides.," *Optics express*, vol. 18, no. 11, pp. 11514–23, May 2010.

[176] D. Taillaert, H. Chong, P. I. Borel, L. H. Frandsen, R. M. De La Rue, and R. Baets, "A compact two-dimensional grating coupler used as a polarization splitter," *IEEE Photonics Technology Letters*, vol. 15, no. 9, pp. 1249–1251, 2003.

[177] W. Bogaerts, D. Taillaert, P. Dumon, D. Van Thourhout, R. Baets, and E. Pluk, "A polarization-diversity wavelength duplexer circuit in silicon-on-insulator photonic wires," *Optics Express*, vol. 15, no. 4, p. 1567, Feb. 2007.

[178] F. Van Laere, W. Bogaerts, P. Dumon, G. Roelkens, D. Van Thourhout, and R. Baets, "Focusing Polarization Diversity Grating Couplers in Silicon-on-Insulator," *Lightwave Technology, Journal of*, vol. 27, no. 5, pp. 612–618, 2009.

[179] Z. Cheng, X. Chen, C. Y. Wong, K. Xu, and H. K. Tsang, “Broadband focusing grating couplers for suspended-membrane waveguides.,” *Optics letters*, vol. 37, no. 24, pp. 5181–3, Dec. 2012.

Appendix A: List of abbreviations

2D	**Two d**imensional
ASE	**A**mplified **s**pontaneous **e**mission
AWG	**A**rrayed **w**aveguide **g**rating
BOX	**B**uried **ox**ide layer for SOI wafers
C-band	**C**ommunication **band**
CMOS	**C**omplementary **m**etal–**o**xide–**s**emiconductor
CVD	**C**hemical **v**apor **d**eposition
DOS	**D**ensity **o**f **s**tates
DSF	**D**ispersion **s**hifted **f**iber
EBL	**E**lectron **b**eam **l**ithography
EDF	**E**rbium-**d**oped **f**iber
EDFA	**EDF a**mplifier
EDFL	**EDF l**aser
FCA	**F**ree-**c**arrier **a**bsorption
FCI	**F**ree-**c**arrier **i**ndex
FEM	**F**inite **e**lement **m**ethod

F-P filter	**F**abry-**P**érot comb **filter**
FSR	**F**ree-**s**pectral-**r**ange
FDTD	**F**inite-**d**ifference **t**ime-**d**omain
FWHM	**F**ull-**w**idth-**h**alf-**m**aximum
FWM	**F**our-**w**ave **m**ixing
HF	**H**ydro**f**luoric acid
HNLF	**H**ighly **n**on**l**inear **f**iber
HWHM	**H**alf-**w**idth-**h**alf-**m**aximum
ICP/RIE	**I**nductively **c**oupled **p**lasma / **r**eactive **i**on **e**tching
Mid-IR	**Mid-i**nfra**r**ed
MZI	**M**ach-**Z**ehnder **i**nterferometer
NA	**N**umerical **a**perture
Near-IR	**Near-i**nfra**r**ed
OC	**O**ptical **c**oupler
OH	**H**ydr**o**xyl
OSA	**O**ptical **s**pectrum **a**nalyzer
PCF	**P**hotonic **c**rystal **f**iber

PC	**P**olarization **c**ontroller
PECVD	**P**lasma-**e**nhanced **CVD**
PIC	**P**hotonic **i**ntegrated **c**ircuit
Q	**Q**uality factor
QCL	**Q**uantum **c**ascade **l**aser
SEM	**S**canning **e**lectron **m**icroscope
SESAM	**S**emiconductor **s**aturable **a**bsorber **m**irror
SMF	**S**ingle **m**ode **f**iber
SMW	**S**uspended **m**embrane **w**aveguide
SOA	**S**emiconductor **o**ptical **a**mplifier
SOI	**S**ilicon-**o**n-**i**nsulator
SOS	**S**ilicon-**o**n-**s**apphire
SPM	**S**elf **p**hase **m**odulation
TB	**T**ight **b**inding
TE	**T**ransverse **e**lectric
TEC	**T**hermo**e**lectric **c**ooling
THG	**T**hird **h**armonic **g**eneration

TM **T**ransverse **m**agnetic

TPA **T**wo-**p**hoton **a**bsorption

VOA **V**ariable **o**ptical **a**ttenuator

WDM **W**avelength **d**ivision **m**ultiplexing

XPM **C**r**oss**-**p**hase **m**odulation

ZBLAN **Z**rF_4-**B**aF_2-**L**aF_3-**A**lF_3-**N**aF

Appendix B: Numerical code for the split-step Fourier method

In this appendix, we show how to use the model based on Schröder et al. to simulate the DFWM mode-locked fiber laser. The following code is based on [65] and written in Mathematica 9.0:

```
 (* This code solves the NLS equation with the split-step Fourier method
based on Govind P. Agrawal in March 2005 for the NLFO book
*)

ClearAll["Global`*"]

(*---Specify input parameters*)
distance = 150.;(*Enter fiber length (in units of L_c)=*)
kappa = -0.001 ;(*Normalized 2nd-dispersion: kappa=beta2*f^2*L/2): \
+ve for normal,-ve for anomalous*)
sigma = 0.; (*Normalized 3rd-dispersion: sigma=beta3*f^3*L/6 *)
G = 1.0;(*small signal gain of Ramam Amp: G=g*L *)
Is = 1.; (*gain saturation parameter*)
alpha = 0.4; (*Normalized fiber amplitude absorption coeff: alpha=l*L*)


n = 2.^0.5;(*Nonlinear parameter n=') \
sqrt(L_D/L_NL)=sqrt(gamma*P0*T0^2/|beta2|) or QT: n=kappa^0.5*)

(*---Specify filter parameters*)
bdwidth = 2. Pi*6.;
delta = 2. Pi*0.5;
a = Log[Sqrt[0.95]];
perta = 0.3;
pertfsr = 0.17;
T = 0.2;
t = Sqrt[T];
r = I*Sqrt[1 - T];

(*---Specify input parameters*)
mshape = -1.;(*m=0 for sech,m>0 for super-Gaussian=*)
chirp0 = 0. ;(*% input pulse chirp (default value)*)

(*
P = 1/(gamma*L); (P is the ref peak power);
uu = A/sqrt(P);
z = z0/L_c; (z0 is the real length, L_c is the cavity length);
tau = f*t; (t is the time of reference traveling frame);
*)

(*---set simulation parameters*)
nt = 2^13; (*% FFT points  (powers of 2)*)
Tmax = 100.; (*(half) window size*)
```

```
stepno = 1*Round[20*distance*n^2];(*No.of z steps to*)
dz = distance/stepno;(*step size in z*)
dtau = (2.*Tmax)/nt ;(*step size in tau*)

Twin = 5.;
fmax = (1./(2. Tmax))*nt/2.;
fwin = 5.;

filterz = 0.5;
plotz = 5;

(*---tau and omega arrays*)
tau = N[Range[-nt/2, nt/2 - 1]]*dtau ;(*temporal grid*)
omega = (1. \[Pi]/Tmax)*
   N[Join[Range[0, nt/2 - 1],
     Range[-nt/2, -1]]];(*[(0:nt/2-1) (-nt/2:-1)]*)
(*frequency grid*)
delaytau = dtau*Range[-Round[Twin/dtau], Round[Twin/dtau]];



(*Input Field profile*)
If[mshape == 0,
  (*;% soliton*)
  uu = Sech[tau]*Exp[-0.5 I*chirp0*tau^2.],
  If[ mshape > 0 ,
   (* super-Gaussian*)
   uu = Exp[-0.5*(1. + 1. I*chirp0)*tau^(2.*mshape)],
   (*White noise*)
   uu = (RandomReal[NormalDistribution[0, 1], nt] +
      I*RandomReal[NormalDistribution[0, 1], nt])*Sqrt[1./2.]
   ]
  ];

temp = RotateRight[
   InverseFourier[uu, FourierParameters -> {1, -1}]*(nt*dtau)/
     Sqrt[2.*Pi], nt/2.];
tempomega = RotateRight[omega, nt/2];


(*---store dispersive phase shifts to speedup code*)
dispersion =
  Exp[(-alpha + I*kappa*omega^2. + I*sigma*omega^3.)*
    dz];(*% nonlinear phase factor*)
(*comb filter type*)
(*original comb filter + BPF*)
(*filtert= \
Exp[-omega^2./bdwidth^2.]*(t^2)/(1-r^2*Exp[-I*(omega+delta)+a]);*)
(*perturbated comb filter + BPF*)
filtert = Exp[-omega^2./bdwidth^2. - perta*Sin[0.5
        *omega/pertfsr]^2]*(t^2)/(1 -
     r^2*Exp[-I*(omega + delta) + a]);

p6 = ListLinePlot[
   Transpose[{tempomega/(2. Pi),
     RotateRight[10.*Log10[Abs[filtert]^2], nt/2]}],
   PlotRange -> {{-fwin, fwin}, {-30, 10}}, Frame -> True,
   ImageSize -> Automatic];
```

```
(*%*********[Beginning of MAIN Loop]***********
% scheme:1/2N\[Rule]D\[Rule]1/2N;first half step nonlinear*)
temp = uu*
   Exp[(I*Abs[uu]^2. + G/(1.0 + Abs[uu]^2./Is))*dz/2.];(*% note hhz/2*)

starttime = SessionTime[];
timeused = SessionTime[] - starttime;
z = 0;

Monitor[ (* Realtime monitoring the simulation progress*)
 For[ i = 1, i <= stepno, i++,
  If[Round[(Mod[z, 1] - filterz )/dz] == 0 ,
    ftemp =
     InverseFourier[temp, FourierParameters -> {1, -1}]*filtert*
      dispersion;
    ftemp =
     InverseFourier[temp, FourierParameters -> {1, -1}]*dispersion;
    ]
  uu = Fourier[ftemp, FourierParameters -> {1, -1}];
 temp = uu*Exp[(I*Abs[uu]^2. + G/(1.0 + Abs[uu]^2./Is))*dz];
 z = z + dz;
 If[Round[Mod[z, plotz ]/dz] == 0 ||
   Round[(Mod[z, plotz ] - plotz )/dz] == 0 ,
  timeused = SessionTime[] - starttime;
  p1 = ListLinePlot[Transpose[{tau, Abs[temp]^2.}],
    PlotRange -> {{-Twin, Twin}, All}, Frame -> True,
    FrameLabel -> {{Null, Null}, {Null,
       StringJoin[{"i = ", ToString[i], ", z = ", ToString[z]}]}}
    ];
  ftemp0 = RotateRight[ftemp (nt*dtau)/Sqrt[2*Pi], nt/2];
  p2 = ListLinePlot[
    Transpose[{tempomega/(2. Pi), 10.*Log10[Abs[ftemp0]^2.]}],
    PlotRange -> {{-fwin, fwin}, All}, Frame -> True,
    FrameLabel -> {{Null, Null}, {Null,
       StringJoin[{" Time = ", ToString[timeused]}]}}
    ];
  p3 = ListLinePlot[Transpose[{tau, Abs[temp]^2}],
    PlotRange -> {{-Tmax, Tmax}, All}, Frame -> True,
    FrameLabel -> {{Null, Null}, {Null,
       StringJoin[{"i = ", ToString[i], ", z = ", ToString[z]}]}}
    ];
  p4 = ListLinePlot[
    Transpose[{tempomega/(2. Pi), 10.*Log10[Abs[ftemp0]^2.]}],
    PlotRange -> {{-fmax, fmax}, All}, Frame -> True,
    FrameLabel -> {{Null, Null}, {Null,
       StringJoin[{" Time = ", ToString[timeused]}]}}
    ];
  autocorr0 =
   RotateRight[
    InverseFourier[
     Fourier[Abs[temp]^2]*Conjugate[Fourier[Abs[temp]^2]]], nt/2];
  p5 = ListLinePlot[Transpose[{tau, autocorr0/Max[autocorr0]}],
    PlotRange -> {{-Twin, Twin}, All}, Frame -> True];
  p = GraphicsGrid[{{p1, p2}, {p3, p4}, {p5, p6}}, ImageSize -> Full]
  ];
 ],
p
]
```

```
uu = temp*
   Exp[(I*Abs[uu]^2. + G/(1.0 + Abs[uu]^2./Is))*
     dz/2.];(*% Final field*)
temp = RotateRight[
   InverseFourier[uu, FourierParameters -> {1, -1}]*(nt*dtau)/
     Sqrt[2*Pi], nt/2];

(*%Final spectrum*)
(*%****************[End of MAIN Loop]***************)
p1 = ListLinePlot[Transpose[{tau, Abs[uu]^2}],
   PlotRange -> {{-Twin, Twin}, All}, Frame -> True,
   FrameLabel -> {{Null, Null}, {Null,
      StringJoin[{"i = ", ToString[i], ", z = ", ToString[z]}]}}
   ];
p2 = ListLinePlot[
   Transpose[{tempomega/(2. Pi), 10.*Log10[Abs[temp]^2.]}],
   PlotRange -> {{-fwin, fwin}, All}, Frame -> True,
   FrameLabel -> {{Null, Null}, {Null,
      StringJoin[{" Time = ", ToString[timeused]}]}}
   ];
p3 = ListLinePlot[Transpose[{tau, Abs[uu]^2}],
   PlotRange -> {{-Tmax, Tmax}, All}, Frame -> True,
   FrameLabel -> {{Null, Null}, {Null,
      StringJoin[{"i = ", ToString[i], ", z = ", ToString[z]}]}}
   ];
p4 = ListLinePlot[
   Transpose[{tempomega/(2. Pi), 10.*Log10[Abs[temp]^2.]}],
   PlotRange -> {{-fmax, fmax}, All}, Frame -> True,
   FrameLabel -> {{Null, Null}, {Null,
      StringJoin[{" Time = ", ToString[timeused]}]}}
   ];
autocorr0 =
  RotateRight[
   InverseFourier[Fourier[Abs[uu]^2]*Conjugate[Fourier[Abs[uu]^2]]],
   nt/2];
p5 = ListLinePlot[Transpose[{tau, autocorr0/Max[autocorr0]}],
   PlotRange -> {{-Twin, Twin}, All}, Frame -> True];
p = GraphicsGrid[{{p1, p2}, {p3, p4}, {p5, p6}}, ImageSize -> Full]

(*Exporting results*)
fname = "2nd_01(0.18)"; (*file name*)
Export[StringJoin[{fname , "_time.dat"}],
  Transpose[{tau, Re[uu], Im[uu], Abs[uu]^2}]];
Export[StringJoin[{fname , "_freq.dat"}],
  Transpose[{tempomega/(2. Pi), Re[temp], Im[temp], Abs[temp]^2,
    RotateRight[Abs[filtert]^2, nt/2]}]];
Export[StringJoin[{fname , "_autocorr.dat"}],
  Transpose[{tau, autocorr0, autocorr0/Max[autocorr0]}]];
```

Appendix C: Fabrication Processes of graphene on silicon waveguides and SOS waveguides

C.1 Graphene on silicon waveguides

C.1.1 Silicon suspended membrane waveguides (SMWs)

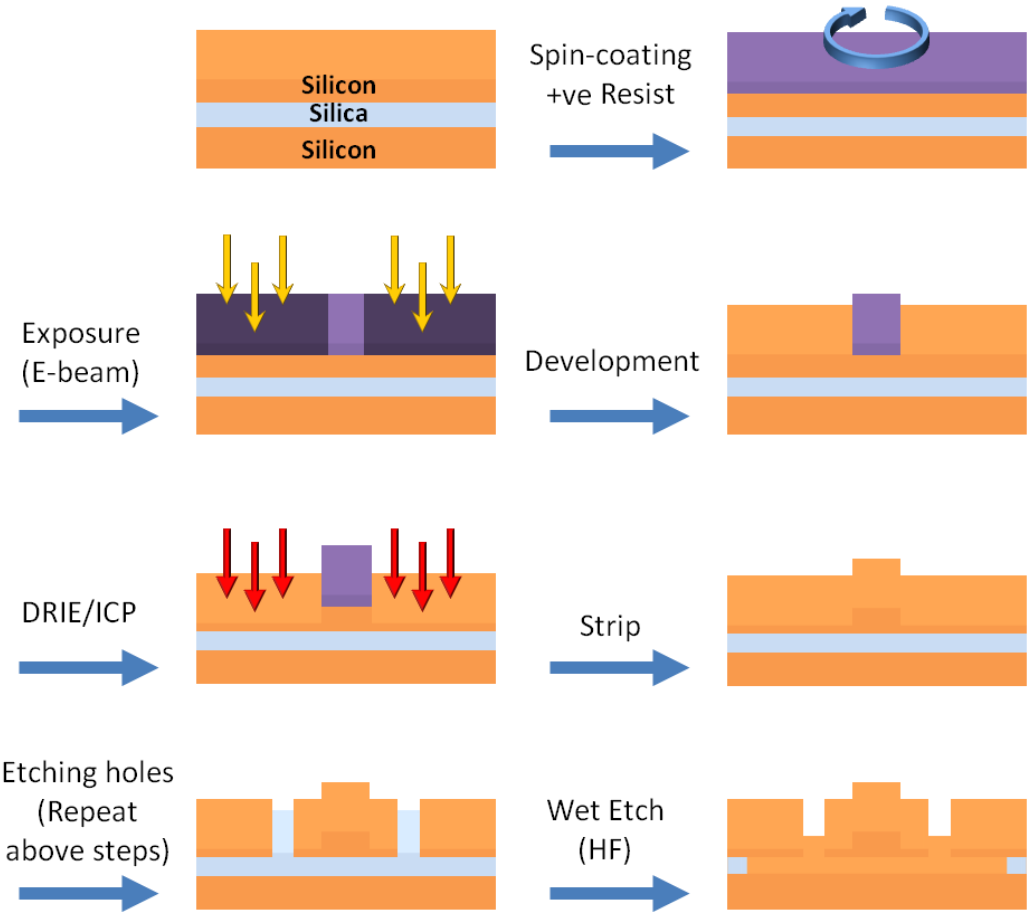

C.1.2 Graphene transfer processes

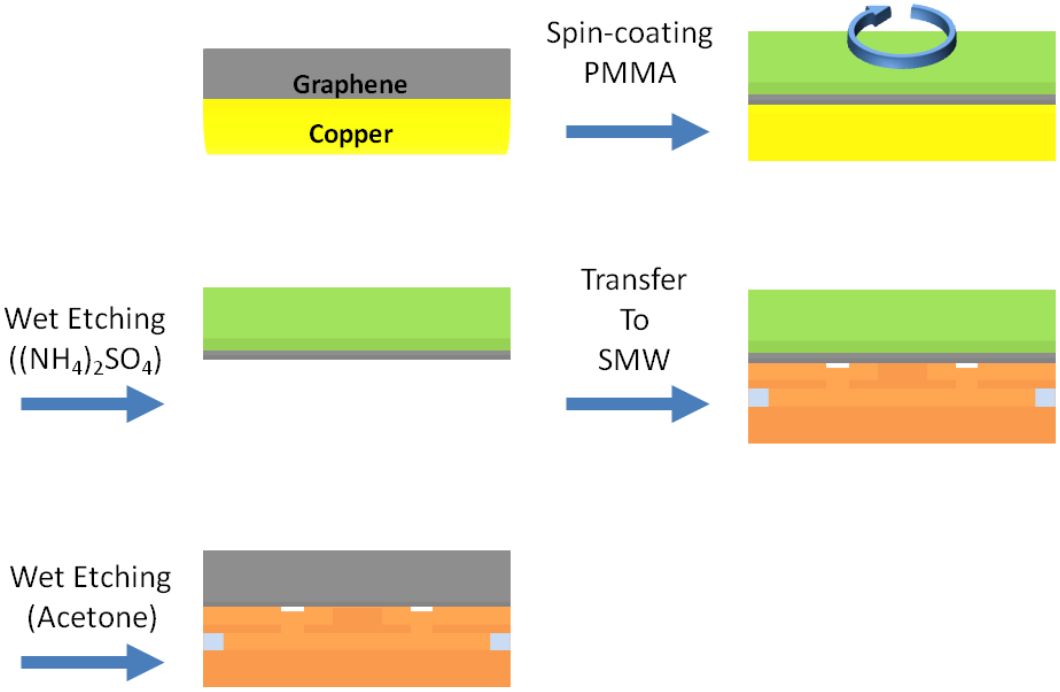

C.2 SOS waveguides

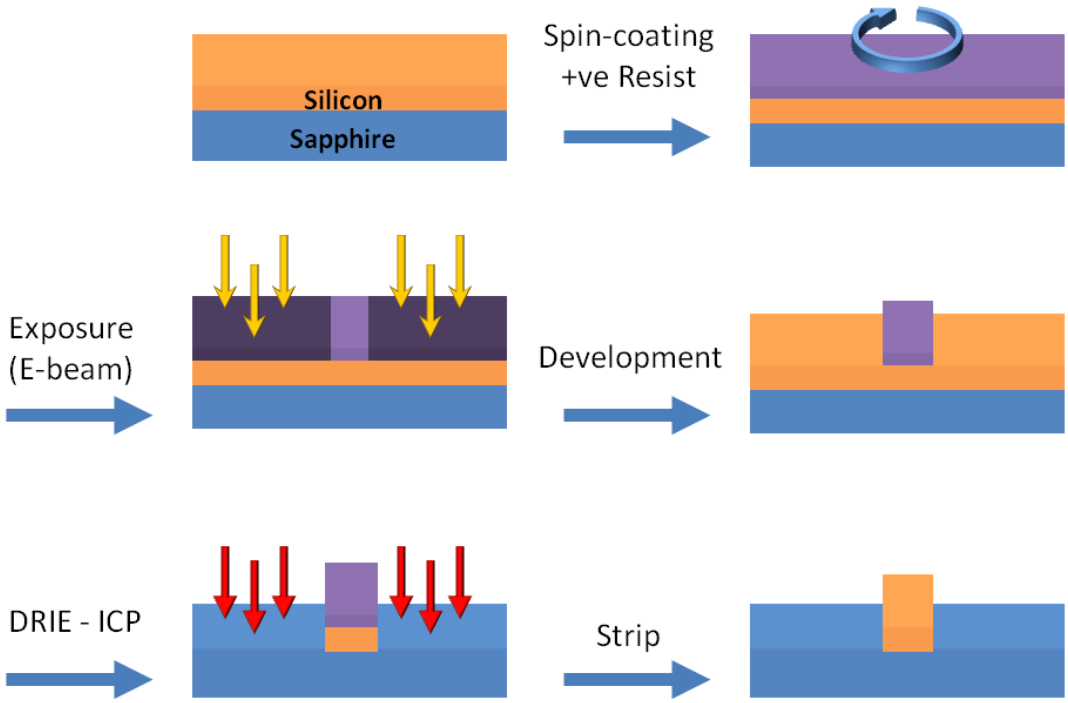

Appendix D: Derivation of thermal shift of MRR resonant wavelength

In this appendix, we show how the Eq. (5.2) for the resonant wavelength of a MRR changes with temperature have been derived. It can be started from the resonant condition of the MRR:

$$\lambda_m = n_{eff}\,\frac{L}{m}. \tag{D.1}$$

By assuming n_{eff} only depends on temperature T and resonant wavelength λ_m. The total temperature derivative of Eq. (D.1) is:

$$\begin{aligned}\frac{d\lambda_m}{dT} &= \frac{L}{m}\left(\frac{\partial n_{eff}}{\partial \lambda_m}\frac{d\lambda_m}{dT}+\frac{\partial n_{eff}}{\partial T}\right)\\ &= \frac{\dfrac{L}{m}\dfrac{\partial n_{eff}}{\partial T}}{1-\dfrac{L}{m}\dfrac{\partial n_{eff}}{\partial \lambda_m}}\\ &= \frac{\dfrac{\partial n_{eff}}{\partial T}}{\dfrac{m}{L}-\dfrac{\partial n_{eff}}{\partial \lambda_m}}\end{aligned}. \tag{D.2}$$

Combining with Eq. (D.1) ($m/L = n_{eff}/\lambda_m$), Eq. (D.2) becomes:

$$\frac{d\lambda_m}{dT} = \frac{\dfrac{\partial n_{eff}}{\partial T}}{\dfrac{n_{eff}}{\lambda_m} - \dfrac{\partial n_{eff}}{\partial \lambda_m}} . \qquad \text{(D.3)}$$

Using $\partial n_{eff}/\partial \lambda_m = (n_{eff} - n_g)/ \lambda_m$, the denominator becomes:

$$\begin{aligned} \frac{n_{eff}}{\lambda_m} - \frac{\partial n_{eff}}{\partial \lambda_m} &= \frac{n_{eff}}{\lambda_m} - \frac{n_{eff} - n_g}{\lambda_m} \\ &= \frac{n_g}{n_{eff}} \end{aligned} . \qquad \text{(D.4)}$$

Combining Eqs. (D.3) and (D.4), λ_m/dT can be written as

$$\frac{d\lambda_m}{dT} = \frac{\lambda_m}{n_g} \frac{\partial n_{eff}}{\partial T} . \qquad \text{(D.5)}$$

Appendix E: List of Publications

Journal Publications

1. **C. Y. Wong**, F. W. Tong, Z. Cheng, K. Xu, Y. M. Chen, and H. K. Tsang, "Stabilization of a multiwavelength erbium-doped fiber laser using a nonlinear silicon waveguide," Applied Physics B, in press (2013);

2. **C. Y. Wong**, Z. Cheng, X. Chen, K. Xu, C. K Y. Fung, Y. M. Chen, and H. K. Tsang, "Characterization of Mid-Infrared Silicon-on-Sapphire Microring Resonators With Thermal Tuning," IEEE Photonics Journal, Vol. 4 (4): 1095-1102 (2012);

3. K. Xu, L. Wang, G. K. P. Lei, Z. Cheng, Y. M. Chen, **C. Y. Wong**, C. Shu, and H. K. Tsang, "Demodulation of 20-Gbaud/s DQPSK Signals Using Wavelength-Tunable Silicon Microring Resonators," Optics Letters, Vol. 37 (16): 3462-3464 (2012);

4. K. Xu, Y. M. Chen, C. Li, X. Chen, Z. Cheng, **C. Y. Wong**, and H. K. Tsang, "An Ultra-Compact OSNR Monitor based on Integrated Silicon Microdisk Resonator," IEEE Photonics Journal, Vol. 4 (5): 1365-1371 (2012);

5. K. Xu, Z. Cheng, **C. Y. Wong**, and H. K. Tsang, "Tunable integrated variable bit-rate DPSK silicon receiver," Optics Letters, Vol. 37 (22): 4738-4740 (2012);

6. Z. Cheng, X. Chen, **C. Y. Wong**, K. Xu, C. K. Y. Fung, Y. M. Chen, and H. K. Tsang, "Focusing Subwavelength Grating Coupler for Mid-Infrared Suspended Membrane Waveguide," Optics Letters, Vol. 37 (7): 1217-1219 (2012);

7. Z. Cheng, X. Chen, **C. Y. Wong**, K. Xu, C. K. Y. Fung, Y. M. Chen, and H. K. Tsang, "Mid-infrared Grating Couplers for Silicon-on-Sapphire Waveguides," IEEE Photonics Journal, Vol. 4 (1): 104-113 (2012);

8. Z. Cheng, X. Chen, **C. Y. Wong**, K. Xu, and H. K. Tsang, "Mid-infrared Suspended Membrane Waveguide and Ring Resonator on Silicon-on-Insulator ," IEEE Photonics Journal, Vol. 4 (5): 1510-1519 (2012);

9. Z. Cheng, X. Chen, **C. Y. Wong**, K. Xu, and H. K. Tsang, "Apodized focusing subwavelength grating couplers for suspended membrane waveguides," Applied Physics Letters, Vol. 101 (10): 101104-101104-4 (2012);
10. Z. Cheng, X. Chen, **C. Y. Wong**, K. Xu, and H. K. Tsang, "Broadband focusing grating couplers for suspended-membrane waveguides," Optics Letters, Vol. 37 (24): 5181-5183 (2012);

11. L. G. Yang, C. H. Yeh, **C. Y. Wong**, C. W. Chow, F. G. Tseng, and H. K. Tsang, "Stable and wavelength-tunable silicon-micro-ring-resonator based erbium-doped fiber laser," Optics Express, Vol. 21 (3), 2869-2874 (2013);
12. K. Xu, Z. Cheng, **C. Y. Wong**, and H. K. Tsang, "UWB Monocycle Pulse Generation based on a Colorless Silicon Photonic Integrated Circuit," Electonics Letters, in press;

Conference Proceedings

1. **C. Y. Wong**, F. W. Tong, Z. Cheng, K. Xu, and H. K. Tsang, "100 GHz Passive Mode-locked Laser based on Nonlinear Silicon Microring Resonator," IEEE Photonics Conference (IPC), accepted, 2013;

2. **C. Y. Wong**, Z. Cheng, Z. Shi, Y. M. Chen, K. Xu, and H. K. Tsang, "Mode-locked Fiber Laser Using Graphene on Silicon Waveguide," IEEE Group IV Photonics Conference, GFP 2013, accepted, 2013;

3. **C. Y. Wong**, F. W. Tong, Z. Cheng, Y. M. Chen and H. K. Tsang, "Four-wave mixing stabilized multiwavelength silicon/erbium-doped fiber hybrid ring laser," IEEE OptoElectronics and Communications Conference, OECC 2012, Paper 3C2-2, Korea, Busan, 2012;

4. **C. Y. Wong**, Z. Cheng, X. Chen, K. Xu, C. K. Y. Fung, Y. M. Chen, and H. K. Tsang, "Mid-infrared micro-ring resonator on silicon-on-sapphire characterized by thermal tuning," IEEE Photonics Conference (IPC), Paper ThZ_5, VA, Arlington, 2011;

5. K. Xu, **C. Y. Wong**, Z. Cheng, and H. K. Tsang, "Performance of Silicon Coupled Resonator Waveguides for Integrated Nyquist Filter," The 10th Conference on Laser and Electro-Optics (CLEO) Pacific Rim, Kyoto, 2013;

6. K. Xu, Z. Cheng, **C. Y. Wong**, and H. K. Tsang, "UWB Monocycle Pulse Generation using a Colorless Silicon Photonic Chip," Submitted to European Conference and Exposition on Optical Communications (ECOC), 2013;

7. Y. M. Chen, G. K. P. Lei, K. Xu, **C. Y. Wong**, X. Chen, Z. Cheng, C. Shu, and H. K. Tsang, "Comparison of extinction ratio enhancement of 10 and 40 Gb/s RZ-OOK signals using pump-modulated four-wave mixing in a silicon waveguide," IEEE OptoElectronics and Communications Conference, OECC 2012, Paper 5B1_4, Korea, Busan, 2012;

8. Z. Cheng, X. Chen, **C. Y. Wong**, K. Xu, C. K. Y. Fung, and Y. M. Chen, and H. K. Tsang, "Mid-infrared suspended membrane waveguides on silicon-on-insulator," IEEE OptoElectronics and Communications Conference, OECC 2012, Paper 4E2-2, Korea, Busan, 2012;

9. Z. Cheng, X. Chen, **C. Y. Wong**, K. Xu, Y. M. Chen, and H. K. Tsang, "Monolithic suspended membrane ring resonator for mid-infrared applications," IEEE Group IV Photonics Conference, GFP 2012, Paper WP5, CA, San Diego, 2012;

10. Z. Cheng, **C. Y. Wong**, K. Xu, and H. K. Tsang, "Apodized Focusing Subwavelength Gratings for Simultaneous Coupling of TE and TM modes," IEEE 2th Optical Interconnects Conference (OIC), Santa Fe, USA, 2013;

11. Z. Shi, **C. Y. Wong**, Z. Cheng, K. Xu, and H. K. Tsang, "In-plane saturable absorption of graphene on silicon waveguides," The 10th Conference on Laser and Electro-Optics (CLEO) Pacific Rim, Kyoto, 2013;